Modeling of the exhaust plume of a submerged exhaust system

A numerical analysis of a submarine exhaust

Maarten Derk Klapwijk

TUDelft
Delft
University of
Technology

ii

Depicted on the front page is a Walrus class submarine [53].

Typeset in LaTeX

Thesis for the degree of MSc in Marine Technology in the specialization of Ship Hydrodynamics

Modeling of the exhaust plume of a submerged exhaust system

A numerical analysis of a submarine exhaust

by

Maarten Derk Klapwijk

Faculty of Mechanical, Maritime and Materials Engineering, 3mE
Delft University of Technology
The Netherlands

Examination committee:
Prof. dr. ir. T.J.C. van Terwisga
Ir. G.M. Rotte
Dr. ir. M.J.B.M. Pourquie
Ir. B. Nienhuis
Ir. M.S. Kerkvliet
Dr. ir. M.I. Gerritsma

July 7, 2017

Abstract

The Royal Netherlands Navy (RNN) operates four diesel-electric submarines, the Walrus class. The submarines sail submerged on electric engines and periodically recharge the batteries with diesel engines at periscope depth. While recharging air is taken in with a snorkel mast, and exhaust gases are dispelled at the back of the sail below water level. During the sea trials of the current class of submarines in the nineties, a disturbance on the surface behind the sail was observed. The rising exhaust gases elevated the surface locally with a height of 1 to 2 m. Due to this elevation visibility backwards through the periscope was limited, water flooded the air intake and the submarines could be easily detected. The elevation was deemed unacceptable and model tests were performed to modify the design and remedy this problem. The Walrus class is scheduled for replacement around 2025, and a similar configuration could be used then. To enable evaluating several exhaust configurations a numerical model is studied to predict the surface elevation.

For a submerged exhaust two flow regimes are of importance, the stratified flow around the submarine and the bubbly flow from the exhaust gases. Rising bubbles are subjected to a number of forces, the forces modeled are drag, added mass, gravitational and buoyancy forces. Basset, collision, lift forces and surface tension are neglected.

To model this situation a numerical method is used. The method applied in this work is the Volume of Fluid code ReFRESCO, which is a Reynolds Averaged Navier-Stokes (RANS) solver. Three test cases are studied, a rising bubble, a turbulent jet and an exhaust plume from a submarine sail. For a rising bubble it is concluded that the results from the code are in agreement with literature, however the lack of surface tension does lead to a diffusion of the air in the domain which is larger than in reality.

The simulations for the turbulent jet show that the momentum in the jet is dominated by buoyancy rather than by the initial inflow momentum. The influence of different turbulence models on the width of the jet and the corresponding surface elevation are investigated. The choice of turbulence model influences the distribution of air in the domain, but does little to the surface elevation. It is concluded that the $k - \sqrt{k}L$ model yields the most physical results where the air spreads out in the domain. This model also has a satisfactory convergence behavior. It is concluded that both the density of the exhaust gas and the velocity profile at the nozzle have

little influence on the final result. A parabolic velocity profile instead of a uniform outflow does improve the convergence. The dominant numerical error is the discretization error, which is in the order of 12% for the surface elevation. To this end the L_∞ norm of the iterative error must be reduced to a satisfactory value, in the order of 10^{-3} or smaller. Comparing the results with experiments is difficult due to a lack of proper experimental data, however it is concluded that the results are in a similar order of magnitude.

Finally the exhaust gases on a submarine sail are modeled. The original configuration of the Walrus class is simulated and compared with available experimental data. For the modeling three simplifications are made: only the flow surrounding the sail is modeled (the hull of the submarine is not modeled), the control planes on the sail are not modeled, and no incoming waves on the free surface are taken into account. Both in the experiments and in the simulations a pulsating behavior can be observed in the rising air. The peaks in the surface elevation are caused by these rising pockets of air. L_∞ norms for the submarine modeling are generally in the order 10^{-3}, but occasionally less. The numerical results are validated against the experimental results. It is concluded that the use of the RANS code ReFRESCO is possible for the modeling of a submerged exhaust of a submarine. The estimated uncertainty for the result is in the order of 15%.

Preface

This report is the result of a research project of nine months at the Delft University of Technology on behalf of the Royal Netherlands Navy.

It is an odd thing to do research into submarines. Most people are unaware that the Royal Netherlands Navy has submarines and even less consider their propulsion mechanism. This research enabled me to look into multiphase CFD from a theoretical perspective, while at the same time keeping a concrete application in mind. It was an interesting learning experience where each new step lead me to reconsider a 16th-century quote which, even though almost five hundred years old, is still very relevant:

"Que sais-je?"

(Michel de Montaigne)

I would like to thank Professor Tom van Terwisga for feedback and discussions on a range of subjects concerning my work. I appreciated the freedom and trust I received throughout the project. Secondly I am indebted to my daily supervisor, Gem Rotte, who greatly enhanced the quality of my thesis with feedback from the start and who introduced me into the basics of CFD. Next to that I am thankful to Maarten Kerkvliet, for all the answers surrounding ReFRESCO, the feedback during the project, but also for assisting with the grid making. Also Bart Nienhuis was a great help with background knowledge on the Navy and submarines in particular. Many thanks for the possibility to work on this assignment. Finally I want to thank Mathieu Pourquie for his knowledge on CFD.

I also need to thank my colleagues at Delft including Erik van Duin, Willian Hogendoorn, and Niek Teeuwen. Finally I want to thank my family, friends and everybody I have not mentioned here.

Delft, July 7, 2017

Maarten D. Klapwijk

Contents

List of Tables

List of Figures

Nomenclature

Symbol	Description	Unit
A	Area	$[\text{m}^2]$
Bo	Bond number	[-]
B	Momentum produced by buoyancy	[kg m/s]
C_p	Pressure coefficient	[-]
D	Diameter	m
E	Validation comparison error	[-]
H	Height	m
L_2	L_2 norm	[-]
L_∞	L_∞ norm	[-]
L_{vK}	Von Kármán length scale	[m]
L	Turbulent length scale	[m]
M	Initial momentum flux	[kg m/s]
M	Molecular mass	[g/mol]
N	Number of members in ensemble	[-]
Q	Volume flux	$[\text{m}^3/\text{s}]$
Re	Reynolds number	[-]
R	Gas constant	J/(mol K)
R	Bubble radius	m
R	Jet radius	m
S_{ij}	Rate of strain tensor	[-]
St	Strouhal number	[-]
S	Source or sink term	[-]
S	Salinity	g/kg
T	Sample record length	s
T	Time	s
T	Temperature	K
$U_\%$	Statistical uncertainty	[%]
U_∞	Free stream velocity	m/s
U_ϕ	Uncertainty of results	[-]
U_{exp}	Experimental uncertainty	[-]
U_{inp}	Input uncertainty	[-]
U_{val}	Validation uncertainty	[-]

Symbol	Description	Unit
U	Relative velocity of bubble with respect to the liquid	m/s
V_S	Ship speed	kt
V_{gas}	Outflow velocity of the gas	m/s
V	Volume	m^3
We	Weber number	[-]
Γ	Diffusive coefficient	[-]
α	Volume fraction	[-]
δ_{ij}	Kronecker delta	[-]
ϵ	Turbulent dissipation	[-]
γ	Surface tension coefficient	N/m
κ	Von Kármán constant	[-]
λ	Scaling factor	[-]
$\mathbf{F}_f$	Flux	[-]
$\mathbf{F}$	Force	N
$\mathbf{S}$	Surface	m^2
$\mathbf{V}$	Velocity vector	m/s
$\mathbf{f}$	Force per unit volume	N/m^3
$\mathbf{n}$	Normal vector	[-]
$\mathbf{u}$	Velocity vector	m/s
$\mathcal{V}$	Volume	m^3
μ	Dynamic viscosity	Ns/m^2
∇	Gradient operator	[-]
ν_t	Turbulent or eddy viscosity	m^2/s
ν	Kinematic viscosity	m^2/s
ω	Specific dissipation rate	[-]
ω	Vorticity	Hz
ϕ_V	Volume flow gas	m^3/s
ϕ	Flow property	[-]
ρ	Density	kg/m^3
σ	Standard deviation	[-]
τ	Stress vector	Pa
d	Diameter nozzle	m
$f(\rho)$	Reboud correction factor	[-]
f_L	Lowest dominant frequency component	Hz
g	Gravitational acceleration	m/s^2
h_i/h	Grid refinement factor	[-]
h	Height nozzle	[m]
$k_\%$	Coverage factor based on normal distribution	[-]
k	Turbulent kinetic energy	[m^2/s^2]

Symbol	Description	Unit
l_m	Morton length scale	[m]
m	Mass	[kg]
n	Number of phases	[-]
n	Eddy viscosity correction factor	[-]
p	Pressure	Pa
q	Source or sink term	[-]
r	Cross-jet radial distance from center line	m
t	Time	s
t	Temperature	°C
u, v, w	Velocity components	m/s
u_x, u_y, u_z	Velocity components	m/s
x, y, z	Cartesian coordinates	m
y^+	Dimensionless wall distance	[-]

Acronyms

AIP   Air Independent Propulsion.
ASM   Algebraic Stress Models.
AVF   Air Volume Fraction.

BC   Boundary Condition.

CFD   Computational Fluid Dynamics.
CG   Conjugate Gradient.

DES   Detached Eddy Simulation.
DMO   Defense Materiel Organisation.
DNS   Direct Numerical Simulation.

EARSM   Explicit Algebraic Reynolds Stress Model.

GMRES   Generalized Minimal RESidual method.

iLES   implicit Large Eddy Simulation.

LES   Large Eddy Simulation.

MARIN   Maritime Research Institute Netherlands.

NATO   North Atlantic Treaty Organization.

QUICK   Quadratic Upstream Interpolation for Convective Kinematics.

RANS   Reynolds Averaged Navier-Stokes.
RDM   Rotterdamsche Droogdok Maatschappij.
ReFRESCO   Reliable and Fast Rans Equation Code for Ships and Constructions Offshore.
RGB   Red Green Blue.
RNN   Royal Netherlands Navy.

RSM   Reynolds Stress Models.

SAS   Scale-Adaptive Simulation.
SST   Shear Stress Transport.

TNT   Turbulent/Non Turbulent.

URANS   Unsteady Reynolds Averaged Navier-Stokes.

Chapter 1

Introduction

The Royal Netherlands Navy (RNN) has operated submarines since 1906. Since the nineties four diesel-electric submarines of the Walrus class are in service.

Where previous classes of submarines made use of a surface exhaust system, on submarines of this type the exhaust system was replaced with a submerged exhaust to reduce the infrared signature. During the sea trials of the first submarine of the Walrus class a number of problems arose. The new exhaust system caused a local elevation of the water surface behind the submarine. This elevation consisted out of a mixture of water and gas and rose to a height of one to two meters. The elevation of the surface restricted the field of view backwards with the periscope. Next to that, due to the rising water the valves in the air inlet were triggered to close and consequently the diesel engines shut down. Finally the disturbance on the water surface was clearly visible from other vessels, causing signature issues. The problem was not acceptable for a submarine, and the yard, the Rotterdamsche Droogdok Maatschappij (RDM), asked Maritime Research Institute Netherlands (MARIN) to investigate the exhaust configuration. Using model tests a number of changes were made to the shape of the submerged exhaust which resulted in the distinctive toucan shape on the back of the sail.

At the moment of writing, the first plans are being drawn by the Defense Materiel Organisation (DMO) for a new class of submarines. DMO is the organization which is responsible for the fleet of the RNN. The new class of submarines is scheduled to replace the Walrus class after 2025. DMO has expressed desire in a method to numerically predict the size of the exhaust plume of a submarine to be able to use this tool in the design of a new class of submarines.

The numerical code used in the research is the code ReFRESCO which is developed by MARIN [45]. DMO has a preference for the use of ReFRESCO due to previous experiences and a longstanding collaboration with MARIN for the design of naval vessels, including submarines.

This report describes a literature study and master thesis into this subject. The problem is formulated in more detail in chapter 2. In this chapter also an overview of the specifications of the Walrus class submarines is given. Chapter 3 describes

different exhaust systems used for naval purposes. The physics of multiphase flows are described in chapter 4, whereas chapter 5 goes into detail on the numerical modeling and the background of Computational Fluid Dynamics (CFD).

The following chapters describe the obtained numerical results. First the first test case, a rising bubble, is described in chapter 6, secondly a turbulent jet, is described in chapter 7 and finally the modeling of a submarine exhaust is shown in chapter 8.

Chapter 9 summarizes the main conclusions and gives a number of recommendations for further research. Also recommendations for the design of a submerged exhaust system are given.

Due to confidentiality reasons in some figures no axes are shown, and no exact values for a number of parameters are given.

Chapter 2

Problem description

This research focuses on the numerical modeling of exhaust gases from a diesel-electric submarines. This chapter describes the background of the problem.

2.1 Submarines configurations

The operational profile of naval submarines dictates that they are able to operate submerged and undetected for a considerable amount of time. This leads to two demands for the propulsion: the propulsion should use a limited amount of air, since it is not possible to obtain large quantities of air at depth, and the propulsion should be as silent as possible to avoid detection. These demands have led to three main power generation configurations for modern submarines:

- a nuclear powered submarine, in which a nuclear plant generates steam which either drives a steam turbine to directly power the propeller, or powers electric motors by means of a generator. A more detailed description can be found in section 2.1.1.

- a conventionally powered submarine, in which a diesel engine drives a generator to charge batteries. The electricity of the batteries powers electric motors. A detailed description can be found in section 2.1.2.

- a submarine with Air Independent Propulsion (AIP). This can be either be fuel cells, closed cycle diesel engines or Stirling engines. A detailed description can be found in section 2.1.3.

These three configurations each have their advantages and disadvantages, which are described hereafter.

2.1.1 Nuclear submarines

The main advantage of a nuclear reactor on board of a submarine is the lack of air required to generate power. Therefore a submarine equipped with such a prime mover effectively has no need to surface while at sea.

The main disadvantage of this configuration is the large cost of a nuclear installation, both in acquisition and in operation. Secondly a nuclear installation requires a large space on board the vessel, which leads to a considerable vessel size. This makes operations close to the coast in shallow waters (so called "brown water" operations) difficult or even impossible. Finally the number of ports which the submarine can enter are limited, since not all ports allow nuclear powered vessels. This leads to difficulties in the resupplying of the submarine.

2.1.2   Conventionally powered submarines

The main advantage of a conventionally powered submarine is the decreased size required for the propulsion, which allow for a smaller vessel size. Also the lower costs make vessels with such a propulsion system attractive.

The disadvantage is that periodically the batteries must be recharged, which requires the use of diesel engines. The diesel engines require a large amount of air which must be obtained from above the surface. Early submarines therefore had to surface periodically to charge the batteries, or were designed to sail on the surface and only dive when required (in case of an attack or an evasion). Developments in radar technology required diesel-electric submarines to remain submerged for longer periods of time, however sailing submerged limited both the speed as well as the range. The invention of the snorkel solved these problems. The snorkel, or sniffer, is a device which allows the submarine to take in air while sailing submerged on periscope depth (just underneath the surface, at a depth where the periscope extends above the water). The snorkel is an extendable pipe which pierces the water surfaces while in use, and can be retracted in the hull while not in use. Figure 2.1 shows a submarine on the surface with a raised snorkel and exhaust mast, figure 2.2 shows a submarine sailing at periscope depth with a snorkel mast. It can be easily understood that it is considerably more difficult to spot a submarine using such a device. A modern submarine has to take in air periodically but can remain submerged while doing so. The rate of charging depends on factors such as the available power at a certain speed and allowable charging speed of the batteries. The occurrence of snorkeling can be as high as once per day.

2.1.3   Air independent propulsion

Finally there are the so called non-nuclear air independent propulsion systems. These include fuel cells based on hydrogen, closed cycle diesel engines where pure air is stored and used for the engine, and Stirling engines, where no combustion occurs in the cylinders. These techniques are left out of the current comparison, since they are not relevant to this research.

Figure 2.1: A submarine with a raised snorkel and exhaust mast (the left and right mast respectively) [84].

Figure 2.2: A submarine of the Walrus class sailing while using a snorkel. The visible masts on this image are, from left to right: the snorkel mast, the radar mast, the communications mast, the observation periscope and the attack periscope. On the left the surface elevation due to the submerged exhaust is visible [52].

2.2   Choice of type of submarine

Based on the described advantages and disadvantages a choice for a type of propulsion can be made. The United States Navy and the Royal Navy make use of nuclear powered submarines exclusively, a large number of smaller navies, including the RNN, make use of conventionally or air independent powered submarines. This choice is based on both financial as well as operational reasons.

2.3   Implications of a conventional submarine

The first implication was already named, a snorkel is needed to provide air to the submarine. Next to an air intake also an exhaust is needed to expel the rest products of the combustion in the engine. A schematic overview of such a system can be found in figure 2.3.
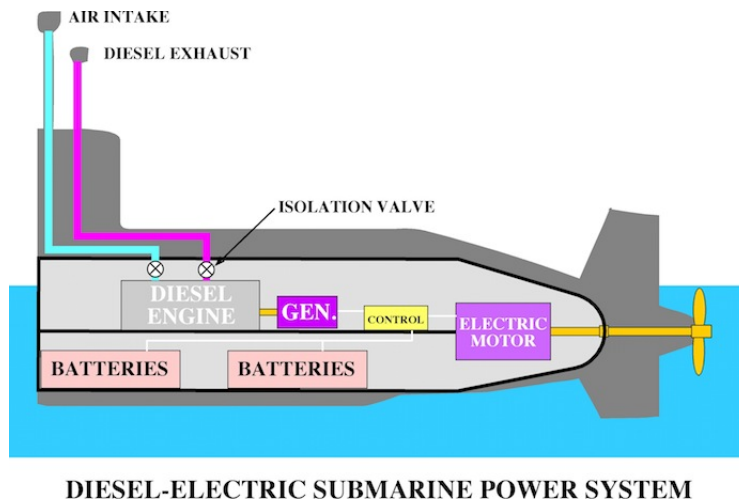
Figure 2.3: The power system of a diesel-electric submarine [84].

The diesel engines can operate when the submarine sails on periscope depth. To be able to stay on periscope depth the submarine controls its depth using control planes. To generate lift a flow over the control planes is needed, therefore the submarine sails at a minimum speed or higher while at periscope depth.

For a submarine sailing at periscope depth there are two ways to expel the exhaust gases. One option is an extendable chimney. This devise is similar to a snorkel, but here exhaust gas is expelled through it. The downside of this system is that the signature of the hot exhaust gases is easily detectable using an infrared camera. This is a dry exhaust, more details can be found in section 3.1.

The second solution is the solution currently in use on the Walrus class submarines, a submerged exhaust system. Here the exhaust gases are expelled in the water. More details can be found in section 3.3. As stated this leads to an elevation

of the water surface, this surface elevation is visible in figure 2.2 on the left of the image. The process is similar to surface elevation in a swimming pool with a bubble section. At a Walrus class submarine the exhaust is located several meters below the surface [79]. This system is the focus point of this research. The presence of a submerged exhaust leads to a back-pressure in the exhaust system, which leads to a number of demands in the propulsion system. These demands for the propulsion system are outside of the scope of the research.

In this research the focus lies on naval submarines, however the work can also be applied to other ships where a conventional chimney is not acceptable. Examples are yachts and cruise ships.

2.4   Submarine hull

The hull of a submarine is generally shaped like a cigar, it consists out of a cylinder shaped mid body, a spherical shaped fore body and a cone shaped aft body. On the mid body a tower is placed for operational purposes. This tower is known as a sail, or a bridge fin. Throughout this report the term sail will be used. The sail houses a number of masts, such as [64]

- an observation periscope,

- an attack periscope,

- a radar mast,

- a communications mast,

- the snorkel mast.

The masts can be seen in figure 2.2.

The exhaust on a diesel-electric submarine is located as high as possible to reduce the back pressure in the exhaust. Back pressure can be thought of as resistance for the exhaust gases. A high back pressure in the exhaust degrades the performance of the diesel engines. A higher located exhaust leads to a lower hydrostatic pressure at the exhaust and thus a lower back-pressure. To gain maximum height the exhaust is located on the sail. To reduce the interference with the periscope it can be considered to locate the exhaust further aft, however this leads to either an added appendage to increase the height of the exhaust, or to a lower located exhaust. Both of which are not favorable, due to an increase in resistance of the ship or back pressure in the exhaust respectively.

2.5   Walrus class submarines

The RNN operates four diesel-electric submarines of the Walrus class. These submarines are used for the following purposes [53]:

- intelligence gathering,

- base for operations of special forces,

- target vessel for exercises with frigates and helicopters,

- deploy sea mines,

- locate enemy submarines and surface vessels, and if necessary attack them.

The Walrus class has been in service since the nineties, and is scheduled to be in service until 2025. The class consists of four vessels:

- Zr. Ms. Walrus, S802, in service since 1992,

- Zr. Ms. Zeeleeuw, S803, in service since 1990,

- Zr. Ms. Dolfijn, S808, in service since 1993,

- Zr. Ms. Bruinvis, S810, in service since 1994.

The Walrus class submarines are so-called blue-water diesel-electric submarines, so diesel-electric submarines with a large range and oceangoing capabilities. This type of submarines is rare, and therefore in high demand by North Atlantic Treaty Organization (NATO). A photograph of a submarine of the Walrus class can be found in figure 2.4. An overview of the dimensions and specifications can be found in table 2.1.

Figure 2.4: A submarine of the Walrus class [53].

Table 2.1: Dimensions and specifications of the Walrus class submarines [53].

Length	68	m
Width	8.5	m
Depth	7.5	m
Diving depth	>300	m
Displacement sailing on the surface	2450	ton
Displacement submerged	2800	ton
Maximum speed sailing on the surface	11	kt
Maximum speed submerged	20	kt
Crew	55	[-]

Chapter 3

Exhaust systems

Exhaust systems for marine purposes can be split into three different concepts, namely dry exhausts, wet exhausts and submerged exhausts. In this chapter the three concepts and their properties are described. Also an overview of the research done into these concepts is given.

3.1 Dry exhaust

A dry exhaust is the common exhaust system for commercial vessels. Here a vertical pipe runs through the decks from the engine to a funnel (also known as chimney or stack) above the superstructure where the exhaust gases exit the vessel. The advantages of this configuration is that there is no danger of water entering and damaging the engine. The configuration requires a lot of room on board due a need for insulation material. Attention must be paid that the funnel is located high enough so that the exhaust gases stay clear of the ship [34].

Kulkarni et al. [34] gives an overview of the changes in funnel design during the last hundred years. The main developments are that the height of the funnel has decreased, and the size and number of funnels are reduced. These developments and an increasing competition for space and height on top of the superstructure have led to a number of investigations into smoke nuisance problems on ships. The investigations are often for naval vessels to determine:

- the interaction of the gases with the superstructure, aircraft and helicopters,

- the effect of high temperature exhaust gasses on equipment located on the superstructure,

- the effect of exhaust gases sucked into gas turbine intakes,

- the effect of high temperature gases on the vessels infrared signature.

Due to the naval origin of this research a large number of investigations are not available in open literature.

The studies done into these areas can be divided into the following four categories: wind tunnel modeling, field measurements and observations, analytical methods and computational fluid dynamics.

From a naval point of view the major downside of such an exhaust system is the large infrared signature due to the exhaust plume. This demand has led to the use of a submerged exhaust system on the Walrus class submarines.

3.2   Wet exhaust

An alternative to the dry exhaust system is a wet exhaust system. Here the exhaust gases are mixed with seawater after the engine to reduce the temperature of the exhaust gases. The water and exhaust gases are then disposed on or slightly above the waterline. This system requires less space on board and eliminates the risk of smoke coming down on the vessel.

A downside is the risk of damaging the engine due to water entering through the exhaust, in case of a poorly designed system or a failure. These systems are mostly used on small vessels with a limited amount of exhaust gases, limited deck area and where it is unacceptable to smell exhaust gases on deck.

Research into this subject is limited. It appears that most of these designs are either based on experience, or are not available in open literature. This can be explained due to the fact that these systems are almost exclusively fitted on small (pleasure) craft. Literature which is available often focuses on pollutant gas emissions, which lies outside of the scope of this research, or on the influence on the engine performance.

3.3   Submerged exhaust

The third system is a completely submerged or underwater exhaust. This is used on submarines due to the operational profile since the infrared signature is reduced to a minimum. Such a system can also be applied for purposes as noise reduction, smell reduction or for aesthetic reasons. A division in two configurations can be made.

A method for surface ships makes use of a scoop underneath the hull which generates a low pressure zone at forward speed. This low pressure zone reduces the local total pressure and mixes the exhaust gases with the water [11]. An image showing such a system is shown in figure 3.1. The scoop can be located on the bottom or on the side of the hull.

Delvoye [11] looked into the disturbance on the flow caused by the presence of the exhaust scoop, both in 2D and 3D. Use was made of the code FresCo, the predecessor of ReFRESCO. It is important to note that this research focused on a single phase flow around the exhaust scoop, no exhaust gas is injected.

On a submarine of the Walrus class the working principle of the exhaust system is different. Here the gases are pumped out against the hydrostatic backpressure, and
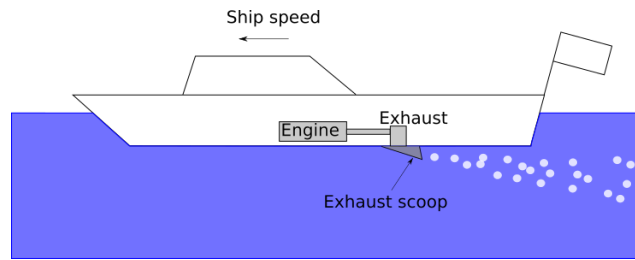
Figure 3.1: Underwater exhaust, by means of a scoop located under the hull. The low pressure zone created by the scoop sucks the gas out of the exhaust and into the water.

are transported to the surface through their own buoyancy. The exhaust is located on the top of the vessel. The main research done in this area is experimental, and is obtained from DMO. More detail on this research can be found in section 8.1. In figure 3.2 the location of the exhaust system on the sail of the Walrus class submarines can be seen.

Figure 3.2: The sail of a Walrus class submarine, the location of the exhaust is indicated with the red box [53].

3.4 Exhaust gas properties

The gases which must be expelled are the exhaust gases of the diesel engines. These gases consist out of combustion components mixed with unused engine charge air. The main combustion components are carbon dioxide, CO_2 and water, H_2O. Engine charge air is ambient air, so this mainly consists out of oxygen, O_2, nitrogen, N_2

and carbon dioxide, CO_2. The volumetric concentrations of these gases in exhaust gas depend on engine properties, fuel properties and engine load. The volumetric concentrations are usually in the range [1]

- CO_2: 2 - 12%,

- H_2O: 2 - 12%,

- O_2: 3 - 17%,

- N_2: 93 - 59%.

In case of increasing engine load the CO_2 and H_2O content increase and the content of O_2 decreases. As an approximation the properties of air can be used for calculations, the error associated with neglecting the combustion components is limited to 2% [1]. The main difference is the increase in molecular mass, which is in the order of 5% depending on the fuel and engine.

Also particles, such as soot, are present in the exhaust gases. Magnaudet and Eames [41] state that particles increase the drag force on a bubble in a liquid. This influence is described for a single rising bubble. To include this in the modeling it is necessary to track each bubble explicitly which is not possible in ReFRESCO. Also the influence is questionably since in this work the bubble flow is a more of a 'global' flow rather than a flow with individual dispersed bubbles. Based on this the influence of these particles on the exhaust plume is assumed to be negligible.

Chapter 4

Multiphase flows

The term multiphase flow describes a fluid flow consisting of more than one phase or component. Two general types of multiphase flows can be observed, namely disperse flows and separated flows. In a disperse flow particles, drops or bubbles are transported by a continuous flow. Examples are gas bubbles in a liquid, rain drops falling through air and particles transported by a flow. A separated flow contains two or more continuous flows of different fluids which are separated by interfaces [4]. Examples of this are a layer of oil on water and a free surface flow.

In the context of this work both these different multiphase flow regimes can be observed. Firstly a stratified two phase flow, namely the free surface, is present. This is a separated flow. Secondly there is a bubbly flow, namely the exhaust gases in the water. This is a dispersed flow. The two flow regimes are shown schematically in figure 4.1.
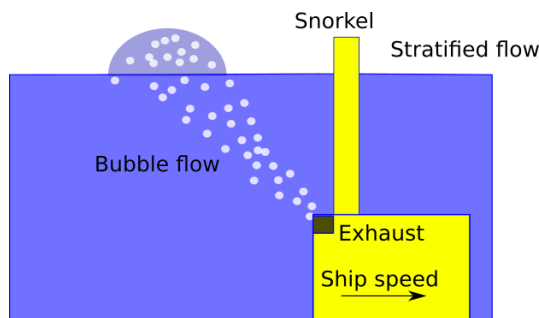
Figure 4.1: The two flow regimes present for a submerged exhaust.

The focus of this work lies on the dispersed gas-liquid flow. In this regime the density difference between the gas and the liquid lies in the order of 10^3. The Reynolds number, the ratio between inertial and viscous forces, is calculated for the bubbles. Based on the rising velocity and the dimensions as given by Van Hees [79], it has a value in the range $1.8 \cdot 10^5 - 3.7 \cdot 10^5$. These large values mean that inertial forces are dominant, and the role of viscosity can be neglected for the rising of the

15

bubbles. Viscosity must be included however to model the disturbed flow behind the sail in which the bubbles rise.

In this chapter a background into the physics of a bubble flow is given. The description will start with the forces acting on a single bubble, then this is extended to different flow regimes for bubble flow.

4.1   Forces acting on a bubble

The dynamics of a bubble transported through a fluid depend on the forces acting on a bubble. These forces deform the gas-liquid interface, the barrier between gas and liquid. This interface moves and deforms both in time and space. A number of different forces can be identified, this distinction is partly based on the work by Rafique et al. [61]:

- Drag force, this force counteracts the motion of a bubble with respect to the fluid and decreases its velocity. It can be divided into skin friction and form drag.

  Skin friction occurs due to the motion of the bubble relative to the fluid. It depends on the viscosity of the fluid. Based on the large value of the Reynolds number as determined in the previous section it can be concluded that this term is negligible.

  Form drag, or pressure drag, depends on the shape of the object. It depends on the area of the bubble perpendicular to its direction of movement, its velocity and the drag coefficient. The drag force is proportional to the velocity squared for a turbulent flow.

- Added or virtual mass force, this force acts due to the acceleration of the surrounding fluid when the bubble is accelerated. It depends on the acceleration and shape of the bubbles, the gas holdup of the fluid, and the volume fraction of the liquid which is accelerated with the bubble. Rafique et al. [61] state that although the influence of the steady state drag force is predominant as compared to the added mass force, the added mass force must be included to accurately predict the hydrodynamics.

- Gravitational force, force due to the gravity acting on the bubble. This force is small for a bubble in water due to its relatively small dimensions and low density, which both result in a low mass.

  The Froude number gives the ratio between inertial and gravitational forces. Based on the values given by Van Hees [79] the Froude number has a value in the range $2.4 - 0.59$. Based on this it can be concluded that gravitational forces can not be neglected.

- Buoyancy force, due to the difference in density between the bubble and the surrounding fluid. If a bubble rises the pressure of the surrounding liquid

decreases so the volume of the bubble increases. As a consequence the density inside the bubble decreases even further, which leads to a higher rising velocity.

- Basset or history force, due to a lagging boundary layer development for an accelerating bubble. It reduces the acceleration with respect to the surrounding liquid. This force is often neglected due to difficulties in implementing it, the influence is only significant for bubbles with a high acceleration.

- Collision force, the force on a bubble due to the presence of other bubbles in the fluid. The force depends on the velocity and mass of a bubble. It is possible that due to collisions bubbles merge.

- Surface tension, a force acting on the surface of the bubble with the tendency to minimize the area of the bubble (also known as the interface). Surface tension and its influence are described in more detail in section 4.3.

- Lift force, due to the bubble moving through a nonuniform flow field a force perpendicular to its relative velocity can arise due to a pressure difference over the sides of the bubble. Drew and Lahey [13] state that this only occurs in slow viscous flow, and that "there is no obvious indication that the lift force is of practical importance in gas-liquid flows".

- other external forces, for example hydro-magnetic forces. These forces are outside the scope of this work.

4.2 Bubble flows

A bubble flow is a gas-liquid two-phase flow in which a large number of bubble is dispersed or suspended in the liquid. Bubble flows are divided into four different flow regimes based on the interactions between bubbles and between bubbles and the liquid [29]:

- ideally separated bubble flow, here the bubbles behave like single bubbles. There is no direct or indirect interaction between bubbles,

- interacting bubble flow, here the bubbles interact with each other directly or indirectly due to collisions or the effects of wakes caused by other bubbles, these interactions are caused by a higher bubble number density,

- churn turbulent bubble flow, when the bubble number density is even higher, the bubbles tend to merge and form so-called cap bubbles. Both cap bubbles and smaller bubbles are present, in this flow type there are many interactions between bubble motions and the turbulent flow,

- clustered bubble flow, here large bubbles cluster and behave as a gas slug, these slugs can merge even further or separate into individual bubbles.

4.3   Surface tension

Surface tension is the tendency of a fluid surface to reduce the surface area to a minimum, it can therefore influence the shape of bubbles. Surface tension occurs whenever there is a discontinuity in density, at a liquid-liquid or liquid-gas interface. The consequence of surface tension is that the interface behaves as if it is an elastic membrane under tension. Surface tension causes a pressure difference over the interface, since the surface tension tends to decrease the volume of the bubble. The pressure difference under the absence of fluid motion and buoyant forces can be shown to be

$$p_i - p_o = \gamma \left(\frac{1}{R_1} + \frac{1}{R_2} \right) \tag{4.1}$$

in which γ is the surface tension coefficient in [F/m] and R_1 and R_2 are the radii of curvature of the surface [35]. This equation is also known as the Young-Laplace equation. It can be seen that the pressure difference is inversely dependent on the dimensions of the bubble.

The value of γ is inversely dependent on the temperature and is given for water as [24],

$$\gamma_w = 235.8 \left(1 - \frac{T}{T_C} \right)^{1.256} \left(1 - 0.625 \left(1 - \frac{T}{T_C} \right) \right) \tag{4.2}$$

with γ in mN/m, the temperature T in Kelvin and $T_C = 647.098$ K, the critical temperature. It is stated that the uncertainty of this prediction lies in the order of $\pm 0.5\%$ for temperatures below 100° C. The value for seawater is given using a correction [56],

$$\gamma_{sw} = \gamma_w \left(1 + 3.766 \cdot 10^{-4} S + 2.347 \cdot 10^{-6} S \cdot t \right) \tag{4.3}$$

in which S is the reference salinity in g/kg, and t is temperature in degrees Celsius.

The influence of surface tension effects related to gravitational effects is determined by the Bond number (also known as the Eötvös number (Eo)) [35]. The Bond number is defined as

$$Bo = \frac{\rho g D^2}{\gamma} \tag{4.4}$$

in which D is the diameter of the bubble and γ is the surface tension. At high Bond numbers surface tension effects can be ignored due to a low relative influence compared to gravity.

Also the influence of surface tension effects related to inertial forces can be expressed, this is determined by the Weber number. The Weber number is defined as

$$We = \frac{\rho U^2 D}{\gamma} \tag{4.5}$$

in which U is the relative velocity of the bubble with respect to the liquid, so the rise velocity of the bubble [41]. At high Weber numbers surface tension effects can be ignored due to a low relative influence compared to inertial forces.

It is known that the presence of small particles on the interface reduces the surface tension. Water molecules have a high intermolecular force due to hydrogen bonds, which leads to a high surface tension. The presence of particles breaks up a number of these bonds and therefore reduces the surface tension.

The report written by Van Hees [79] states that the bubbles have a diameter varying from 0.1 m to 0.4 m. The rising time for these bubbles is 3 s and 1.5 s respectively. The value of the surface tension is estimate to be around 75 mN/m, calculated using equations 4.2 and 4.3 with a seawater temperature of $10°C$ and a salinity of 122.2 g/kg. Based on these dimensions and this value of the surface tension the pressure difference caused by the surface tension was estimated using the Young-Laplace equation. The Young-Laplace equation is valid in the absence of fluid motion and buoyant forces, both of which are not the case in a submerged exhaust system, however it does give an indication of the order of magnitude. The range for the pressure difference obtained is between $3.11 - 0.78$ Pa.

Also the Bond number and Weber number are calculated with these values. The Bond number in this situation has a value in the range $1.3 \cdot 10^3 - 2.1 \cdot 10^4$, and the Weber number has a value around $7.2 \cdot 10^3$.

Based on this, the small pressure difference and the large Bond and Weber number it is concluded that the influence of surface tension compared with gravitational and inertial effects is negligible. Surface tension can therefore be left out of the current modeling. This is in agreement with d'Agostino and Salvetti [10] who state that for large bubbles the surface tensions and dissipation due to viscosity are negligible.

Chapter 5

Computational Fluid Dynamics

A fluid is defined as a medium which deforms continuously when a shear force is applied. Analytical solving of fluid mechanics is difficult and in many cases even impossible. This has lead to the rise of Computational Fluid Dynamics (Computational Fluid Dynamics (CFD)). CFD is the modeling of fluid behavior using numerical methods. It has the advantage that more complex problems can be solved and that the flow can be analyzed in detail, which is often difficult or impossible using experiments. This chapter describes the basis of CFD.

5.1 Conservation equations

The modeling of flows is based on mathematical models based on physical principles. The two main mathematical equations for fluid flows are the conservation of mass, also known as the continuity equation, and the conservation of momentum, also known as Newton's second law. Together these two conservation laws form the Navier-Stokes equations.

5.1.1 Conservation of mass

The derivation shown here is based on the derivation given by Kundu et al. [35].
The conservation of mass can be derived using an arbitrary fixed control volume V. The change of mass in the volume should be equal to the the mass flux across the surface of the control volume, which can be expressed mathematically as

$$\iiint\limits_{V} \frac{\partial \rho}{\partial t} \mathrm{d}V = -\oiint\limits_{S} \rho \mathbf{u} \cdot \mathrm{d}\mathbf{S}. \tag{5.1}$$

Using the divergence theorem this equation can be rewritten to the continuity equation

$$\frac{\partial \rho}{\partial t} + \nabla \cdot \rho \mathbf{u} = 0. \tag{5.2}$$

A detailed derivation can be found in appendix A.

Often the simplification is used that a flow is incompressible. Compressibility effects the flow when the fluid velocities are near the speed of sound. The effect of compressibility can be neglected if the Mach number is smaller than 0.3 [35]. This condition is satisfied in this work.

If an incompressible flow is considered $\frac{\mathrm{D}\rho}{\mathrm{D}t} = 0$, so the conservation of mass simplifies to

$$\nabla \cdot \mathbf{u} = 0. \tag{5.3}$$

5.1.2   Conservation of momentum

The derivation shown here is based on the derivation given by White [85] and Larsson et al. [37].

The conservation of momentum can be derived from Newton's second law

$$\mathbf{F} = m\frac{\partial \mathbf{u}}{\partial t}. \tag{5.4}$$

For a fluid particle it is customary to divide by the volume of the particle and use the density, so

$$\rho\frac{D\mathbf{u}}{Dt} = \mathbf{f} \tag{5.5}$$

in which force $\mathbf{f}$ is the applied force per unit volume, and can be split into pressure forces, body forces and viscous forces [37].

Using the net force acting on a fluid element caused by the stresses it can be shown that the conservation of momentum is

$$\frac{D\mathbf{u}}{Dt} = \mathbf{f} - \frac{1}{\rho}\nabla p + \nu\nabla^2\mathbf{u} \tag{5.6}$$

or

$$\rho\frac{\partial \mathbf{u}}{\partial t} + \rho\mathbf{u} \cdot \nabla\mathbf{u} = \rho\mathbf{g} - \nabla p + \mu\nabla^2\mathbf{u} \tag{5.7}$$

for an incompressible flow with constant viscosity, and with only gravity as body force. These equations are known as the Navier-Stokes equations, a more detailed derivation can be found in appendix B.

5.2   Numerical modeling

To solve the flow numerically a number of methods is available. First of all the entire flow, including all the turbulent scales, can be calculated according to the Navier-Stokes equations. This is called a Direct Numerical Simulation (DNS) method. Due to the demand for large memory and computational time this is not possible for a ship flow with modern day computers. To be able to reduce the computational effort, modeling of the turbulence of the flow is needed. One method is to solve the large turbulent scales (the grid size motion) using the Navier-Stokes equations, and model the effect of small scale turbulence (the sub-grid scale motions). This method

of solving a flow is called Large Eddy Simulation (LES). However still the computational demands are to large for application in practical ship design. Therefore in most cases an additional modeling step is taken and use is made of Reynolds Averaged Navier-Stokes (RANS) equations. Here all the fluctuations in the flow due to turbulence are modeled and the Navier-Stokes equations are only used to calculate the mean flow [37]. The CFD code used in this work, ReFRESCO, is described in section 5.8.1.

5.3 RANS equations

In the RANS (Reynolds Averaged Navier-Stokes) approach the mean flow is calculated by solving the Navier-Stokes equations, and the turbulence fluctuations in the flow are modeled. This is achieved by averaging the Navier-Stokes equations over a time scale larger than the largest turbulence scale, but smaller than the time scale of the mean flow [37]. This time averaging is achieved by making use of a Reynolds decomposition, which decomposes the velocity field, pressure and body forces in a mean and a fluctuating part [77],

$$u_i = \bar{u}_i + u_i' \tag{5.8}$$

$$p = \bar{p} + p' \tag{5.9}$$

$$f_i = \bar{f}_i + f_i'. \tag{5.10}$$

Using this composition the Navier-Stokes equations can be rewritten to the RANS equations,

$$\frac{\partial \bar{u}_i}{\partial x_i} = 0 \tag{5.11}$$

$$\frac{\partial \bar{u}_i}{\partial t} + \bar{u}_j \frac{\partial \bar{u}_i}{\partial x_j} = \frac{1}{\rho} \frac{\partial}{\partial x_i} \left(-\bar{p}\delta_{ij} + \mu \frac{\partial \bar{u}_i}{\partial x_j} - \rho \overline{u_i' u_j'} \right) + \bar{f}_i. \tag{5.12}$$

or

$$\rho \frac{D\bar{\mathbf{u}}}{Dt} + \rho \frac{\partial}{\partial x_j} \left(\overline{u_i' u_j'} \right) = \rho \mathbf{f} - \nabla \bar{p} + \mu \nabla^2 \bar{\mathbf{u}} \tag{5.13}$$

in which $\bar{\mathbf{u}}$ is the time averaged velocity defined as

$$\bar{\mathbf{u}} = \lim_{T \to \infty} \frac{1}{T} \int_{t_0}^{t_0+T} \mathbf{u} dt. \tag{5.14}$$

If the flow is unsteady, ensemble averaging is used instead of time averaging to prevent the disappearance of variations of the mean flow,

$$\bar{\mathbf{u}} = \lim_{N \to \infty} \frac{1}{N} \sum_{n=1}^{N} \mathbf{u}. \tag{5.15}$$

in which N is the number of members in the ensemble [11]. Together with the conservation of mass these two equations form the so called unsteady Reynolds Average Navier-Stokes, or RANS, equations. The $\overline{u_i' u_j'}$ term, the so-called inertia tensor, represents the mean transport of fluctuating momentum by turbulent velocity fluctuations [85]. Since this term is not negligible and an analytic form is unknown this term leads to the closure problem of turbulence. There are more unknowns than equations, so modeling of turbulence is needed to find a solution. This modeling is reviewed in depth in section 5.4.

A detailed derivation of the RANS equations can be found in appendix C.

Equation 5.13 can be rewritten to

$$\rho \frac{D\bar{\mathbf{u}}}{Dt} = \rho \mathbf{g} - \nabla \bar{p} + \nabla \cdot \tau_{ij} \tag{5.16}$$

with

$$\tau_{ij} = \mu \left(\frac{\partial u_i}{\partial x_j} + \frac{\partial u_j}{\partial x_i} \right) - \rho \overline{u_i' u_j'}. \tag{5.17}$$

Here the turbulent inertia terms are written as if they are stresses. The turbulent inertia stress behaves mathematically as if the total stress consists out of newtonian viscous stress (the first term) plus an additional turbulent stress tensor (the second term) [85]. This second term, $\rho \overline{u_i' u_j'}$, is also known as the Reynolds stresses.

5.4 Turbulence models

Turbulence models are needed to close the system of equations. Attempts are made to define a turbulence conservation relation, next to the conservation laws given before. A relation for the turbulent kinetic energy k is given by [85],

$$k = \frac{1}{2} \overline{u_i' u_i'} = \frac{1}{2} \left(\overline{u_1' u_1'} + \overline{u_2' u_2'} + \overline{u_3' u_3'} \right). \tag{5.18}$$

Here use is made of the Einstein summation convention, where repeated indices imply summation. From this a turbulence kinetic energy relation for an incompressible fluid can be derived [85],

$$\underbrace{\frac{Dk}{Dt}}_{\text{change of turbulent energy}} = -\frac{\partial}{\partial x_i} \underbrace{\overline{\left[u_i' \left(\frac{1}{2} u_j' u_j' + \frac{p'}{\rho} \right) \right]}}_{\text{convective diffusion}} - \underbrace{\overline{u_i' u_j'} \frac{\partial \bar{u}_j}{\partial x_i}}_{\text{production}} +$$

$$\underbrace{\frac{\partial}{\partial x_i} \left[\nu u_j' \left(\frac{\partial u_i'}{\partial x_j} + \frac{\partial u_j'}{\partial x_i} \right) \right]}_{\text{work done by turbulent viscous stresses}} - \underbrace{\nu \overline{\frac{\partial u_j'}{\partial x_i} \left(\frac{\partial u_i'}{\partial x_j} + \frac{\partial u_j'}{\partial x_i} \right)}}_{\text{turbulent viscous dissipation}}. \tag{5.19}$$

To compute these terms models are needed. Turbulence models can be divided in five classifications [37]:

1. zero-equation model: no transport equation is used for turbulent quantities,

2. one-equation model: uses one transport equation for turbulence,

3. two-equation model: uses two transport equations,

4. Reynolds stress models (RSM),

5. algebraic stress models (ASM).

The first three models are based on the Boussinesq hypothesis from 1877, the last two make use of a more extended modeling. The models are described in the following sections.

5.4.1 Boussinesq hypothesis

The Boussinesq hypothesis states that the Reynolds stresses $\rho \overline{u_i' u_j'}$ can be computed from the rate of strain tensor S_{ij} in a way similar as the viscous stresses [3]. Based on the fact that

$$\rho \overline{u_i' u_i'} = -2\rho k \tag{5.20}$$

the Boussinesq hypothesis may be written as

$$\rho \overline{u_i' u_j'} = \mu_T \left(\frac{\partial \bar{u}_i}{\partial x_j} + \frac{\partial \bar{u}_j}{\partial x_i} \right) - \frac{2}{3} \rho k \delta_{ij}, \tag{5.21}$$

[37], in which δ_{ij} is the Kronecker delta such that

$$\delta_{ij} = \begin{cases} 1, & \text{if } i = j, \\ 0, & \text{if } i \neq j. \end{cases} \tag{5.22}$$

The turbulent viscosity μ_T is unknown and not a physical constant such as μ, therefore it must be calculated at each point in the flow.

5.4.2 Zero-equation models

In a zero-equation model algebraic equations are used to calculate the turbulent quantities. The most common approach to use is mixing length models. Here the length scale is prescribed analytically and the velocity scale is calculated as the length scale times the dominant velocity gradient. These models were developed for thin shear layers where the only important velocity derivative is perpendicular to the surface [37]. One of most used models is the Baldwin-Lomax model.

5.4.3   One-equation models

Zero-equation models cannot compute the turbulent energy k or the fluctuating components, therefore additional partial differential equations are needed. One-equation models are a potential solution for this problem, a number of models were developed which solve a transport equation for k. Often again the length scale is prescribed analytically in such models. Since this causes additional difficulties this type of models is no longer popular [37].

A different model is the Spalart-Allmaras turbulence model, here a transport equation for the quantity ν is used. This quantity is closely related to the turbulent viscosity. This model is more popular, however the model does depend on eight empirical constants which must be varied to obtain good results [37, 85].

5.4.4   Two-equations models

In two equation models it is assumed that two independent scales are needed to statistically describe turbulence, to this end two equation models have been developed. The two scales are obtained from two independent transport equations. Often a transport equation for the turbulent kinetic energy k is used, since this is easily modeled. The second equation is mainly based on dimensional arguments [50]. Three two-equation models are discussed here, the $k - \epsilon$, the $k - \omega$ model and the $k - \sqrt{k}L$ model.

$k - \epsilon$ model

One of the most common models is the $k-\epsilon$ turbulence model, proposed by Launder and Spalding [38]. This model solves a transport equation for the turbulent kinetic energy k, and solves a similar equation for the rate of change of the turbulent dissipation ϵ.

While the $k-\epsilon$ model is popular it has some downsides in modeling wall attached flows. It is known that the detailed features of the ship wake cannot be obtained using this model, since irregular wake contours are smoothed out. The model is not suitable for flows with strong stream-wise vorticity, which generally dominates a ship's wake [37]. Also the model behaves well in the wake of the boundary layer, but not in the logarithmic region of the boundary layer, this often implies the use of a wall function in conjunction with this model [67].

$k - \omega$ model

To be able to resolve the problems described for the $k-\epsilon$ model, Wilcox [86] suggested the $k - \omega$ model. In this model an equation for the specific dissipation rate

$$\omega = \frac{\epsilon}{k} \tag{5.23}$$

is solved, rather than for the dissipation rate ϵ.

A downside to this model is that it is difficult to define a boundary condition at the outer edge for the specific dissipation rate equation, consequently the model is sensitive for the inflow boundary condition. A proposed solution to this problem is the use of a Baseline $k - \omega$ model, where the transport equations are combined so that ω is represented at the surface, and ϵ outside of the boundary layer. This model is first suggested by Menter [47]. He also suggested a further modification which improved the prediction of the principal shear stress in adverse pressure gradients. This model is known as the Menter Shear Stress Transport (SST) model [37].

$k - \sqrt{k}L$ model

The $k - \sqrt{k}L$ (KSKL) turbulence model was proposed by Menter et al. [50]. It is based on the $k - kL$ model as proposed by Rotta [71] which makes use of an exact transport equation for a turbulent length scale L. The model is a two-equation turbulence model which takes also higher order velocity derivatives into the turbulent length scale equation.

The model makes use of a transport equation for the turbulent kinetic energy k and a transport equation for $\sqrt{k}L$ in which L is the turbulent length scale. The turbulent length scale describes the size of the large energy containing eddies. Also the Von Kármán length scale, defined as

$$L_{vK} = \kappa \left| \frac{U'}{U''} \right| \tag{5.24}$$

arises in the equations. To obtain asymptotic turbulence behavior near a wall a viscous sublayer model is implemented to include additional near wall damping terms.

Due to the inclusion of the Von Kármán length scale (L_{vK}) the unsteady behavior changes with respect to classical URANS (unsteady RANS) models. The Von Kármán scale adjust to the smallest scales and produces an eddy viscosity small enough to allow the formation of even smaller eddies until the grid limit. It allows the formation of a turbulent spectrum within the limits specified by the numerical method, the grid and time step. An eddy viscosity small enough to allow further cascading to smaller scales is also formed, due to the grid limit the energy accumulates at the high wave number limit [49]. Therefore the model could lead to a LES-like behavior in unsteady flow regions, and RANS capability in attached flow regions. This ability is known as Scale-Adaptive Simulation (SAS) capability. This behavior is similar to a Detached Eddy Simulation (DES), however on a different basis and modeling [49]. A DES makes use of RANS in the attached flow regions and a LES modeling in unsteady regions [74]. Since the $k - \sqrt{k}L$ model does not use a LES modeling the grid sensitivity of DES in the RANS regime is avoided [48]. An advantage of this is that the model can be applied to higher Reynolds numbers than a LES method, and the wall bounded flow solution is less dependent on the local grid refinement in the wall-normal direction. For the flow around rigid bodies

it is often found that the $k - \sqrt{k}L$ model is in better agreement with experimental data than classical unsteady RANS [17, 50].

Menter et al. [50] states that the $k - \sqrt{k}L$ model gives a more accurate prediction of the spread of a round jet than a SST or Spalart-Allmaras model in a steady state simulation.

5.5   Reynolds stress model

The assumption that the stress tensor is proportional to the rate of strain tensor is true for viscous stresses, but not generally for turbulent stresses. As a consequence models are developed which do not rest upon the Boussinesq hypothesis: Reynolds Stress Models (RSM).

A Reynolds stress model consists of transport equations for each of the six Reynolds stress components. It is a second-order modeling scheme, where the Reynolds stresses are calculated directly. The stresses can be calculated either using an algebraic model (see section 5.6) or a differential equation for the rate of change of the stress. The Reynolds stress equation can be split into turbulent transport, production, pressure-strain and dissipation terms [85]. This distribution in terms is not unique, for instance Pope [60] uses a slightly different formulation.

The dissipation, turbulent transport and pressure-strain are all three statistical correlations and are difficult or, in the case of the pressure-strain, impossible to measure. As a consequence additional modeling is needed for these terms. Often an additional equation for ϵ is needed, k can be obtained from the normal Reynolds stresses. A number of these models are described in White [85] and Pope [60].

It is expected that these models are more accurate due to the fact that the physics are more closely resembled, however the computational effort is increased due to the increased number of equations which must be solved [37, 85].

5.6   Algebraic stress model

The Reynolds stress model can more accurately describe the physics, however it requires three to six additional partial differential equations which makes it computationally expensive. To reduce the computational cost the differential equation can be replaced by an Algebraic Stress Models (ASM), where an algebraic approximation for the transport terms is used [60]. This results in a nonlinear set of algebraic equations, which not necessarily depends on the turbulent viscosity. A consequence of this approximation is that an algebraic stress model is less general and accurate than a Reynolds stress model. Examples of algebraic stress models are the models by Rodi [69], Wallin and Johansson [83] and Dol et al. [12].

Next to the approximation for the transport term additional three-dimensional correlations are needed for the dissipation and pressure-strain terms. White [85] states that presently algebraic stress models are not popular especially for separating and reattaching flows.

The algebraic stress model must be used together with a two equation model and usually includes equations for k and either ϵ or ω. The algebraic Reynolds stress model implemented in ReFRESCO 2.3.0 is the model by Dol et al. [12] which is based on the model by by Wallin and Johansson [83]. The Explicit Algebraic Reynolds Stress Model (EARSM) is based on a Turbulent/Non Turbulent (TNT) $k - \omega$ turbulence model .

5.7 Multiphase modeling

CFD models describing multiphase flows can be divided into Euler-Euler, Euler-Lagrange and mixture flow models. The difference between these models lies in the way in which the dispersed phase is modeled. In this section an overview of the different methods and their properties is given. The focus lies on the dispersed flow regime as described in chapter 4, and the models applicable for this flow regime.

For reference a visual interpretation of the different models is given in figure 5.1.
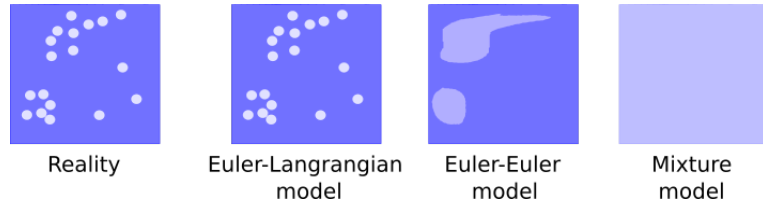
Figure 5.1: A visualization of the differences between an Euler-Lagrangian model, an Euler-Euler model and a mixture model. In this figure a liquid with a number of dispersed bubbles is shown.

5.7.1 Euler-Lagrangian models

The Euler-Lagrangian model makes use of a single set of conservation equations for the liquid phase. The bubbles (or particles) are tracked by solving their equation of motion in a Lagrangian frame of reference, so following the flow. Separate models for drag, lift, added mass and the Basset history forces can be used to model the interaction between the liquid and the gas. To model this interaction a distinction between one-, two- and four-way coupling can be made, the interested reader is referred to Rafique et al. [61] for more details. The advantage of this model lies in the fact that physical phenomena like bubble-bubble, bubble-liquid interactions, bubble breakup and coalescence, can be modeled. The downside of this model is that only flows with a limited gas volume fraction can be modeled (at maximum 5%), and only a limited number of bubbles can be tracked due to high computational demands [61]. Due to this limitation this model is not applicable for the current research.

5.7.2 Euler-Euler models

In the Euler-Euler model both the gas and liquid phase are calculated in the Eulerian frame of reference (the general frame of reference). The individual bubbles are not tracked, but an averaged description of each element of finite volume of the space domain is calculated. Each element contains a fraction of the continuous and a fraction of the dispersed phase. For each phase the conservation of mass and conservation of momentum are solved. The momentum equations are coupled using interface momentum exchange terms which model the interactions between both phases [61]. Again due to high computational demands this method is less suitable for the current research.

5.7.3 Mixture models

In mixture models each cell contains a mixture of two phases, and for the mixture phase a single set of mass and momentum equations is solved. The relative motion of each phase with respect to the center of mass of the mixture is known as the 'diffusion' of that phase [61]. A group of mixture models are developed based on the assumption of a local equilibrium. These models differ on the exact formulation used to determine the velocity differences [42]:

- the drift-flux model [89],

- the mixture model [25],

- the algebraic-slip model [61],

- the suspension model/approach [82],

- the diffusion model [25, 76],

- the local-equilibrium model [27].

In this study a restriction is made to the mixture model known as the Volume of Fluid method since this is the model which is implemented in ReFRESCO. The interested reader is referred to the given references for more information concerning the other models.

In the Volume of Fluid method the fluid is treated as a single continuum and no slip between the phases is assumed. The following section is based on the description given by Rijpkema [67].

In this model the volume fraction α_i is defined as

$$\alpha_i = \frac{\mathcal{V}}{\sum\limits_{i=1}^{n} \mathcal{V}_i} \tag{5.25}$$

in which $\mathcal{V}$ is the total volume, $\mathcal{V}_i$ the volume of each phase and n the number of phases. The mixture density ρ_m is given by

$$\rho_m = \sum_{i=1}^{n} \alpha_i \rho_i. \tag{5.26}$$

The mixture viscosity μ_m is given by

$$\mu_m = \sum_{i=1}^{n} \alpha_i \mu_i \tag{5.27}$$

and

$$\sum_{i=1}^{n} \alpha_i = 1. \tag{5.28}$$

If isothermal behavior is assumed the properties of each phase are constant. For a two phase flow the continuity equation can be rewritten using relations 5.26, 5.27 and 5.28. Under the assumption of incompressibility the transport equations for the volume fraction of gas and liquid can be obtained,

$$\frac{\partial \alpha_g}{\partial t} + \frac{\partial (\alpha_g u_i)}{\partial x_i} = \frac{S}{\rho_g} \tag{5.29}$$

$$\frac{\partial \alpha_l}{\partial t} + \frac{\partial (\alpha_l u_i)}{\partial x_i} = -\frac{S}{\rho_l}. \tag{5.30}$$

Here S is a source term to take the creation or destruction of gas into account, for instance when cavitation is modeled. If no gas is created or destroyed $S = 0$.

5.7.4 Multiphase turbulence modeling

For turbulence modeling in multiphase flows again a division can be made in Euler-Lagrangian methods, Euler-Euler methods and mixture models. Since the used code is a mixture model, only turbulence modeling for these models is described.

In a mixture model only the single phase equations are solved for the mixture phase, therefore any single phase turbulence model, as described in section 5.4, can be used. However these models are in most cases developed for single phase flows, therefore at the interface unexpected effects can occur. For example Coutier-Delgosha et al. [8] describe the influence of the used turbulence model on the results of their test case. Also questions exist concerning the production of eddy viscosity around an interface.

As a consequence the influence of the turbulence model on the results for this work must be looked into.

5.8 Numerical implementation

A description of the used CFD code is given here. The reasoning behind the choice of this code is given, and the implementation of the equations in the code is illustrated.

5.8.1   ReFRESCO background

The following description is taken from MARIN [45]. More details can be found on the ReFRESCO website, www.refresco.org.

Reliable and Fast Rans Equation Code for Ships and Constructions Offshore (Re-FRESCO) is a community based open-usage CFD code for the Maritime World. It solves multiphase (unsteady) incompressible viscous flows using the Navier-Stokes equations, complemented with turbulence models, cavitation models and volume-fraction transport equations for different phases [81]. The equations are discretised using a finite-volume approach with cell-centered collocated variables, in strong-conservation form, and a pressure-correction equation based on the SIMPLE algorithm is used to ensure mass conservation [31]. Time integration is performed implicitly with first or second-order backward schemes.

The implementation is face-based, which permits grids with elements consisting of an arbitrary number of faces (hexahedrals, tetrahedrals, prisms, pyramids, etc.), and if needed h-refinement (hanging nodes). State-of-the-art CFD features such as moving, sliding and deforming grids, as well automatic grid adaptation (refinement and/or coarsening) are also available. For turbulence modeling, both RANS/Unsteady Reynolds Averaged Navier-Stokes (URANS) and Scale-Resolving Simulations (SRS) models such as SAS, DDES/IDDES, XLES, PANS and LES approaches can be used.

ReFRESCO (v2.3.0) is currently being developed, verified and its several applications validated at MARIN (in the Netherlands) [15, 30, 32, 66, 72, 75, 87] in collaboration with IST (in Portugal) [58], USP-TPN (University of Sao Paulo, Brasil) [70], TUDelft (Technical University of Delft, the Netherlands) [31], UoS (University of Southampton, UK) [20], UTwente (University of Twente, the Netherlands) [28], Chalmers (Chalmers University, Sweden) [19], UMaine (University of Maine, USA) [46], Texas A&M (Texas A&M University, USA), UPB (Universidad Pontificia Bolivariana, Colombia) [62] and WUR (Wageningen University and Research, the Netherlands).

5.8.2   Discretization of the governing equations

Rijpkema [67] gives a description of the numerical modeling used in ReFRESCO, this section is based on his description.

A general conservation equation for a flow property ϕ in integral form can be given by the equation

$$\frac{\partial}{\partial t}\underbrace{\iiint_V \rho\phi\,\mathrm{d}V}_{\text{unsteady term}} + \underbrace{\iint_S \rho\phi\mathbf{V}\cdot\mathbf{n}\mathrm{d}S}_{\text{convection term}} = \underbrace{\iint_S \Gamma\nabla\phi\cdot\mathbf{n}\mathrm{d}S}_{\text{diffusion term}} + \underbrace{\iiint_V q_\phi\mathrm{d}V}_{\text{source term}} \qquad (5.31)$$

in which $\mathbf{V}$ is the velocity vector, $\mathbf{n}$ the normal vector, Γ a diffusive coefficient and q_ϕ a source or sink term acting on the volume.

The source term is discretized as

$$\iiint\limits_V q_\phi \mathrm{d}V \approx q_{\phi_c} \Delta V. \tag{5.32}$$

The property is expressed as a product of the value at the cell center and the cell volume, if expressed this way the property has a second order accuracy.

The unsteady term is discretized as

$$\frac{\partial}{\partial t} \iiint\limits_V \rho \phi \mathrm{d}V = \iiint\limits_V \frac{\partial (\rho \phi_c)}{\partial t} \mathrm{d}V \approx \frac{3 (\rho \phi_c)^n - 4 (\rho \phi_c)^{n-1} + (\rho \phi_c)^{n-2}}{2 \Delta t} \Delta V. \tag{5.33}$$

Here for the time discretization an implicit three time level discretization (second order backward) is used. This is an unsteady approach, this can be used for steady as well as unsteady problems.

The convection term is discretized as

$$\iint\limits_S \rho \phi \mathbf{V} \cdot \mathbf{n} \mathrm{d}S \approx \sum_{i=1}^{N_f} \phi_{f_i} (\rho \mathbf{V} \cdot \mathbf{n})_{f_i} S_{f_i}. \tag{5.34}$$

The discretization is the value at the face center times the face area. In this equation the term $\rho \mathbf{V} \cdot \mathbf{n}$ is also known as the flux $\mathbf{F}_f$.

The diffusion term is discretized as

$$\iint\limits_S \Gamma \nabla \phi \cdot \mathbf{n} \mathrm{d}S \approx \sum_{i=1}^{N_f} \Gamma_{f_i} (\nabla \phi \cdot \mathbf{n})_{f_i} S_{f_i}. \tag{5.35}$$

The discretization is done by using the discretized gradient on the cell faces. Linear interpolation between two neighbor cell center values is used to determine the gradient. The discretization expressed in this way has a second order accuracy.

5.8.3 Mixture equations

In ReFRESCO the multiphase flow is modeled by solving transport equations for a single continuum mixture fluid, therefore besides the velocity V and the pressure p, the density ρ and the viscosity μ may vary in time and space. The equations which describe this can be found in section 5.7.3 [81]. It is assumed that the process is iso-thermal, so the density and viscosity of each phase are constant.

5.9   Numerical uncertainty

Similarly to experimental work, numerical results are subjected to error. It is generally accepted that numerical error consists of three elements: the round-off error, the iterative error and the discretization error [68]. Determining the numerical error is necessary to verify the results, so to check whether the equations are solved right [66]. Next to numerical error there is also the modeling error, which relates tot the question whether the right equations are solved [66]. This can be addressed by validating the results with experiments, as is described in section 5.10.

5.9.1   Round-off error

The round-off error is a consequence of finite precision of computers. Its importance tends to increase with grid refinement, but the error is usually negligible compared to the other sources of error due to double-precision arithmetic [14, 16].

5.9.2   Iterative error

The iterative error is caused by the to non-linearity of the equations which are solved, mainly in the convective terms and the turbulence closure model [14]. The iterative error is commonly based on the L_2 or L_{inf} norms of either the differences between iterations or the normalized residuals. The norms are defined as

$$L_2 = \sqrt{\frac{\sum_{i=1}^{N_p} (|\Delta\phi_i|)^2}{N_p}} \qquad (5.36)$$

which is in effect a root mean square value of $\Delta\phi$ and

$$L_\infty = \max\left(|\Delta\phi_i|\right) \qquad (5.37)$$

which is a maximum local change of flow quantity between two consecutive iterations in one grid cell. These two quantities can be interpreted as an indication of the convergence in the entire domain (the L_2 norm) and the lowest convergence which is present at a single location in the domain (the L_∞ norm). Eça and Hoekstra [14] states that the most appropriate norm to estimate the iterative error is the L_∞ norm. The iterative error can be brought down to the level of round-off error, however computational cost makes this not always feasible nor achievable for industrial problems. To obtain a negligible effect of the iterative error the error should be at least two to three orders of magnitude smaller than discretization error [14, 16]. To estimate the uncertainty the module *Numerical Uncertainty Analysis* of MARIN is used [43, 44].

5.9.3 Discretization error

Thirdly there is the discretization error, which is caused by the approximations made in discretizing the partial differential equations to obtain a system of equations and the finite resolution of the grid [16, 66, 68].

To estimate the discretization error the method as described by Rosetti et al. [70] is used. This method is similar to the method of Eça and Hoekstra [16], however it is extended for unsteady simulations. The uncertainty is estimated based on grid and time step refinement.

Using this method the solution can be verified. For this method at least six data points are needed. These data points must vary in grid and in time step. The various grids must be geometrically similar. Ideally each grid has a refinement factor (h_i/h) of 2 relative to the previous grid, however to limit the computational costs lower refinement factors are used. This influences the geometrical similarity, since due to these factors some round off errors arise in the number of grid cells in different directions.

In the method a least squares fit on the data is made based on a power series expansion which is based on the cell size and time step size. The used expansions are based on first-order, second-order, first- and second-order and p-order terms. The expansions are determined both with and without weights. The quality of the fit is determined using the standard deviation of the fit, depending on this quality a safety factor is selected and the uncertainty is estimated. The fit which is obtained is both dependent on time and grid, so the fit is a plane in a three dimensional domain. To estimate the uncertainty the module *Numerical Uncertainty Analysis* of MARIN is used [43, 44]. The method is described in detail in appendix F.

5.10 Validation method

To determine whether a result is validated the method described by Rijpkema and Vaz [66] is used. In this method the validation uncertainty

$$U_{val} = \sqrt{U_\phi^2 + U_{inp}^2 + U_{exp}^2} \tag{5.38}$$

is compared with the validation comparison error

$$E = \phi_i - \phi_{exp}. \tag{5.39}$$

Here U_{inp} is the parameter uncertainty in the input (so uncertainties in the fluid properties, flow geometry and boundary conditions), U_{exp} is the experimental uncertainty and ϕ_{exp} is the experimental value. The validation depends on the result of the comparison:

- If $|E| > U_{val}$, the model must be improved since the comparison error is probably dominated by the modeling error.

- If $|E| < U_{val}$, the modeling error is within the range imposed by the three uncertainties. This means either that, if $|E|$ is considered to be sufficiently small, the model and solution are validated against the given experiment, or that the quality of the numerical solution and/or experiment should be improved. If the model and solution are validated the determined uncertainty U_{val} must be taken into account for the result.

Chapter 6

Rising bubble

The first validation case is the modeling of a single rising gas bubble in a liquid. This case is used to see how well the code performs for a single bubble, and to see which forces are relevant for this case. A spherical bubble is released 40 cm below the water surface, and rises to the surface due to buoyancy. The results are compared with bubble shapes as predicted by Hua and Lou [22]. This comparison is done quantitatively, no systematic study into the effect of time steps, grid, discretization schemes, etc. was performed. Three different bubble dimensions are used.

6.1 Background literature

Hua and Lou [22] used a front tracking method to model single bubbles rising in water due to buoyancy. An ideal spherical bubble is located initially at two bubble diameters above the bottom. At the initial condition it is assumed that the liquid and bubble are stationary. An overview of different predicted bubble shapes for a range of Reynolds and Bond numbers is given, these shapes are compared with experiments. Also the evolution of the shape over time is given.

Hua et al. [23] used a DNS method to model air bubbles in water over a range of Reynolds and Bond numbers. The numerically determined terminal velocity was compared with experimental measurements for bubbles with initial diameters ranging from 0.5 mm to 30 mm. Also the effect that bubbles at high Reynolds numbers do not rise in a straight line but rather follow a more zigzag or spiral path due to pressure fluctuations in the wake of the bubble was shown with the modeling. Finally the interaction and merging between two rising bubbles with a different size was looked into, both the effect on velocity and on bubble shape were given.

Mudde and Simonin [55] used an ensemble-averaged form of the Eulerian two-fluid equations to model a rising bubble column in a rectangular domain filled with fluid. The modeling is done in both 2D and 3D. Velocity fields and gas fraction distribution plots were given.

6.2   Modeled forces

Section 4.1 gives an overview of all different forces which act on a bubble, including an assessment of their influence. The forces modeled in the current analysis are:

- drag force,

- added or virtual mass force,

- gravitational force,

- buoyancy force.

The forces which are neglected, and the reasoning being this, are:

- Basset, or history, force, this is only relevant for high accelerations and difficult to implement since ReFRESCO is a mixture model where the bubbles are not explicitly tracked,

- collision force, not possible to accurately model since ReFRESCO is a mixture model where the bubbles are not explicitly tracked,

- surface tension, since this force is negligible compared to the inertial and gravitational forces, this is also not implemented yet in ReFRESCO,

- lift force, since this only occurs in slow viscous flows, which is not the case for a submerged exhaust.

6.3   Results

The dimensions and the dimensionless numbers of the bubbles can be found in table 6.1. The Reynolds number and Bond number are calculated according to the definition given by Hua and Lou [22]. The Reynolds number (the ratio between inertial and viscous forces) is then defined as

$$Re^* = \frac{\rho_l g^{\frac{1}{2}} D^{\frac{3}{2}}}{\mu_l} \tag{6.1}$$

and the Bond number (the ratio between body forces and surface tension) as

$$Bo^* = \frac{\rho_l g D^2}{\gamma}. \tag{6.2}$$

In ReFRESCO surface tension is not modeled, therefore for the modeled bubbles the Bond number is infinitely large. The absence of surface tension is expected to be valid, since this force is dominant only for small bubbles (diameter in the order of 10^{-3} m). The value of the Bond number shown in table 6.1 is calculated with a value of the surface tension $\gamma = 0.063$ N/m.

Table 6.1: Modeled bubbles.

Property		Bubble 1	Bubble 2	Bubble 3
Radius	[m]	0.002	0.005	0.05
Height	[m]	0.002	0.005	0.05
Re^*	[-]	$2.3 \cdot 10^2$	$9.2 \cdot 10^2$	$2.9 \cdot 10^4$
Bo^*	[-]	0.6	3.9	390

The simulation is performed on the grid SysVar1, which is described in section 7.6. The used discretization scheme for the momentum equation is the QUICK scheme. Using these settings and a time step of 0.01 s the Courant number in the domain is in the range 1-2, with a peak value of 6 at the edge of the bubble when it is released. The iterative error for a number of representative time steps is shown in figure 6.1. It can be seen that for later time steps all L_∞ norms are below 10^{-3}, and the L_2 norms are at least two orders of magnitude lower. For the first time steps, when the bubble is just released and accelerates, the convergence is less and the solution oscillates.
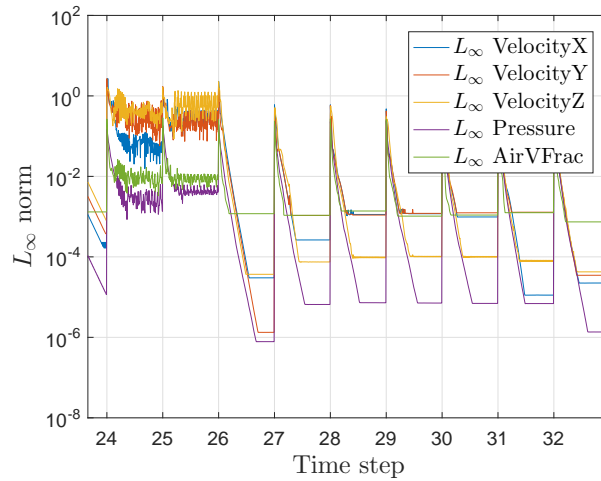
Figure 6.1: Convergence behavior for the rising bubble. A number of representative time steps are shown.

The development of the cross section of the bubble shape of the bubble with $D = 0.05$ m is shown in figure 6.2, the shape of the bubble is shown in figure 6.3. It can be seen that the bubble breaks up quickly and that the air concentrates in a ring with a diameter larger than the original bubble. This shape is known as a toroidal bubble. This behavior can also be observed for the bubbles with a smaller initial diameter.

The computed shape is compared with the predicted shapes as function of Re^* and Bo^* as shown by Hua and Lou [22]. Based on the values of the dimensionless
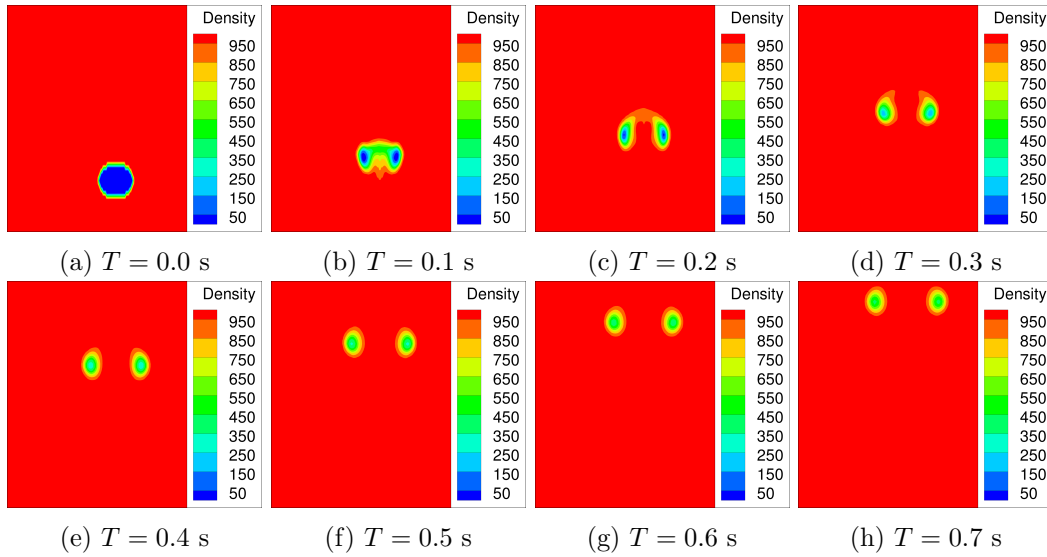
Figure 6.2: Development of the bubble cross section of a bubble with $D = 0.05$ m from $T = 0$ s until $T = 0.7$ s. A cross section of the bubble is shown.
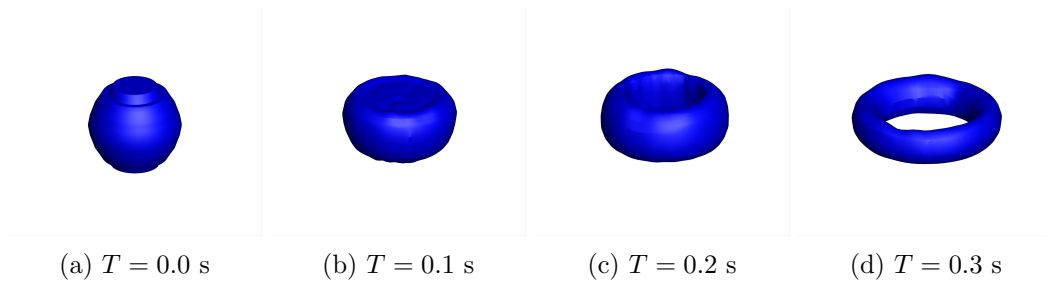
Figure 6.3: Development of the bubble shape of a bubble with $D = 0.05$ m from $T = 0$ s until $T = 0.3$ s. A isosurface of the density with $\rho = 500$ km/m^3 is shown.

numbers, for the modeled case for $D = 0.05$ m toroidal bubbles are expected. For the two smaller bubbles either spherical or somewhat elliptical shapes are expected.

It is concluded that the results of the computations for the large bubble are in agreement with the results given in literature, however the smaller bubbles are not. This discrepancy is attributed to the lack of surface tension in ReFRESCO. There is no force to keep the bubbles together, therefore also smaller bubbles break up into a toroidal shape. It is known that surface tension plays a more important role for smaller diameter bubbles, so it can be expected that these results are not in agreement with the predicted shapes. See section 4.3 for more details. The absence of surface tension also enables the air to continue into the domain, whereas the shapes given by Hua and Lou [22] are terminal bubbles shapes.

Since the diameter of the bubbles for a submerged exhaust are in the range of the largest bubble modeled here it is concluded that ReFRESCO can probably be used for this purpose.

Chapter 7

Turbulent jet

The second modeled case is a turbulent jet through a single nozzle. This case can be seen as a simplified form of the configuration on a submarine. The exhaust there is a combination of multiple nozzles located close to each other. First a theoretical description is given, after which the modeled situations and the numerical results are described.

7.1 Theoretical description

Cushman-Roisin [9] looked into turbulent jets in a fluid. This section is based on that work. The terminology as used in this thesis is shown in table 7.1. In all cases investigated in this thesis both momentum and buoyancy play a role and the injection is continuous.

Table 7.1: Types of intrusions of a fluid into another and the corresponding terminology [9].

	Continuous injection	Intermittent injection
Momentum only	Jet	Puff
Buoyancy only	Plume	Thermal
Both momentum and buoyancy	Buoyant jet or forced plume	Buoyant puff

It is stated that laboratory investigations of jets penetrating into a quiescent fluid of the same density show that the turbulence caused by the jet is contained in an conical shape. The spreading angle is 11.8°, or approximately 24° from side to side. Based on this the jet radius R can be approximated using the equation

$$R(x) = \frac{1}{5}x \tag{7.1}$$

in which x is the distance from the outlet. This distance must be taken $\frac{5d}{2}$ into the outlet, due to the initial jet radius which is equal to half the exit diameter d.

Equation 7.1 is used for comparison purposes, although it is noted that is is based on two fluids of the same density, which is not the case for a submerged exhaust.

The cross-jet velocity profiles are similar to one another after averaging over turbulent fluctuations. The velocity profile across the jet has by approximation a Gaussian shape, so

$$u(x,r) = u_{max} \cdot e^{-\frac{r^2}{2\sigma^2}} \tag{7.2}$$

in which r is the cross-jet radial distance from its center line, u_{max} the maximum velocity at the center line, and $\sigma(x)$ is the standard deviation related to the spread of the profile across the center line. An exemplary velocity profile with an increasing distance from the origin are shown in figure 7.1. 4σ is the width of the distribution in which 95% of the curve is contained.
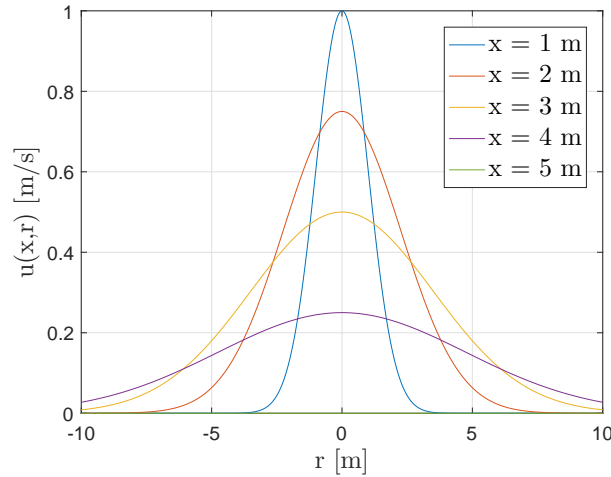
Figure 7.1: An exemplary velocity profile of a jet penetrating in a fluid at rest with increasing distance x from origin.

However, the spread of a jet is not as constant as stated by Cushman-Roisin [9]. It is shown that the mixing and entrainment of the jet, and therefore the flow dynamics are dependent on the shape of the nozzle and the Reynolds number of the flow [2, 51, 26]. An asymmetric nozzle introduces more mixing than an axisymmetric nozzle. Since the exhaust on the Walrus class consists of axisymmetric nozzles it is assumed that the model as presented here holds.

In the model by Cushman-Roisin [9] the velocity profile through the nozzle is uniform. It was shown that the this assumption is invalid [7, 36, 88]. Langman et al. [36] state that there is a clear difference between a jet flow from a long pipe (where a velocity profile has developed) or from a smooth contracting nozzle (where the velocity profile is more uniform). This is for a gas-gas or liquid-liquid jet. In the case of a gas jet in water however, there is also the influence of buoyancy. For such

a jet Morton [54] defined a length scale

$$l_m = \frac{M^{3/4}}{B^{1/2}} \tag{7.3}$$

in which M is the initial momentum flux and B the momentum produced by buoyancy. The length scale l_m controls the behavior (more like a plume or more like a jet) at a given distance from the source. If this ratio is much smaller than the distance along the plume (x) the initial momentum flux is dominated by the momentum produced by the buoyancy. For a source with a mass flux the momentum by buoyancy is defined as

$$B = \frac{g\left(\rho_a - \rho_o\right)Q}{\rho_o} \tag{7.4}$$

in which ρ_a is the ambient fluid density, ρ_o the source fluid density and Q the volume flux [40]. In the modeled situation l_m is in the order of 10^{-2} m on a plume length of 0.5 m. Consequently the buoyancy has a larger influence than the initial momentum flux, and it can be argued that influence of the exact velocity profile in the nozzle can be neglected. This hypothesis is checked in section 7.8.2.

7.2 Numerical settings

The flow through a single nozzle is investigated in a similar way as done by Norwood and Chen [57]. A buoyant jet is modeled in 3D in a cylindrical tank. For this case a number of parameters is varied, namely the grid size to estimate the discretization error, the density to look into the influence of the temperature of the exhaust gases and the volume flow of the exhaust gases to see the effect on the free surface. Also the influence of different turbulence models on the shape and spread of the plume is investigated. Based on this a turbulence model might be selected. For the first simulations no turbulence model is used, this is sometimes known as a implicit Large Eddy Simulation (iLES), a LES without a subgrid model. This implies that the large vortices can be solved and the effect of the smaller vortices is handled by numerical diffusion. The risk of this method is that the turbulence dissipation is based on numerical dissipation. As a consequence the result is very sensitive for the discretization method, the time step, the grid resolution, the Courant number and the convergence. To investigate whether the demands are met the spectrum of turbulence decay should be investigated, this is not done for these simulations.

The computational domain is a cylindrical tank with a radius of 0.5 m and a height of 1 m. A schematic of the domain can be found in figure 7.2, and an overview of the main settings in table 7.2. The container is filled with water to a height of 0.5 m. In the middle at the bottom a cylindrical nozzle is located, with a diameter and height of 0.010 m. As inflow a velocity is prescribed on the exit of the nozzle with an air volume fraction of 1 (pure air). The walls of the tank are modeled as a slip wall. This choice influences the result, since it allows for reflections. It is assumed that the walls are located sufficiently far to let the plume reach a fully developed

state before reflections influence the surface. The effect of this assumption and its validity are described in section 7.5. An overview of the main numerical settings used can be found in appendix D.
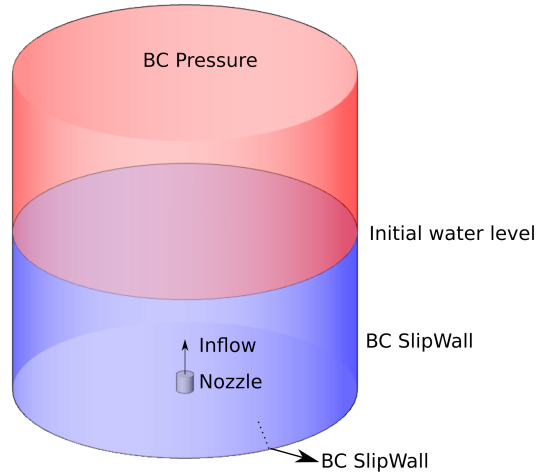
Figure 7.2: Computational domain for the turbulent jet. The red section is filled with air, the blue section with water.

7.3   General observations

As a measure to reduce the computational load the first test cases were taken by using half the domain, which was mirrored using a symmetry plane. It turned out that this simplification influences the solution.

The plume oscillates due to pressure differences surrounding the plume which are induced by the creation of vorticity. Due to the symmetry plane the oscillations in the plume are restricted to the plane of symmetry. As a consequence the spread in different directions differs and the cross-section of the plume becomes elliptical rather than circular.

To obtain accurate results for the spread it is therefore necessary to model the plume in a complete 3D domain.

The width of the plume is monitored on four different heights, at 0.1, 0.2, 0.3 and 0.4 m. A logical method to determine the width is based on the air volume fraction, however this proved to be unreliable. The inflow from the nozzle creates a cone of upwards flow, consisting of a mixture of water and air. The oscillations in the plume cause clustering in the air volume fraction. Based on the air volume fraction one might think that the plume is not present or is small, whereas there is a large region where the flow moves upwards and disturbs the surface.

Table 7.2: Main settings for the turbulent jet.

Description	Symbol	Value	Unit
Tank diameter	D	1	[m]
Tank height	H	1	[m]
Nozzle diameter	d	0.01	[m]
Nozzle height	h	0.01	[m]
Nozzle area	A_{nozzle}	$7.85 \cdot 10^{-5}$	[m^2]
Waterlevel height	H_0	0.5	[m]
Inflow velocity gas	V_{gas}	2.64	[m/s]
Density water	ρ_w	998	[kg/m^3]
Dynamic viscosity water	μ	$1.002 \cdot 10^{-3}$	[kg/(s m)]
Density air	ρ_a	1.2	[kg/m^3]
Dynamic viscosity air	μ	$1.8 \cdot 10^{-5}$	[kg/(s m)]
Reynolds number	Re	$8.3 \cdot 10^3$	[-]

An alternative method was used based on the magnitude of the vorticity according to the equation

$$|\omega| = \sqrt{\omega_x^2 + \omega_y^2 + \omega_z^2}. \tag{7.5}$$

The width is determined based on the points where the magnitude of the vorticity is larger than a threshold value. Since the water in the tank is stationary at the start the influence of the exact value of the threshold is limited. Inside the plume the vorticity is high, around it the vorticity is zero. As first estimate a threshold of 1 Hz was selected. In the submarine case if the same method is used care must be taken in selecting the threshold value, due to the different sources of vorticity.

The vorticity equation in Lagrangian form is given by [78]

$$\frac{D\omega}{Dt} = (\omega \cdot \nabla)\,\mathbf{u} - \omega\,(\nabla \cdot \mathbf{u}) + \frac{1}{\rho^2}\nabla\rho \times \nabla p + \nu\nabla^2\omega + \nabla\mathbf{f}. \tag{7.6}$$

In this equation the term $(\omega \cdot \nabla)\,\mathbf{u}$ describes the stretching and tilting of vortices due to flow velocity gradients. The term $\omega\,(\nabla \cdot \mathbf{u})$ describes the stretching due to flow compressibility and is zero for incompressible flow. The term $\frac{1}{\rho^2}\nabla\rho \times \nabla p$ is the baroclinic term and includes the vorticity production due to a difference in direction of the pressure and density gradients. It is zero for a simulation where temperature effffects are neglected (so density is only a function of pressure), and is zero for an incompressible flow. The term $\nu\nabla^2\omega$ describes the diffusion of vorticity due to viscous effects and $\nabla\mathbf{f}$ takes the changes due to external body forces into account. This final term is zero for a conservative force field, such as gravity. Under these assumptions the equation can be simplified to [78]

$$\frac{D\omega}{Dt} = (\omega \cdot \nabla)\,\mathbf{u} + \nu\nabla^2\omega. \tag{7.7}$$

In the case of a turbulent jet the $(\omega \cdot \nabla)\,\mathbf{u}$ term, also known as the turbulent term, is assumed to be the dominant term for the vorticity. This assumption is validated in section 7.8.4.

Next to the width the disturbance on the surface is monitored, since this is the main objective of the study.

7.4   Statistical uncertainty

The width at a certain height reaches a steady state after the start-up process. At this steady state the width shows fluctuations around a mean. The statistical uncertainty is a measure for the extend of statistical convergence. Next to that the standard deviation of the signal can be determined. this determines the magnitude of the oscillations. For example: if the exact solution is a sine wave the standard deviation determines the amplitude of the oscillation, whereas the statistical uncertainty is a measure for how well the result approaches a sine wave. Here first a thorough method to determine the statistical uncertainty is described, secondly a pragmatic method to determine the standard deviation is given. In this research only the pragmatic method is used.

7.4.1   Autocovariance method

A method to determine the statistical uncertainty, the autocovariance method, is given by Brouwer et al. [5] and Brouwer et al. [6]. This method is valid if the sample length T satisfies the condition

$$T > \frac{1}{f_L} \tag{7.8}$$

in which f_L is the lowest dominant frequency component. The method makes use of an autocovariance function for a stationary process to estimate the variance of the mean σ_m^2. This variance differs from the sample record variance σ_i^2 due to the finite length of the sample T. Based on the standard deviation of the mean, σ_m, the statistical uncertainty is calculated with

$$U_\% = k_\% \cdot \sigma_m. \tag{7.9}$$

$k_\%$ is a coverage factor based on a normal distribution, which is 1.96 for a 95% confidence interval, and 2.58 for a 99% confidence interval [21]. This coverage factor is applied to ensure that 95% or 99% of the measurement points fall in the range given by the mean $\pm$ the uncertainty. A complete description of the method can be found in appendix E.

7.4.2   Pragmatic method

To give a first estimate of the signal a more pragmatic method is used. The standard deviation of the signal, σ_i, is calculated. As stated before this differs from σ_m,

partly due to the limited sample length. Also the start-up process influences the results. Therefore the mean and standard deviation are calculated based on the last $\frac{3}{4}$ time steps, after the plume has reached a certain height. The method is shown graphically in figure 7.3. The result is shown in figure 7.4, where for the base grid SysVar1 (as described in section 7.6) the width at different heights, the mean and the standard deviation are shown. The plot contains stepwise curves, since the width is determined using a series of measurement points which are 0.01 m apart.
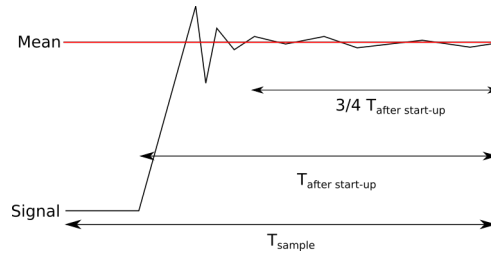
Figure 7.3: Illustration of the pragmatic method to determine the mean and standard deviation of the signal. The mean and standard deviation are based on the data in the range $3/4 \; T_{after \; start-up}$.

Figure 7.4: Spread of the plume in x and y direction on grid SysVar1, with the mean and standard deviation shown. The blue and black line are the width in the x and y-plane, the red line is the mean and the red band indicates the standard deviation.

7.5   Time requirement

Due to the instabilities in the plume at start-up it is necessary to allow the simulation to reach a steady state at which the width oscillates around a mean. Ideally an infinite number of time steps are calculated to achieve this, however this is not feasible. This section aims to determine the required simulation time to achieve a statistically converged solution.

To determine a time requirement a large number of time steps were performed. The spread of the plume in x and y direction at different heights is shown in figure 7.5. In this situation after around 200 time steps the plume reached the surface. Based on this figure it is concluded that it is necessary to let the simulation run at least twice, but preferably three times the time needed for the plume to reach the surface to obtain a steady state solution. After this time also the width at 0.4 m, which is the last to converge, reaches a steady state.
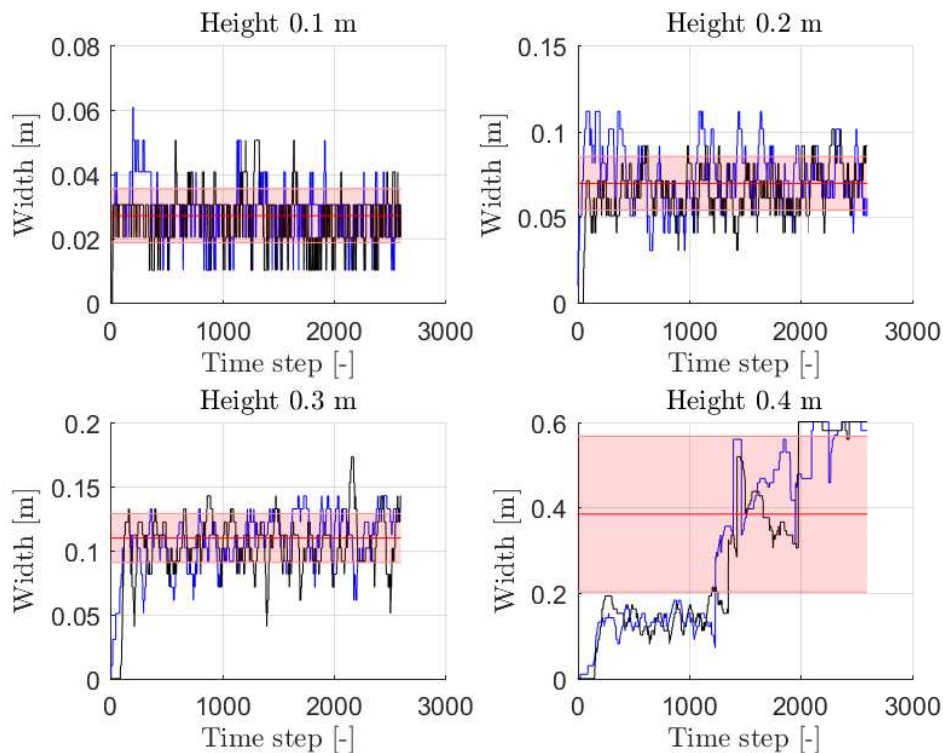
Figure 7.5: Spread of the plume in x and y direction on grid SysVar1, with the mean and standard deviation shown. The blue and black line are the width in the x and y-plane, the red line is the mean and the red band indicates the standard deviation.

It can be seen that around time step 1200 the width of the plume at 0.4 m increases drastically. This effect is caused by the size of the domain and the used

boundary conditions, as described in section 7.2. The domain is limited in size, and the edges are walls. The disturbance on the surface due to the rising plume creates waves who reflect on the walls. Therefore if a large number of time steps are simulated the entire interface starts to move. The width is determined close to the interface, and since this is determined based on vorticity, it appears that the width of the plume has increased. This effect is shown in figure 7.6, where the magnitude of the vorticity on time steps 500 and 1500 is shown. Around the interface, the vorticity has increased between the two different time steps.

It is clear that if a long term simulation is run attention must be paid to the size of the domain and that an outflow or pressure boundary condition is necessary to prevent reflections. Outgoing waves should be damped, for instance by using large cells to add numerical damping.

(a) Time step 500   (b) Time step 1500
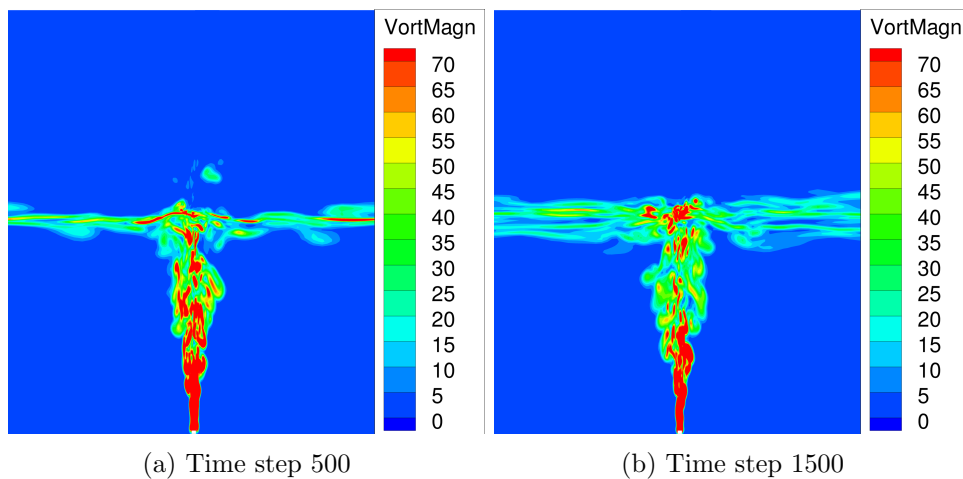
Figure 7.6: Vorticity magnitude at different time steps. The horizontal band of larger vorticity is located around the free surface.

To look into the effect of the boundaries on the simulation a simulation identical to the simulation for grid SysVar1 was run but with an enlarged domain. The radius of the tank was increased from $R = 0.5$ m to $R = 1.5$ m. This leads to larger cells at the boundary which numerically dampens the waves. Also the reflections are postponed since the waves need to travel a longer distances.

The spread of the plume in x and y direction at different heights is again shown in figure 7.7. It can be seen that the sudden increase in width at height $H = 0.4$ m is no longer present. For the other heights and the height at 0.4 m at earlier times steps no difference can be observed.
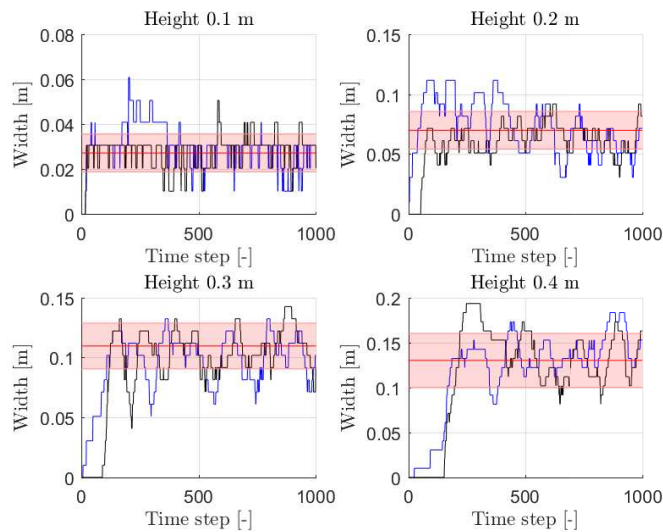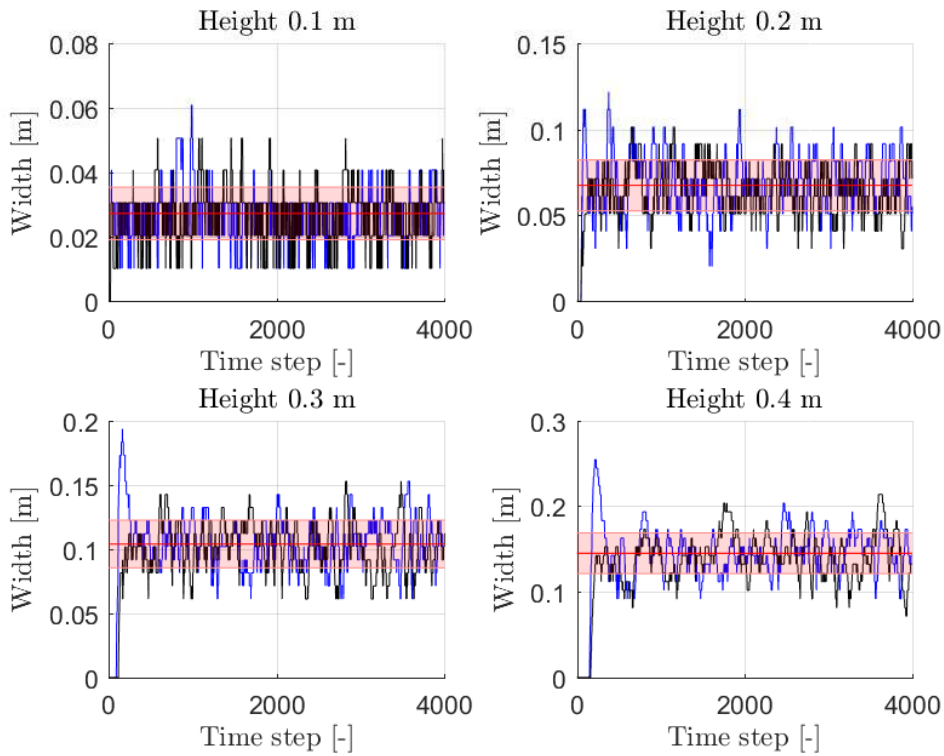
Figure 7.7: Spread of the plume in x and y direction on the enlarged grid SysVar1, with the mean and standard deviation shown. The blue and black line are the width in the x and y-plane, the red line is the mean and the red band indicates the standard deviation.

(a) $R = 0.5$ m   (b) $R = 1.5$ m
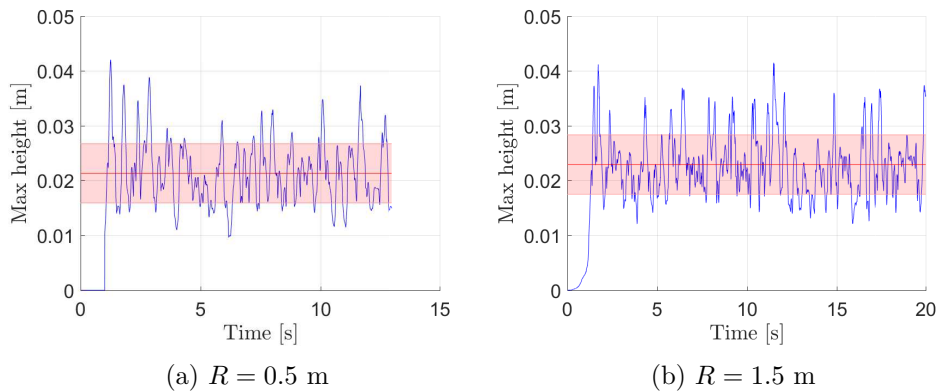
Figure 7.8: The maximum surface elevation over time for the regular and enlarged domain. The red line is the time averaged surface elevation, the red band around the mean is the indicates the standard deviation.

For comparison also the effect on the surface elevation is plotted for both simulations in figure 7.8. It can be seen that there is hardly a difference between mean and the peaks of the surface elevation. Based on this it is concluded that the influence of the boundary conditions on the surface elevation is limited and that the original domain is large enough to use in this study.

7.6 Grid sensitivity

The discretization error is usually one of the largest errors in numerical results, and is assessed by doing a grid sensitivity study. This is described in section 7.7. In this section a first exploration into the influence is performed without the use of a turbulence model. The same plume on three different grids is shown in figure 7.9. Here also the time step sizes were changed to the Courant number and achieve convergence. This comparison is made using a symmetry plane and half the domain, therefore the spread in the image is overestimated. Three grids is low to estimate the sensitivity, however it does give an impression of the influence of the mesh.
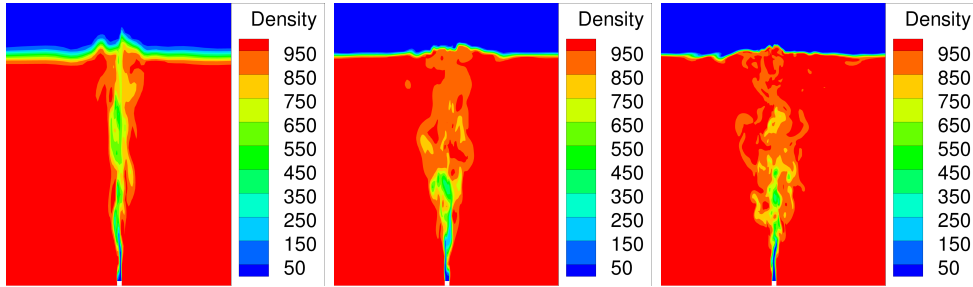
Figure 7.9: The exhaust plume on a coarse, a medium and a fine grid. An instantaneous cross section of the density is shown.

A relatively dense grid is needed to accurately model the start-up of the plume. On the coarse grid the plume goes in a straight line to the surface, and the water is thrown up to an unrealistic height. On finer grids vortices arise which slow down the plume and increase the spread of the plume. This increase in spread persists even after start-up. Since no turbulence model is used here, the vortices can only arise if the cell size and time step are small enough. The length scale of the vortices must be larger than a number of cells to be captured on the grid. Also the Reynolds number must be low and the equations must be solved well (so the L_{inf} norm is below 10^{-6}).

On a coarse grid these vortices can not be captured. Although the spread is smaller on a coarse grid the shape of the plume is comparable. The denser grids capture shedded pockets of air which are not visible on the coarse grid. Also on the denser grids the free surface interface is more compressed, which leads to a better indication of where the interface is located. The height of the water pile after stabilization of the turbulent jet is approximately equal.

Based on these exploratory results a more systematic grid study was set up. A base grid (SysVar1) was developed, this grid is shown in figure 7.10. The grid has a constant cross section in the horizontal plane, the cell size differs in the vertical direction. The horizontal plane consists out of a cylinder above the nozzle and an O-grid surrounding this cylinder. Smaller grid cells are used in the region where the jet is located, surrounding this region the cell size increases. A refinement band is present at the initial water level. The number of grid cells in different directions can be found in table 7.3. Using these dimensions three dimensionless grid lengths are obtained, x^+, y^+ and z^+. Here x, y and z denote the streamwise, radial and circumferential directions. The values of x^+, y^+ and z^+ in the region above the nozzle are in the order of 500, 70 and 0 respectively. To determine these values the friction velocity is taken as 4% of the velocity of the plume. The cell Péclet number has a magnitude in the order of 10^2, so convection dominates over diffusion. The Courant number in the domain is discussed in section 7.7.2.

(a) Total domain.

(b) Top view of the domain.

(c) Detail of the nozzle.
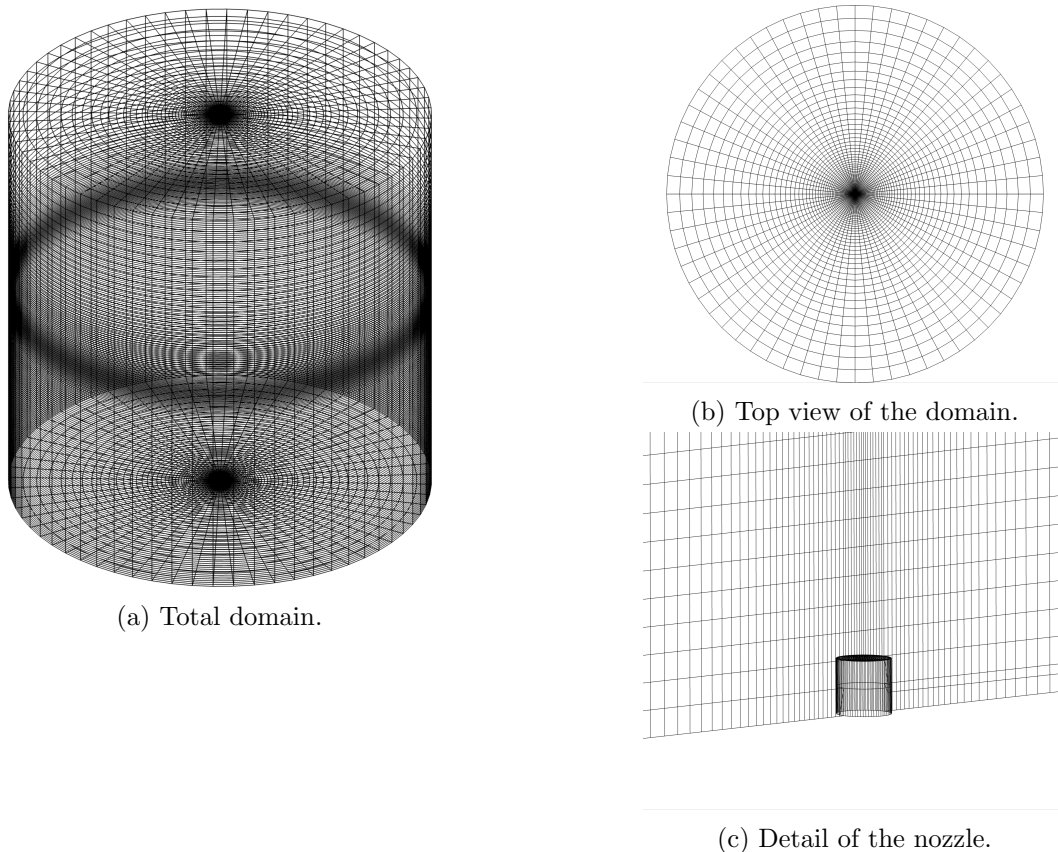
Figure 7.10: The grid SysVar 1. The nozzle is located at the bottom in the center of the domain.

Table 7.3: Dimensions and number of grid cells of grid SysVar1.

	Location	# of cells [-]	Distance [m]
Horizontal	Nozzle radius	8	0.005
	Nozzle to edge	59	0.5
Vertical	Nozzle to lower end of refinement band	79	0.45
	Refinement band over water surface	50	0.1
	Top end of refinement band to top of domain	30	0.45

This grid is refined with a refinement factor of 1.5 in the horizontal plane, so in the x and y direction after which grid SysVar1.5X is obtained. Also the base grid is refined with the same factor in the vertical direction which results in grid SysVar1.5Z. Finally a grid refined in all three directions (SysVar1.5) is made. To estimate the numerical uncertainty also a grid with a refinement factor of 0.8 in all directions (SysVar0.8) and a factor of 1.2 (SysVar1.2) are made. An overview of the grids with their properties and the relation between the grids is given in figure 7.11. In this figure the relationship between the different grids is shown. The four grids on the diagonal are geometrically similar, and can therefore be used to estimate the numerical uncertainty as described in section 7.7. The four grids which form a square are used to look into the sensitivity of refinement into different directions.
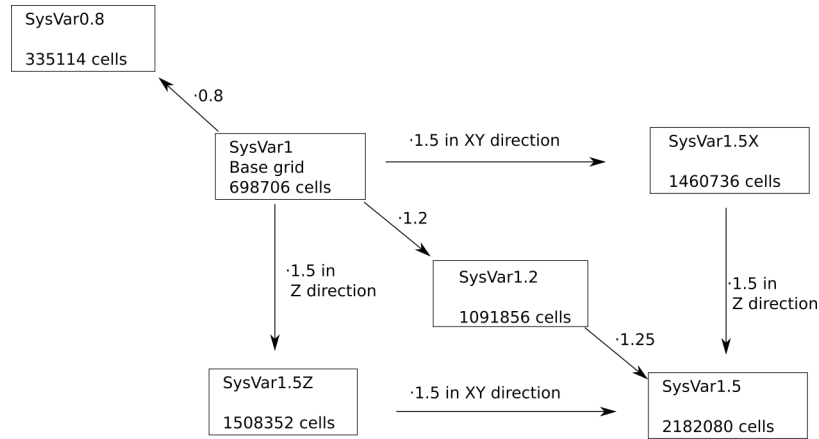
Figure 7.11: The different grids with their number of grids cells and their dependencies. The four grids on the diagonal are geometrically similar.

The spread of the height for the different grids is shown in figure 7.12. Also the theoretic prediction as formulated by equation 7.1 in section 7.1 is shown.

It can be seen that the grid refinement in the horizontal plane has little influence

on the spread. The grid sizing as defined for grid SysVar1 suffices. The spread is however increased by decreasing the grid size in vertical direction. Grids SysVar1 and SysVar1.5X have a comparable slope as the theoretical prediction, but they under predict the spread. Grids SysVar1.5Z and SysVar1.5 also under predict the spread at lower heights, but with increasing height the spread increases more than in theoretical formulation.

For comparison of different settings in the sensitivity study the base grid, Sys-Var1, is used. This choice is mainly influenced by the lower computational effort due to the lower number of grid cells in this grid.
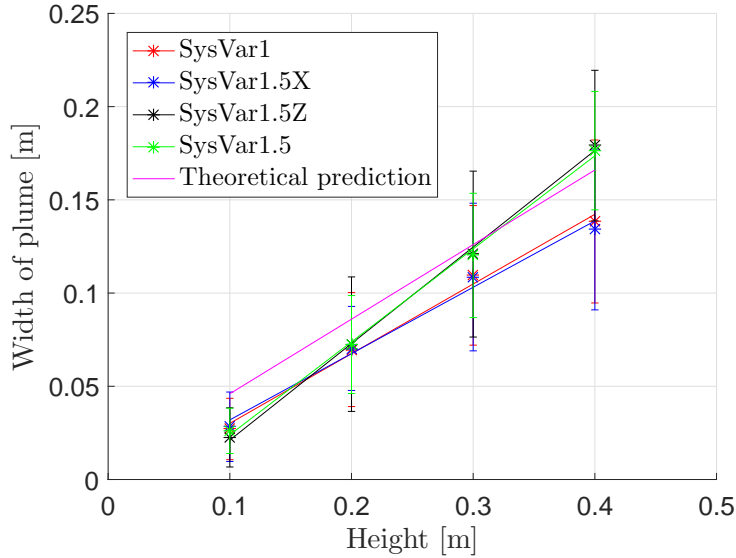
Figure 7.12: Average spread of the plume over the height, for the different grids. The errorbars indicate the standard deviation.

7.7   Numerical uncertainty

As described in section 5.9 the numerical error consists of three elements: the round-off error, the iterative error and the discretization error. In this section the iterative and discretization error are estimated.

7.7.1   Iterative error

The convergence behavior of a representative simulation is shown in figure 7.13, here a number of time steps are shown. It can be seen that most time steps converge, occasionally some time steps oscillate (time step 60 in figure 7.13) after which the convergence is resumed. This oscillation is usually when a large pocket of air rises from the nozzle. The L_∞ norm for all residuals is usually around or below 10^{-6}, except for the above described stagnation steps and for the air volume fraction

equation. The iterative error estimate for the different quantities for a representative time step is given in table 7.4. These results are obtained using a $k - \sqrt{k}L$ turbulence model, the order of magnitude of convergence is representative for other calculations. It is assumed that this convergence behavior, even though some time steps oscillate, is acceptable such that the iterative error is negligible compared to the discretization error.
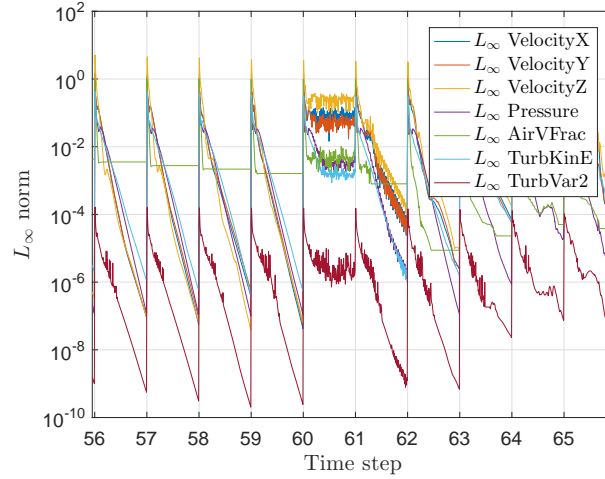
Figure 7.13: Convergence behavior using a $k - \sqrt{k}L$ turbulence model. A number of representative time steps are shown.

Table 7.4: Iterative error estimate of a representative time step. The results are obtained from a simulation using a $k - \sqrt{kl}$ turbulence model, the order of magnitude is representative for other simulations.

Item	$\Delta\phi_i$	δ
L_2 VelocityX	$3.74 \cdot 10^{-10}$	$5.09 \cdot 10^{-9}$
L_2 VelocityY	$4.24 \cdot 10^{-10}$	$5.78 \cdot 10^{-9}$
L_2 VelocityZ	$6.37 \cdot 10^{-10}$	$2.17 \cdot 10^{-8}$
L_2 Pressure	$1.59 \cdot 10^{-8}$	$1.06 \cdot 10^{-6}$
L_2 AirVFrac	$6.85 \cdot 10^{-6}$	$5.51 \cdot 10^{-4}$
L_2 TurbKinE	$6.10 \cdot 10^{-9}$	$1.56 \cdot 10^{-7}$
L_2 TurbVar2	$2.89 \cdot 10^{-12}$	$6.73 \cdot 10^{-11}$
L_∞ VelocityX	$5.64 \cdot 10^{-8}$	$1.05 \cdot 10^{-6}$
L_∞ VelocityY	$8.78 \cdot 10^{-8}$	$1.82 \cdot 10^{-6}$
L_∞ VelocityZ	$6.53 \cdot 10^{-8}$	$2.93 \cdot 10^{-6}$
L_∞ Pressure	$1.12 \cdot 10^{-7}$	$5.09 \cdot 10^{-6}$
L_∞ AirVFrac	$2.85 \cdot 10^{-3}$	$7.69 \cdot 10^{-3}$
L_∞ TurbKinE	$5.57 \cdot 10^{-7}$	$1.66 \cdot 10^{-5}$
L_∞ TurbVar2	$3.07 \cdot 10^{-10}$	$9.47 \cdot 10^{-9}$

7.7.2   Discretization error

The discretization error is estimated for the width at the four different heights (0.1, 0.2, 0.3 and 0.4 m) and the mean of the maximum height of the elevation at the surface, as described in section 7.3. The used grids and time steps used for this analysis are shown in table 7.5. Also the maximum Courant numbers are shown, these are rather high (larger than one). However, two remarks must be made here. Firstly it is an implicit solver so a Courant number higher than 1 is possible. Secondly this high value only occurs in a small region above the nozzle, for the region surrounding this the Courant number is much lower (below 2). This is shown in figure 7.14 where the Courant number in the domain is plotted.
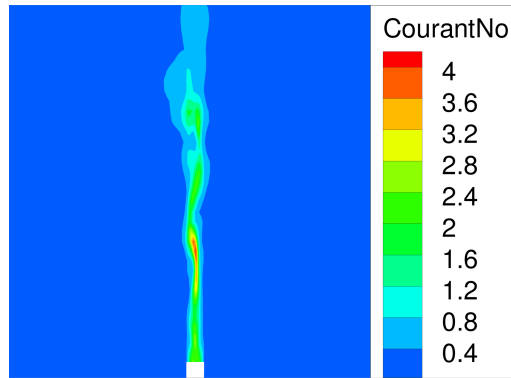
Figure 7.14: Courant number in the domain for a simulation with a $k - \sqrt{k}L$ turbulence model, with a time step of 0.001 s.

Table 7.5: Grids and time step combinations used for the uncertainty analysis. The values in the table are the averaged peak values of the Courant numbers in the region above the nozzle.

Grid	Number of grid cells [-]	Time step [s]			
		0.001	0.003	0.005	0.01
SysVar0.8	$3.34 \cdot 10^5$	2.5	10	15	25
SysVar1.0	$6.53 \cdot 10^5$	3	12	17	
SysVar1.2	$1.13 \cdot 10^6$	3.2	15		
SysVar1.5	$2.20 \cdot 10^6$	4			

The obtained fit for the mean of the maximum elevation of the surface is shown in figure 7.15. The obtained fits for the width at different heights are shown in figure 7.16. Finally the results of the analysis are shown in table 7.6.

It can be seen in table 7.6 that there is a difference between the different uncertainties. For the surface elevation and the spread at height 0.3 and 0.4 m the uncertainty is reasonably small (in the order of 12%). The result for the surface
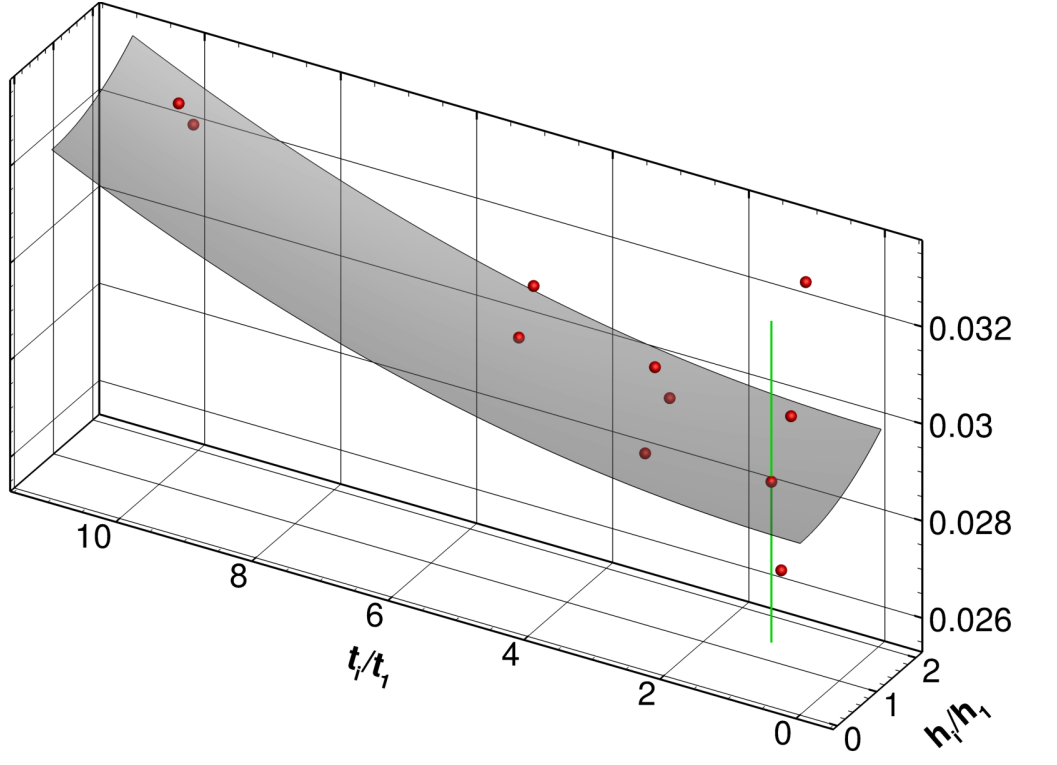
Figure 7.15: Error estimate for the mean of the maximum elevation of the water surface. The red dots are the data points, the green vertical line indicates the uncertainty and the grey plane is the fit, $U_\phi = 11.4\%$.

Table 7.6: Uncertainty estimates for the finest grid and time step in percentage based on Eça and Hoekstra [16] and Rosetti et al. [70]. Next to the result the type of fit is shown, p is the fit type for the grid dependency and q is the fit type for the time step dependency.

Item	ϕ_0	ϕ_1	U_ϕ	p	q
Spread at $H = 0.1$ m	$2.92 \cdot 10^{-2}$	$3.09 \cdot 10^{-2}$	37.2%	1.00	* 1,2
Spread at $H = 0.2$ m	$4.57 \cdot 10^{-2}$	$5.88 \cdot 10^{-2}$	27.8%	* 1,2	1.00
Spread at $H = 0.3$ m	$9.30 \cdot 10^{-2}$	$9.70 \cdot 10^{-2}$	13.1%	* 1,2	2.00
Spread at $H = 0.4$ m	$1.18 \cdot 10^{-1}$	$1.14 \cdot 10^{-1}$	11.9%	2.00	2.00
Surface elevation	$2.88 \cdot 10^{-2}$	$2.90 \cdot 10^{-2}$	11.4%	2.00	2.00

* 1,2 Fit was made using first and second order exponents

(a) $H = 0.1$ m, $U_\phi = 37.2\%$

(b) $H = 0.2$ m, $U_\phi = 27.8\%$

(c) $H = 0.3$ m, $U_\phi = 13.1\%$

(d) $H = 0.4$ m, $U_\phi = 11.9\%$
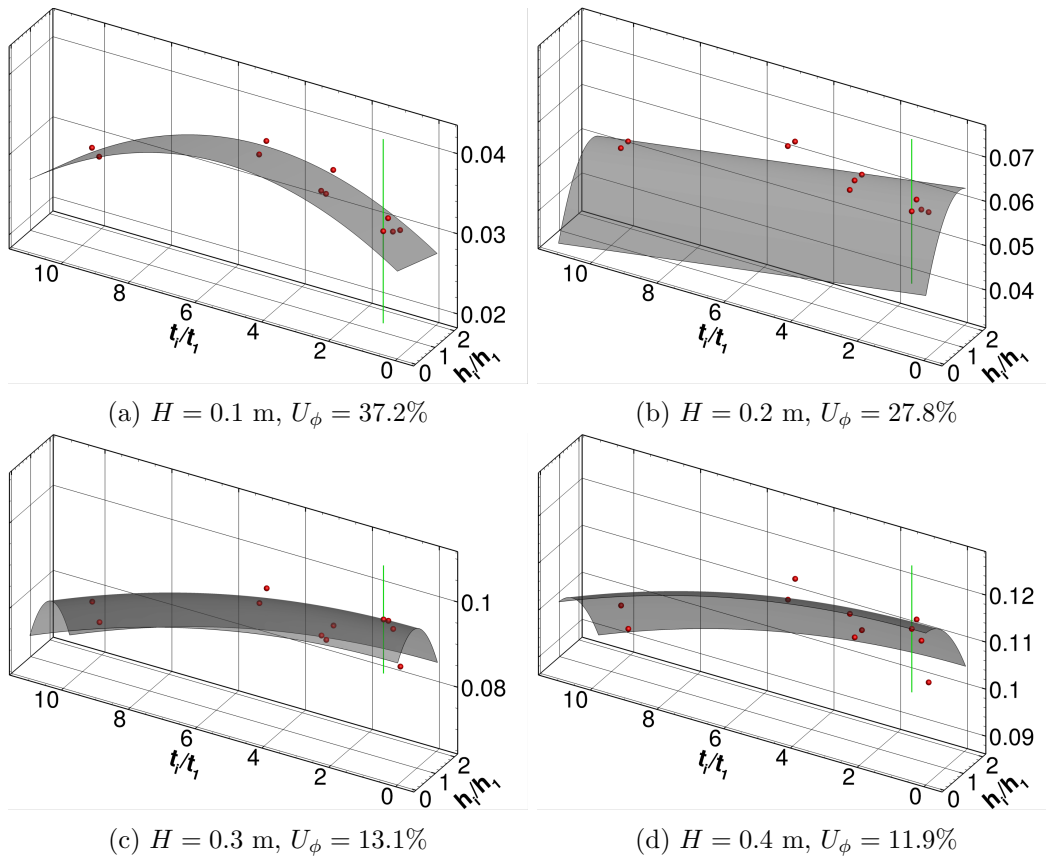
Figure 7.16: Error estimate for the width of the plume at different heights. The red dots are the data points, the green vertical line indicates the uncertainty band for the finest grid and time step and the grey plane is the fit.

elevation is one of the main interests since this is the final goal of this research. The uncertainty is in the order of 10%, though the spread in data points is large as can be seen in figure 7.15.

The larger uncertainty at lower heights is attributed to the fact that the difference between the values in general is small. Consequently if there is one larger deviation the error in percentage is large, therefore the uncertainty at this point is large. The obtained fit for these data points is a first and first-and-second order fit which leads to a higher uncertainty. This larger uncertainty might also be attributed to the large Courant numbers, since these occur at the lower heights. Consequently the iterative error in this region is larger.

The large uncertainty in general can be attributed to the fact that the process is highly unstationary. The uncertainty estimate is based on a mean of the value. At times there is a difference between the spread in the x-direction versus in the y-direction. Consequently the statistical uncertainty also attributes to the estimated discretization uncertainty. This effect can be decreased to some extend by using an increased amount of time steps, this does lead to a high computational cost and was therefore not done for this estimate.

It is assumed that the value of the uncertainty (in the order 12-20%) is representative for all numerical results described in this work. To this end the conditions for the grid as described in section 7.6 must be satisfied. Next to this verification, validation of the results is necessary. This is elaborated in section 7.9.

7.8 Sensitivity study of input parameters

For the turbulent jet the sensitivity to a number of parameters is determined. First of all two parameters which are a consequence of the operational profile of the submarine are looked into, namely the density and the volume flow of the exhaust gases. Next the the influence of the viscosity is studied, and finally the effect of the used turbulence model. The effect of the parameters is compared based on images, the width of the plume and the disturbance on the surface.

7.8.1 Influence of gas density

The temperature of the exhaust gases influences the density of the gases. This density difference might influence the results.

If the exhaust gas is modeled as an ideal gas, the ideal gas law can be applied

$$\rho R T = M p \tag{7.10}$$

in which R is the gas constant, M the molecular mass of the gas, p the pressure and T the temperature in Kelvin. The molecular mass depends on the constitution of the gas. Exhaust gas differs from air in constitution, however the consequent increase in molecular weight is low, in the order of 5% depending on the fuel and

the engine. Since the exhaust is located several meters m below the water surface the hydrostatic pressure must be taken into account. At the exhaust this pressure is around 134 kPa. The exhaust gases have an approximate temperature of 50-60°C. These two parameters have a different effect, the increase in temperature leads to a decrease in the density, the increase in pressure to an increase in density.

ReFRESCO is an incompressible solver, so the density specified for the different phases (water, air and exhaust gas) is constant. This may lead to a problem since due to the difference in temperature and pressure over the turbulent jet the density of the exhaust gases is not constant.

The density of the exhaust gas for atmospheric conditions and a temperature of 20°C is 1.2 kg/m^3. If only the hydrostatic pressure is taken into account the density rises to around 1.6 kg/m^3, if however also a temperature of 60°C is used the density has a value of 1.4 kg/m^3.

The influence of this variation is investigated, the different densities looked into are 1.2, 1.4 and 1.6 kg/m^3. A comparison of the solutions for the three different air densities can be found in figure 7.17.
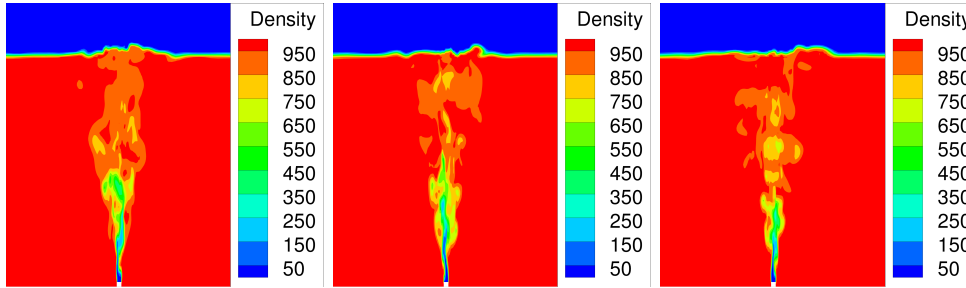
Figure 7.17: The exhaust plume with a density 1.2, 1.4 and 1.6 kg/m^3. The instantaneous cross section of the density is shown.

The difference in the density leads to a difference in rising velocity of the plume. The time in which the plume reaches the surface is inversely dependent on the density, the values can be found in table 7.7. This effect can be explained due to the fact that the inflow velocity and area are constant, consequently with a larger density there is a larger mass flow. Since the pressure at location of the nozzle is constant a larger mass flow leads to larger bubbles, which rise faster.

Table 7.7: Density influence on the rising time for the intermediate grid.

Density gas [kg/m^3]	Rising time [s]
1.2	0.83
1.4	0.78
1.6	0.58

The difference in density influences the start-up of the system, but has little influence on the plume when it stabilizes. The shape and spread of the plume are approximately equal, as can be seen in figure 7.17. This instantaneous density plot is representative for the plume throughout the simulation. Also the elevation of the water surface is hardly effected by the difference in density.

This lack of apparent influence can be explained due to the small variations in density. The ratio between the density of the gas and the liquid is in the order of 10^3, the variation in gas density investigated lies in the order 10^{-1}. Larger variations in density will likely influence the solution, however these densities will not occur for a submarine exhaust. It can be concluded that the influence of density, and therewith the temperature of the exhaust gas is negligible.

7.8.2   Influence of velocity profile

In section 5.9.2 it was noted that although the convergence in general is satisfactory, for some time steps it is not. A hypothesis for this behavior is the used velocity profile on the nozzle which is an uniform (top hat) profile. This discontinuity in velocity might lead to the oscillations, also it is less accurate since in reality a velocity profile in the pipe develops (a Poiseuille flow). To investigate this hypothesis two simulations with a parabolic velocity profile were performed.

The original velocity profile is shown in figure 7.18a. In figure 7.18b a parabolic profile is shown where the total gas flux is equal to the one for the uniform profile. The convergence for this simulation is similar to the convergence for the uniform velocity profile, due to the increased velocity in the core of jet which leads to a locally increased Courant number. This is confirmed by the result for the velocity profile shown in figure 7.18c, where again a parabolic profile is prescribed but with a core velocity equal to the uniform inflow velocity. Using this velocity profile the number of steps who stagnate is reduced.

Next to the improved convergence behavior it is noted that the resulting plume and disturbance on the surface are not affected by the change in velocity profile in the nozzle, which is in agreement with the statement in section 7.1 that the momentum in the plume is dominated by buoyancy rather than by the initial momentum.

(a) Uniform inflow   (b) Parabolic inflow A   (c) Parabolic inflow B
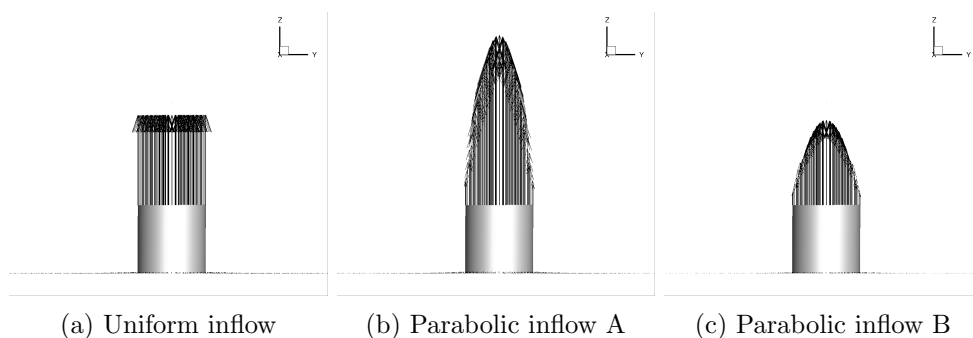
Figure 7.18: The used velocity profiles, the vectors indicate the inflow velocity.

7.8.3   Influence of volume flow gas

To see the effect of a variation in volume flow of exhaust three different exhaust flows are used:

- $V_{gas} = 1$ m/s, or $\phi_V = 7.85 \cdot 10^{-5}$ m³/s,

- $V_{gas} = 2$ m/s, or $\phi_V = 1.57 \cdot 10^{-4}$ m³/s,

- $V_{gas} = 3$ m/s, or $\phi_V = 2.36 \cdot 10^{-4}$ m³/s.

A comparison of the solutions for the three different volume flows can be found in figure 7.19.
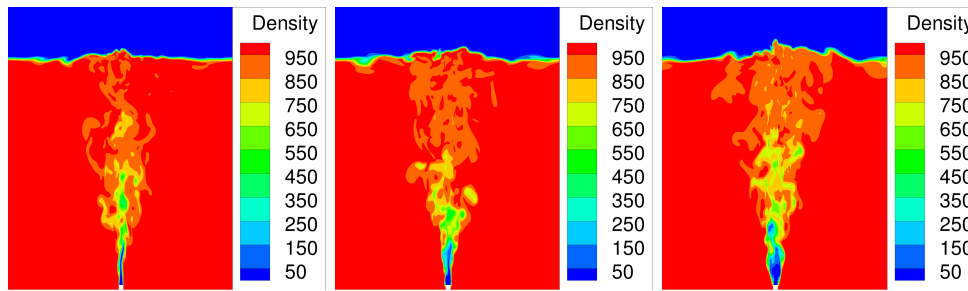
Figure 7.19: The exhaust plume with a volume flow of 1, 2 and 3 m/s. The instantaneous cross section of the density is shown.

Based on the results it can be concluded that the shape of the plume remains equal, also the spread lies in the same order. As expected the air volume fraction along the plume is larger. Also due to the increase in amount of gas the disturbance on the surface is increased in height, on average 2, 2.5 and 5 cm respectively. This is as expected since the increase in exhaust gas both increases the momentum which is added at the bottom, as well as reduces the density of the mixture which leads to an increase rising velocity.

7.8.4   Simulation without viscosity

As shown in the previous sections the plume spreads in the water as expected. This spread is partly due to the vortices which occur next to the jet, and partly due to numerical effects such as diffusion due to the discretization scheme. To investigate the numerical diffusion a simulation in an inviscid flow was performed. The viscosity both for water and for air was set to 0 kg m^{-1}s^{-1}. Also in section 7.3 the hypothesis was made that the $(\omega \cdot \nabla)\,\mathbf{u}$ term in the vorticity equation is dominant, this hypothesis is investigated in this section.

It is important to note that this simulation is a more exploratory investigation into the effects of an absence of viscosity, therefore care must be taken in using these results. The Courant number in the domain is on the high side, up till 10 above

the nozzle in the core of the plume and also the convergence is not ideal. The L_∞ norm for the residuals has a order of magnitude of around 10^{-1}. In the simulation a QUICK scheme is used as advection scheme for the momentum equation, and a Fromm scheme for the air volume fraction.

Due to the lack of viscosity and the absence of a turbulence model it was expected that the plume would travel vertically and no vortices would occur. However contrary to the expectations also in this case an instability occurs which leads to a spread of the plume. The development of the jet near the nozzle can be seen in figure 7.20.

(a) $T = 0.1$ s (b) $T = 0.2$ s (c) $T = 0.3$ s (d) $T = 0.4$ s
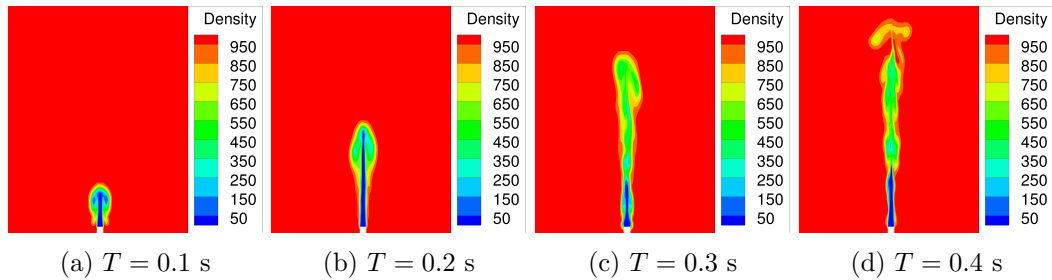
Figure 7.20: Development of the jet near the nozzle without viscosity.

Also the spread is almost identical to a simulation with viscosity with the same numerical settings. The start-up process does take more time.

This spread can be explained when one looks into the velocity. As a consequence of the inflow of gas near the nozzle the fluid moves upward in the center of the tank. Gravity combined with conservation of mass leads to a downwards velocity surrounding the upwards jet, which in turn leads to a inflow of water from the walls towards the center near the bottom of the tank. This flow pattern forms a circulation around the jet, and therefore an instability surrounding the jet can be observed. Secondly there is a pressure effect, under influence of the higher pressure in the core of the plume and the lower pressure surrounding the plume, the plume spreads out.

In section 7.3 it was described that the vorticity equation could be simplified to equation 7.7. In this case, with the absence of viscosity the $\nu\nabla^2\omega$ term is also zero, so the equation simplifies to

$$\frac{D\omega}{Dt} = (\omega \cdot \nabla)\, \mathbf{u}. \tag{7.11}$$

In figure 7.21a the vorticity magnitude is plotted for this simulation. When compared with figure 7.21b it can be seen that the vorticity magnitude has the same order of magnitude. Based on this it can be concluded that the $(\omega \cdot \nabla)\, \mathbf{u}$ term, the production due to flow velocity gradients, is the dominant term.

It can be concluded that even in an inviscid flow the plume spreads under the influence of the flow pattern, the pressure and numerical effects. The increased time

(a) Without viscosity   (b) With viscosity
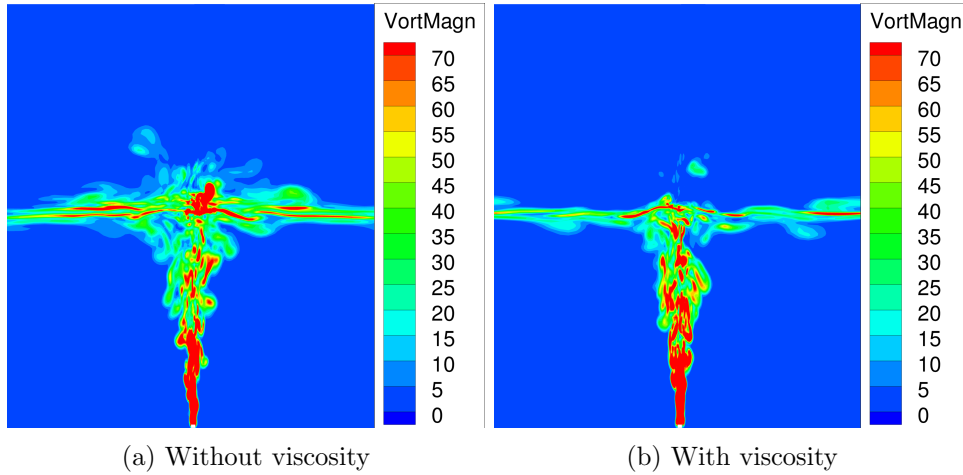
Figure 7.21: Vorticity magnitude with and without viscosity. The horizontal band of larger vorticity is located around the free surface.

needed for the spread can be attributed to the absence of shear. Shear entraps more fluid in the vortices, which leads to an increased spread. This in turn leads to a decrease in time needed for the start-up process. Even so in the end the magnitude of vorticity remains the same since the viscous term in the vorticity equation is small compared to the turbulent term.

7.8.5 Turbulence models

All calculations in sections 7.8.1, 7.8.3 and 7.8.4 were done without a turbulence model. The calculations were in effect an implicit LES modeling without a subgrid model. To be able to accurately predict the flow (including the boundary layer) around a rigid body, like a sail, and to reduce the dependency on the grid and numerical settings the inclusion of a turbulence model is needed. Different turbulence models are available in ReFRESCO. Based on literature a selection is made, the used models can be divided into one-equation models, such as the Spalart-Allmaras model and the one equation model of Menter; two equation models, such as the $k-\omega$ Menter SST 2003 model and the $k-\sqrt{k}L$ model, and an EARSM. The one-equation models are not the most obvious choice for a turbulent jet, but can be used to look into the influence of a more simple turbulence model. Due to the absence of a wall in the modeled case the $k-\omega$ model is in effect a $k-\epsilon$ model in the far field.

The calculations described in this section are all done using the grid SysVar1. The resulting elevation of the water surface is described in section 7.8.6.

Effect of inclusion of a turbulence model

As start more conventional turbulence models, such as the Spalart-Allmaras, Menter one equation and SST 2003 turbulence models are used. The inclusion of a turbu-

lence model influences the result strongly. Rather than a spread plume the air forms a pipe which travels vertically to the surface. This can be seen in figure 7.22a where both the density and vorticity magnitude are plotted for the SST 2003 model. There is a clear decrease in width when based on the density, however when looked into the vorticity magnitude the spread of the plume is approximately equal. Also the spread is more stable.

(a) Density   (b) Vorticity magnitude
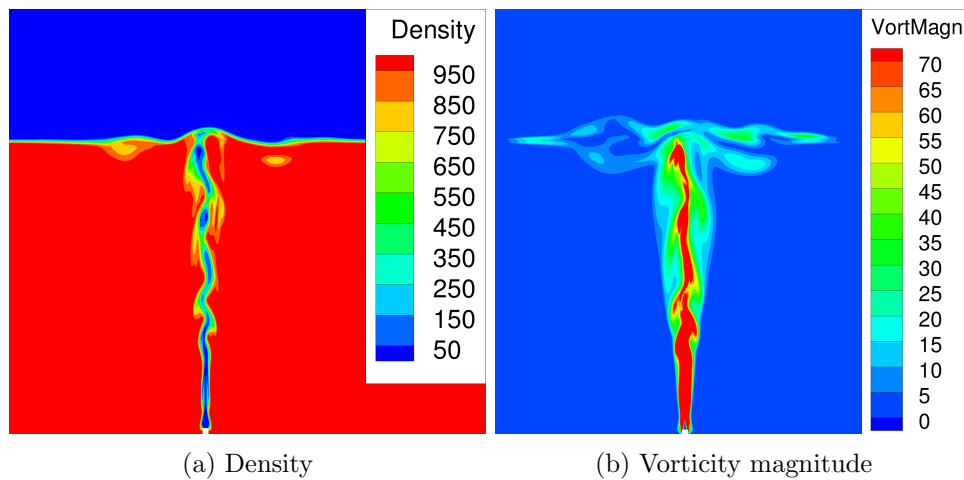
Figure 7.22: Density and vorticity for the SST 2003 turbulence model.

The spread based on the vorticity is plotted for the three used turbulence models and compared with the spread without turbulence model. This plot can be found in figure 7.23. It can be seen that the trend is similar for all three turbulence models, the spread of the Spalart-Allmaras is closest to the situation without a turbulence model, the Menter one equation and the SST 2003 model give a similar but lower spread.

As described there is a clear difference between width based on density and based on vorticity. In figure 7.24 an isosurface of the air volume fraction at a representative time step is shown for the three different turbulence models and the case without turbulence model. Here it can be seen that the interface is smoothed due to the influence of by a turbulence model. Secondly there are no longer any shedded parts with a higher air volume fraction. This difference in the interface leads to the described differences in spread.
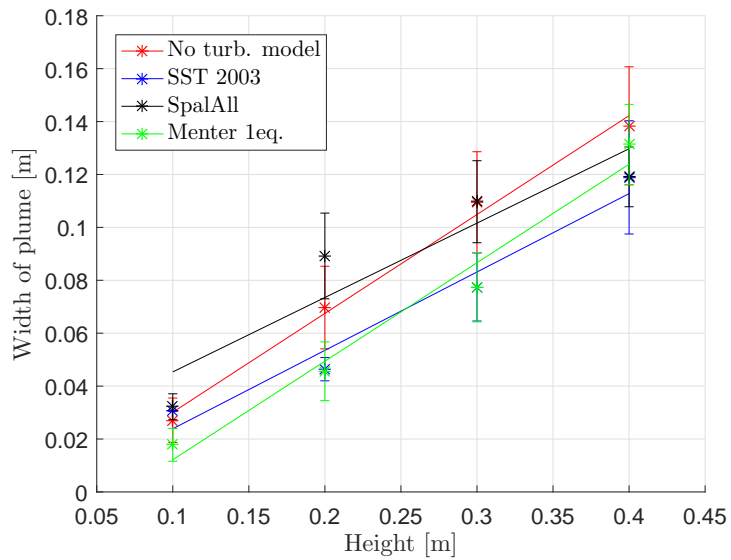
Figure 7.23: Width based on vorticity over the height of the plume for three different turbulence models. The errorbars indicate the standard deviation.

(a) No turbulence model

(b) SST 2003.

(c) Spalart-Allmaras.

(d) Menter one equation.
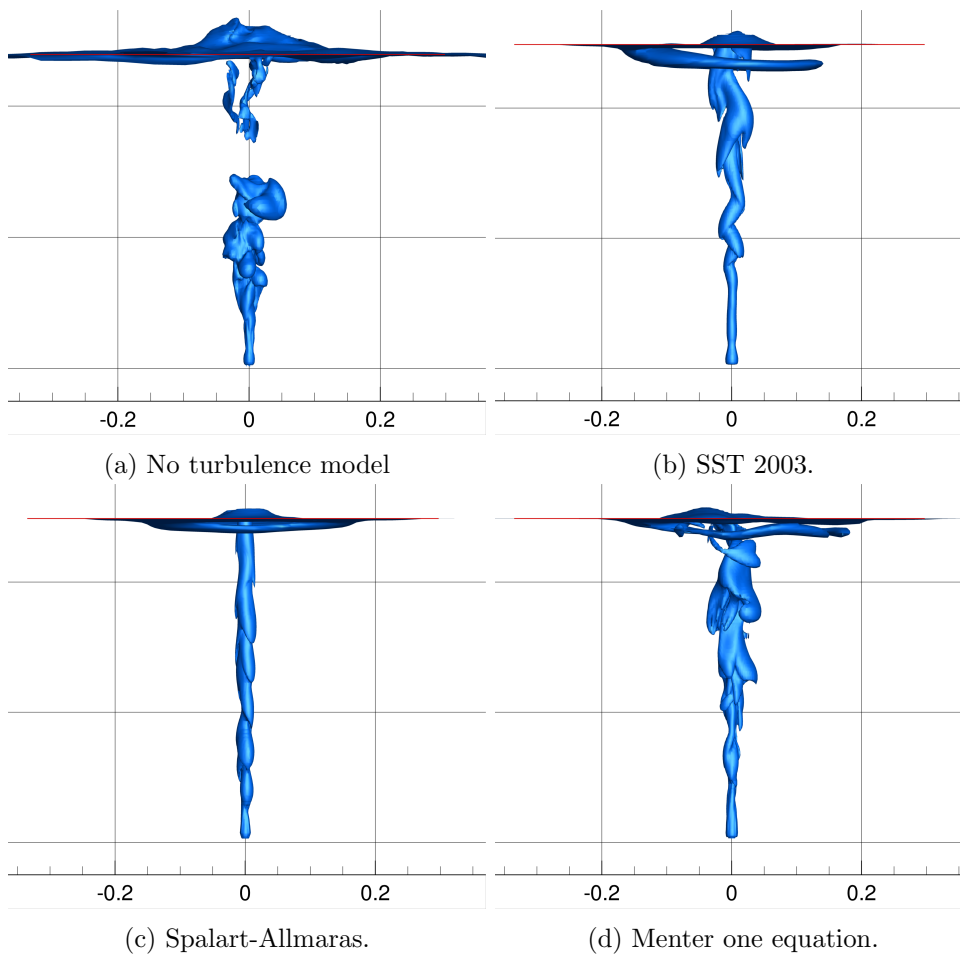
Figure 7.24: Isosurface of the air volume fraction at $AVF = 0.1$ for the conventional turbulence models. The horizontal red line indicates the free surface

The increased stability and decreased spread might be attributed to the high eddy-viscosity developed at the air-water interface due to the turbulence model. The eddy-viscosity ratio

$$\frac{\nu_t}{\nu} \tag{7.12}$$

is calculated and plotted in figure 7.25. It can be seen that this ratio reaches high values at the locations where there is a mixture of air and water. The eddy-viscosity near an interface is too high, which leads to a very stable interface. To reduce this effect an eddy-viscosity correction, such as proposed by Reboud et al. [63] might be necessary. This correction is described in the following section.
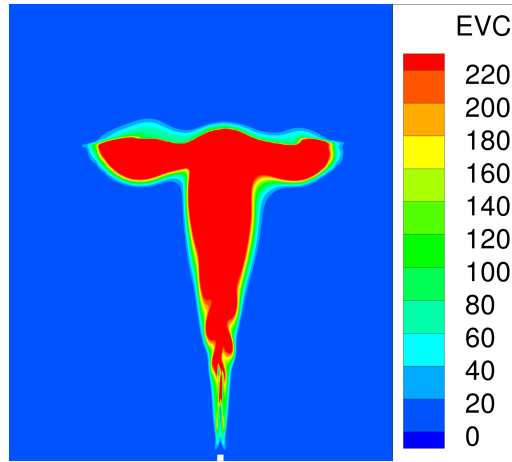
Figure 7.25: Eddy-viscosity ratio $\frac{\nu_t}{\nu}$ using the SST 2003 turbulence model.

Eddy-viscosity correction

Reboud et al. [63] suggested an improved $k - \epsilon$ model with an eddy-viscosity correction to remedy similar issues with modeling cavitation. This correction is known as the Reboud correction. Due to the high eddy-viscosity no re-entrant jet could be modeled. The correction is described in detail by Fortes-Patella et al. [18].

The correction affects the mixture turbulent viscosity, which is calculated as

$$\mu_t = f(\rho)\frac{C_\mu k^2}{\epsilon}. \tag{7.13}$$

Here $f(\rho)$ is the proposed correction factor, defined as

$$f(\rho) = \rho_g + \left(\frac{\rho_g - \rho}{\rho_g - \rho_l}\right)^n (\rho_l - \rho_g). \tag{7.14}$$

The only variable in the equation is the density ρ, which is dependent on the air volume fraction in a cell. The eddy-viscosity correction is determined by the factor n. A value of $n = 1$ yields no correction, and makes the turbulent viscosity linearly

dependent on the density. The correction factor is plotted for a number of correction factors across a range of densities and shown in figure 7.26. It can be seen that for pure air and pure water the viscosity is not affected, only in the cells where a mixture is present the correction factor is used. A value of $n = 10$ is often employed for cavitation modeling.
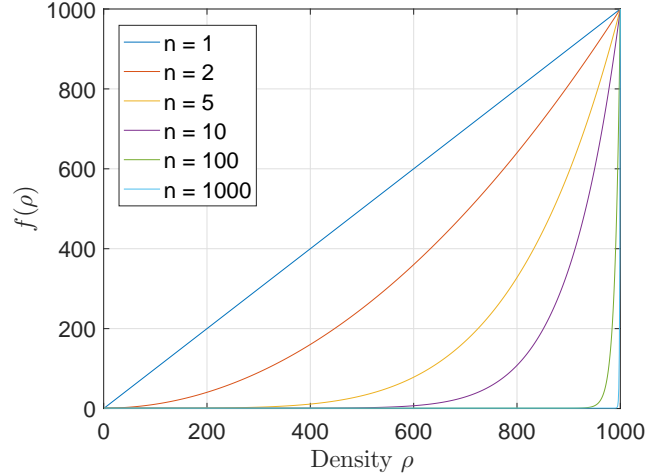
Figure 7.26: Eddy-viscosity correction factor $f(\rho)$ as function of the density, as proposed by Fortes-Patella et al. [18].

Effect of inclusion of the eddy-viscosity correction

The eddy-viscosity correction is applied on both the SST 2003 and the Menter one equation model. For the SST 2003 model both a correction factor of $n = 5$ and $n = 10$ are used, for the Menter one equation only a factor of $n = 5$ was used. The effects described here concern the SST 2003 model, the effects on the Menter one equation model are similar.

The effect of the correction is clearly visible when again the density and vorticity magnitude are plotted, as shown in figure 7.27. When looking at the density plots it can be observed that with correction now the air spreads out in the water. Also the plume is more unstable, as can be seen by the vorticity magnitude plot. The result with $n = 5$ and $n = 10$ cannot clearly be distinguished.

The eddy-viscosity ratio $\frac{\nu_t}{\nu}$ is shown again in figure 7.28. Here the difference between the two correction factors is more obvious. For both the ratio is considerably lower, especially near the nozzle. For $n = 5$ at the free surface in the middle of the plume the ratio is still quite large, for $n = 10$ this area with a large ratio has disappeared. To investigate the effect of the correction the correction factor normalized with the density $\frac{f((\rho)}{\rho}$ is plotted in figure 7.29. A value of 1 means no correction. It can be seen that around the nozzle and the free surface the most correction occurs, whereas in the jet below the free surface less correction occurs. This is attributed to the lower air volume fraction and therefore higher density in

(a) Density, no correction   (b) Vorticity magnitude, no correction

(c) Density, $n = 5$ (d) Vorticity magnitude, $n = 5$

(e) Density, $n = 10$ (f) Vorticity magnitude, $n = 10$
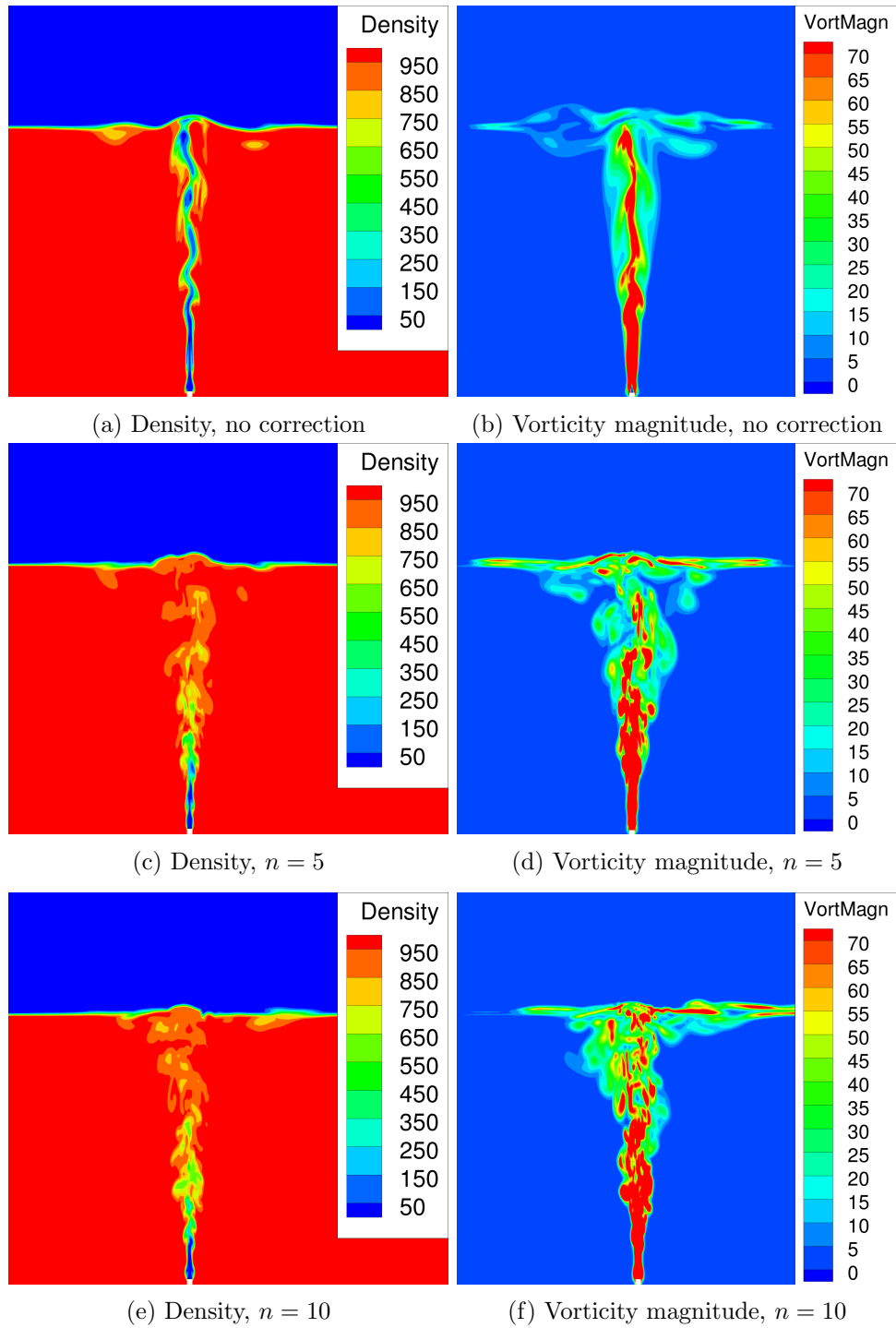
Figure 7.27: Density and vorticity magnitude, SST 2003 turbulence model with eddy-viscosity correction using $n = 5$ and $n = 10$.

this region.

(a) $n = 5$ (b) $n = 10$
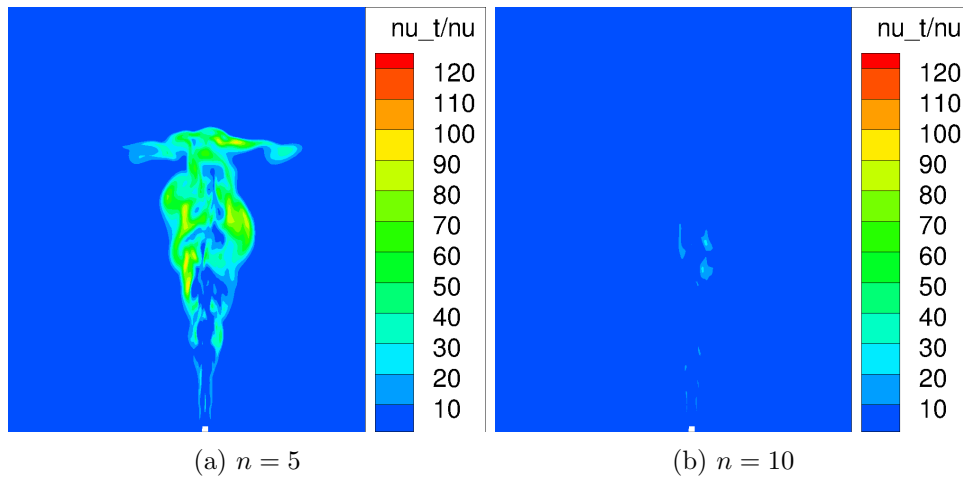
Figure 7.28: Eddy-viscosity ratio $\frac{\nu_t}{\nu}$, SST 2003 model with eddy-viscosity correction.

(a) $n = 5$ (b) $n = 10$
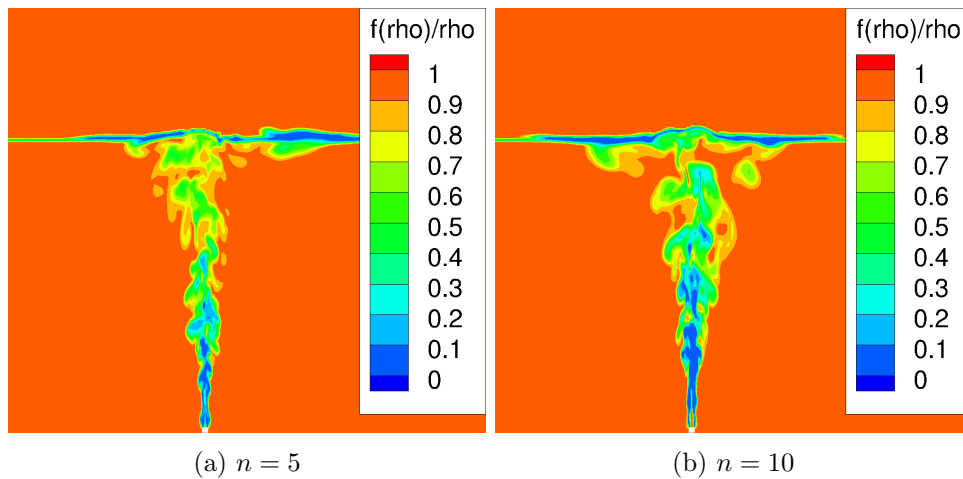
Figure 7.29: Eddy-viscosity correction factor $\frac{f(\rho)}{\rho}$ for the SST 2003 turbulence model with a correction factor of $n = 5$ and $n = 10$. In this plot value of the Correction factor of 1 indicates no correction, whereas a value of 0 implies maximum correction.

Finally in figure 7.24 again isosurfaces of the air volume fraction at 0.1 are shown for the turbulence model with eddy-viscosity correction. It can be seen that the interface is more unstable, and for the also some shedded pockets of air are again visible. For the higher correction factor the disturbances on the interface are more widespread.

Based on this it can be concluded that the correction has a positive effect, the interface is more unsteady which is in agreement with the expectations. It can

however be questioned whether this unsteadiness is physical. By suppressing the eddy-viscosity the influence of the turbulence model at the interface is suppressed, which leads back to a sort of the implicit LES in this region and the corresponding requirements for the grid and numerical settings.

(a) $n = 5$ (b) $n = 10$
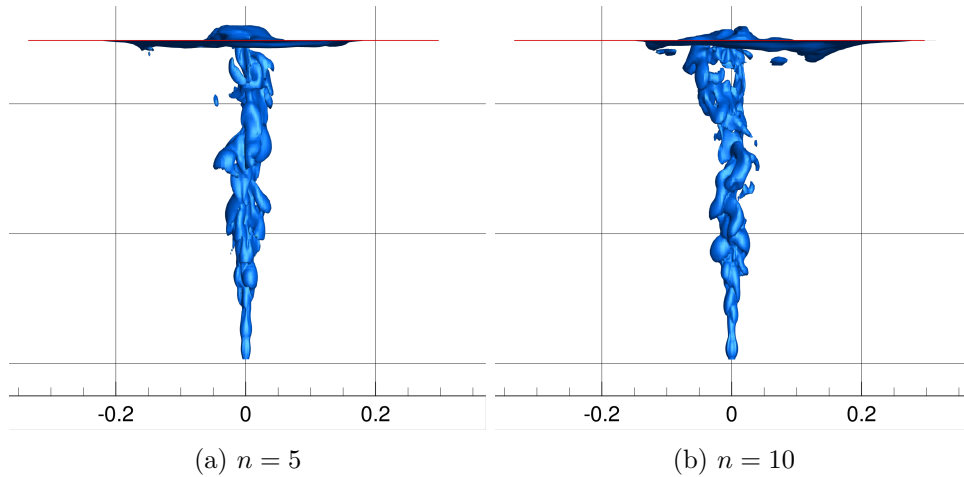
Figure 7.30: Isosurface of the air volume fraction at $AVF = 0.1$ for the SST 2003 model with and without eddy-viscosity correction. The red horizontal line indicates the free surface.

Influence of the eddy-viscosity correction on the spread

The spread based on the vorticity is shown in figure 7.31. It can be seen that the results lie in the same range, and have the same slope. The only exception is the SST 2003 model with $n = 10$. This effect might be attributed to a lack of statistical convergence. Generally the width close after the start-up process is larger than the width at steady state. Due to computational costs this simulation was not extended.

Advanced turbulence models

It is observed that the choice of turbulence model influences the distribution of air in the plume. Also the influence of an eddy-viscosity correction was looked into to increase the disturbances on the interface. Although it appears to have a realistic effect there are some doubts concerning this approach. The main downside of this is that by decreasing the eddy-viscosity in effect the influence of the turbulence model at the interface dynamics is reduced. If the effect of the turbulence model is suppressed the question arises whether the turbulence model has effect on the simulation. Consequently two more advanced turbulence models are used, namely the $k - \sqrt{k}L$ (KSKL) model and the EARSM.
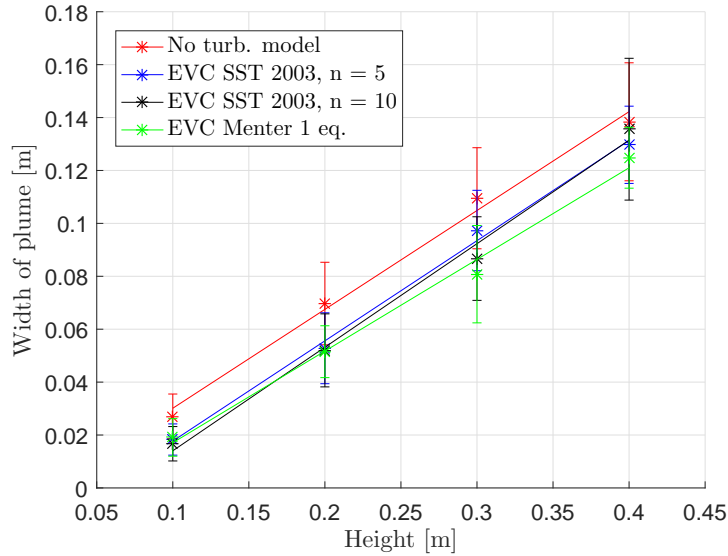
Figure 7.31: Width based on vorticity for two turbulence models with eddy-viscosity correction. The errorbars indicate the standard deviation.

KSKL results

First the $k - \sqrt{k}L$ turbulence model was applied, this model is described in section 5.4.4. The isosurface of the air volume fraction at $AVF = 0.1$ is shown in figure 7.32a. It can be seen that the interface is relatively unstable, however it is known that for this model also an over prediction of eddy-viscosity near interfaces occurs. This is visible in figure 7.32b where it is visible that values as high as 850 are achieved. An explanation might be that the turbulence model is not yet in its scale adaptive model and requires a smaller cell size and time step size, or a larger unsteadiness in the flow Pereira et al. [59].

The large eddy-viscosity gives rise to believe that here also an eddy-viscosity correction might be beneficiary, again as correction factors $n = 5$ and $n = 10$ are used. The isosurface of the air volume fraction and eddy-viscosity ratio for $n = 5$ are shown in figure 7.32c and 7.32d respectively, and for $n = 10$ in figure 7.32e and 7.32f. Finally the density is plotted and shown in figure 7.33.

There is a considerable difference between this result and the same plot for the $k - \omega$ turbulence model as shown in figure 7.27 and figure 7.28. The air is less spread out, this is in line with expectations bases on the higher eddy-viscosity ratio. Also for the $k - \sqrt{k}L$ near the surface a large S shaped pattern is visible wheres for a $k - \omega$ model only smaller vortices occur. This shape is caused by the plume which waves from side to side, such oscillatory movement is reported for jets in confined domains [65]. This instability is less visible for a $k - \omega$ model. Finally clustering of air along the plume is visible, this is most clearly visible in for the case with eddy-viscosity correction.

(a) AVF, no correction

(b) $\frac{\nu_t}{\nu}$, no correction

(c) AVF, $n = 5$

(d) $\frac{\nu_t}{\nu}$, $n = 5$

(e) AVF, $n = 10$

(f) $\frac{\nu_t}{\nu}$, $n = 10$
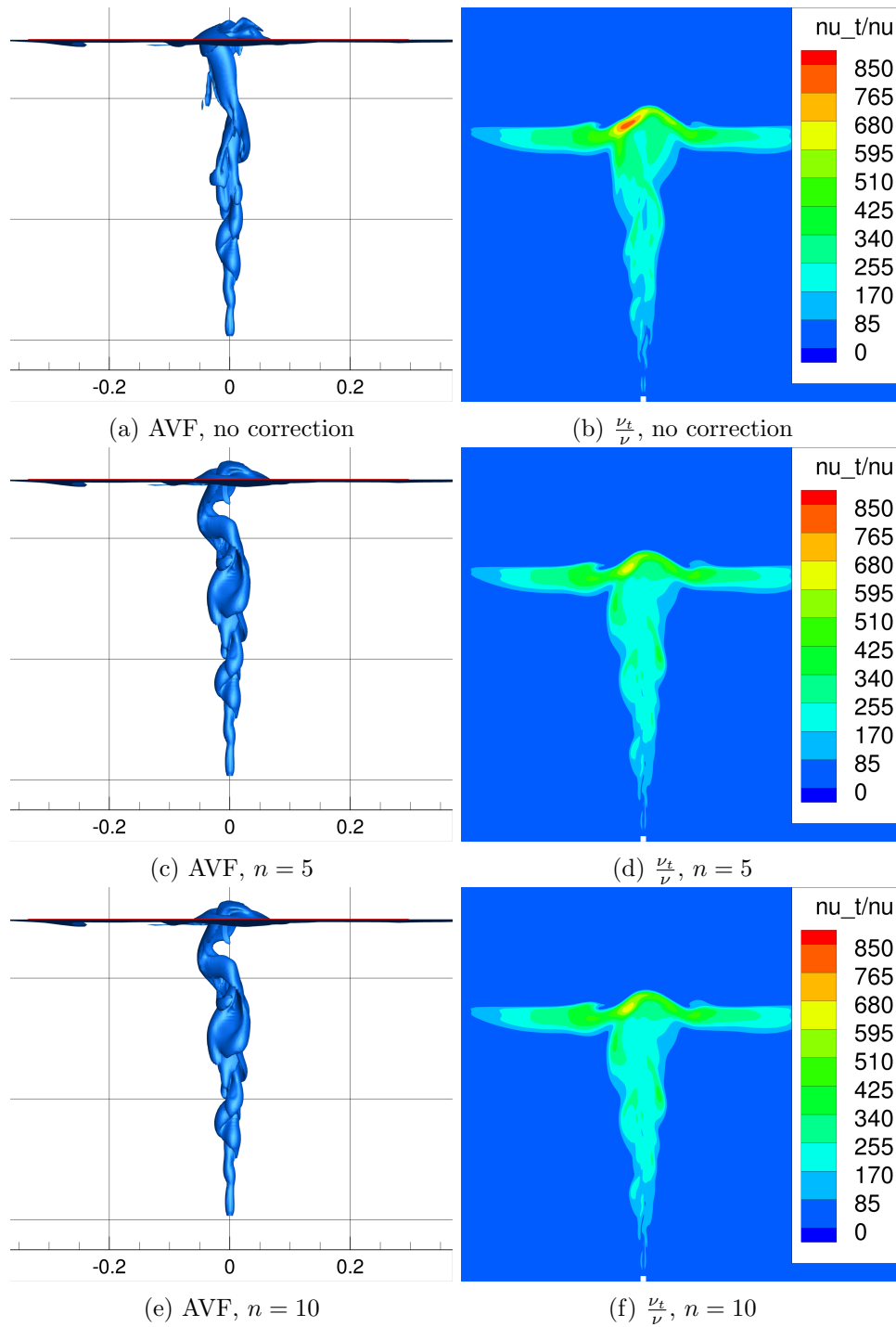
Figure 7.32: Isosurface of the air volume fraction at $AVF = 0.1$ and eddy-viscosity ratio for the $k - \sqrt{k}L$ turbulence model, with and without eddy-viscosity correction.

(a) No correction   (b) $n = 5$
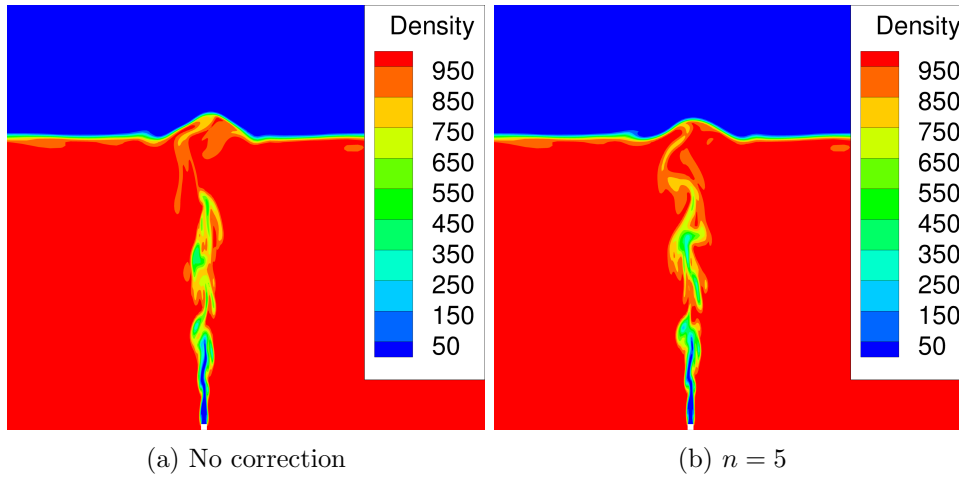
Figure 7.33: Density using the $k - \sqrt{k}L$ turbulence model, without and with eddy-viscosity correction, $n = 5$.

It is interesting to note that whereas the eddy-viscosity correction strongly influenced the eddy-viscosity and the corresponding shape of the interface for a $k - \omega$ model, this effect does not take place for a $k - \sqrt{k}L$ model. The difference in eddy-viscosity is smaller, and so is the difference in shape of the air in the plume. There is some difference between no correction and the use of correction, however whether the factor is 5 or 10 does not appear to influence the result.

To investigate the effect of the correction the correction factor normalized with the density $\frac{f((\rho))}{\rho}$ is plotted in figure 7.34. A value of 1 means no correction, a value of 0 is complete correction. It can be seen that around the nozzle and the free surface the most correction occurs (the blue regions). This is expected since here there is an interface. However higher in the plume below the free surface less correction occurs. Due to the spread of air the density here is close to the density of water and therefore the correction is low (as can be seen in figure 7.26). Here again the S shape can be observed, and it is visible that whereas in some regions there is correction in other regions no correction occurs. This is in contrast with the correction for a $k - \omega$ model where the correction is active in a larger area, as can be seen in figure 7.30. Consequently the inclusion of correction has less effect for a $k - \sqrt{k}L$ model than for a $k - \omega$ model.

EARSM results

Secondly the Explicit Algebraic Reynolds stress model (EARSM) was applied, this model is described in section 5.6.

The advantage of this model is that due to the extra transport equations solved for the Reynolds stresses it is closer to reality, the downside is a lower convergence. This becomes clear when the L_∞ norm is plotted, as is shown in figure 7.35. It

(a) $n = 5$ (b) $n = 10$
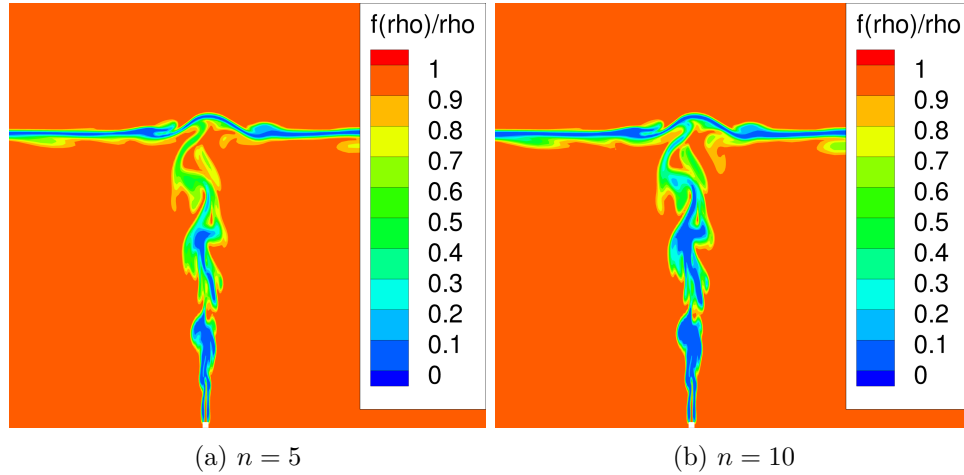
Figure 7.34: Eddy-viscosity correction factor $\frac{f(\rho)}{\rho}$ for the $k - \sqrt{k}L$ turbulence model with a correction factor of $n = 5$ and $n = 10$.

can be seen that the average order of convergence for the time steps which converge properly (in figure 7.35 time steps 200 - 202) lies in the order of 10^{-5}, whereas for a $k - \sqrt{k}L$ model this was in the order of 10^{-7}. However it is also observed that some time steps (such as 211 to 222 in figure 7.35) do not converge well. After a number of stagnated time steps, the solution resumes to converge.

To investigate the lack of convergence during these time steps a plot of the density near the nozzle is shown in figure 7.36. It can be seen that between $T = 0.21$ s and $T = 0.22$ s a pocket of air is formed on the nozzle which is then consequently released. This time interval during which the pocket is formed corresponds to time step 210 to 220, so during the forming of a pocket of air on the nozzle the solution does not converge well. This effect keeps occurring throughout the entire simulation. It also occurs for a $k - \sqrt{k}L$ model, however here the lack of convergence is usually limited to a few time steps. It is likely that this model requires smaller time steps and grid cells to converge properly, due to computational expense this was not further investigated.

Next to this the isosurface of the air volume fraction at $AVF = 0.1$ is shown in figure 7.37a and a density plot is shown in figure 7.37b. Again an unstable interface can be observed. In the density plot larger vortices are visible, which suggests a larger instability in the plume which oscillates from left to right.

Advanced turbulence models results

As stated these more advanced turbulence models lead to a difference in shape of the plume. However more important is the spread based on vorticity since this is directly related to the surface elevation. The spread is plotted in figure 7.38. It can be seen that the inclusion of an eddy-viscosity correction for the $k - \sqrt{k}L$ model
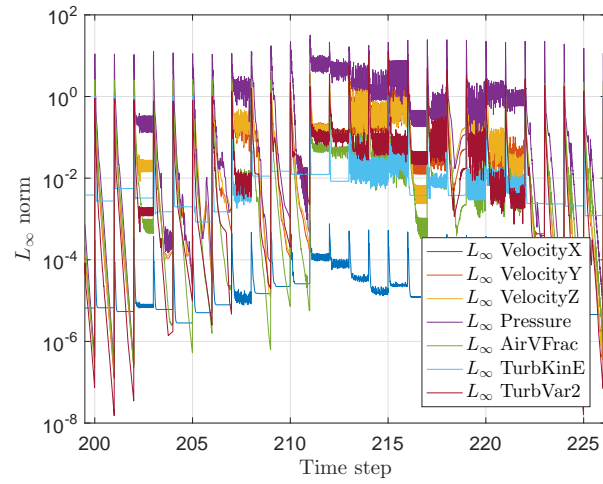
Figure 7.35: Convergence behavior using an EARSM turbulence model. A number of representative time steps is shown.

(a) $T = 0.20$ s   (b) $T = 0.21$ s   (c) $T = 0.22$ s   (d) $T = 0.23$ s
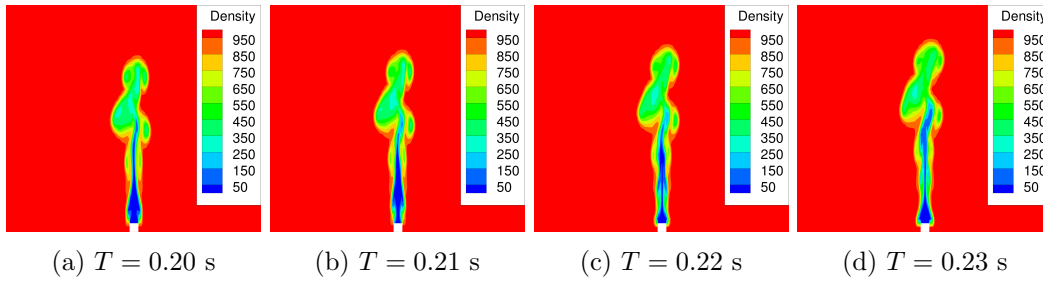
Figure 7.36: Development of the density near the nozzle for the EARSM model.

(a) AVF   (b) Density
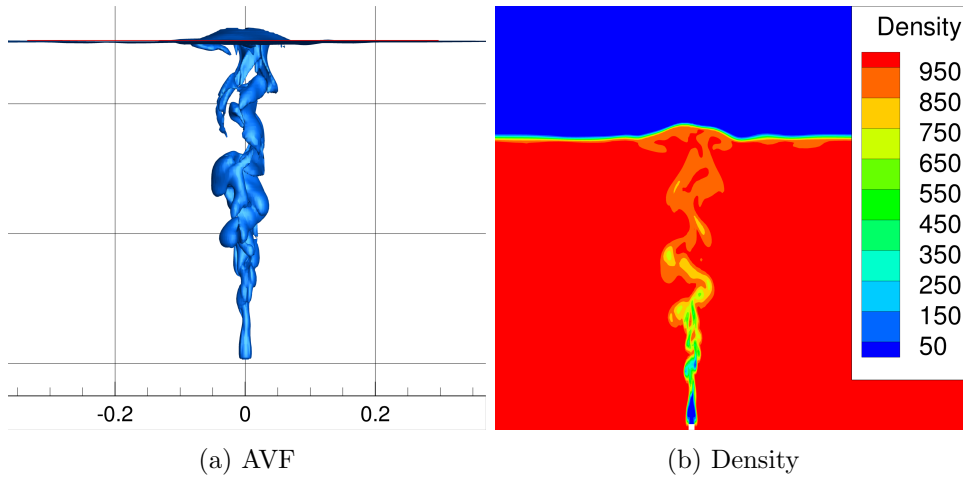
Figure 7.37: Isosurface of the air volume fraction at $AVF = 0.1$ and density for the EARSM.

has virtually no effect on the spread. The spread for a $k - \sqrt{k}L$ model has a lower slope than for an EARSM. The spread for an EARSM is almost identical to the spread for a SST 2003 model with eddy-viscosity correction. Based on this and the convergence behavior the choice is made to use the $k - \sqrt{k}L$ turbulence model for the submarine simulations in chapter 8.
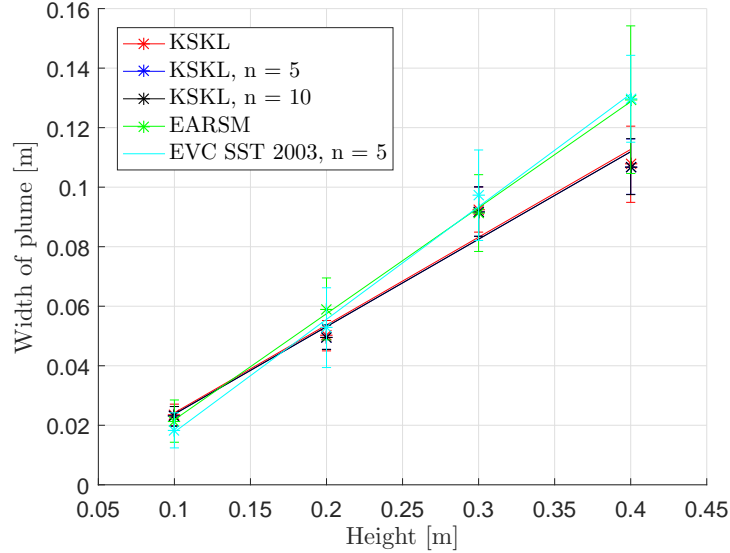
Figure 7.38: Width based on vorticity for the $k - \sqrt{k}L$ turbulence model, with and without eddy-viscosity correction, and for the EARSM. The errorbars indicate the standard deviation.

7.8.6 Effect on free surface

In the previous sections the influence of the different turbulence models on the spread was looked into, this section looks into the elevation of the water surface. To this end the height of the interface (the location where the air volume fraction equals 0.5) is tracked in an area of 0.6 by 0.6 m above the nozzle. The highest elevation of the surface over time was determined. Of this elevation the mean, the maximum value and the height of the peak at start up are determined. The results are shown in table 7.8.

It can be seen that the differences for the mean and the maximum value of the surface elevation are limited. Generally one equation turbulence models, such as the Menter 1 equation and Spalart-Allmaras, lead to a lower mean value than two equation models. The inclusion of an eddy-viscosity correction does little to the height of the elevation. It is interesting to note that for an EARSM the resulting surface elevation is lower than for for instance a $k - \sqrt{k}L$ model. A $k - \sqrt{k}L$ model also gives a large peak at the start up, this peak is almost twice the mean value. This peak does not occur for an EARSM. Both these differences are related to the eddy-viscosity produced by the model. Around the free surface the eddy-viscosity

Table 7.8: Surface elevation for different turbulence models.

Turbulence model	Mean [m]	Max [m]	Peak at start up [m]
No turbulence model	0.022	0.040	0.060
Spalart-Allmaras	0.015	0.017	0.037
Menter 1 eq.	0.016	0.018	0.021
Menter 1 eq., $n = 5$	0.018	0.024	0.024
SST 2003	0.030	0.040	0.040
SST 2003, $n = 5$	0.025	0.036	0.036
SST 2003, $n = 10$	0.025	0.040	0.040
KSKL	0.033	0.040	0.065
KSKL, $n = 5$	0.035	0.040	0.065
KSKL, $n = 10$	0.035	0.040	0.065
EARSM	0.020	0.030	0.030

produced by an EARSM has a value in the order of 2 to 3 times the eddy-viscosity produced by the $k - \sqrt{k}L$ model. This increased eddy-viscosity leads to a more stable free surface and consequently a lower elevation.

7.9   Validation of the turbulent jet

To validate the results a comparison is made using two different validation sources. First of the results are compared to the theoretical model as described in section 7.1.

The comparison plot is shown in figure 7.39, where the width of the theoretical model, the simulation without turbulence model and the SST 2003 turbulence model with and without eddy-viscosity correction are plotted. It can be seen that the trend of all three simulations is similar to the theoretical model, but they all underpredict the spread. The underprediction can be related to the fact that the width as calculated is a mean over the width fluctuating in time, whereas the theoretical width assumes that the width is constant over time. The theoretical width includes all turbulence and is therefore larger than the width averaged over time. Nevertheless since the slope of the curves is approximately equal the results do compare with the theoretic description.

Secondly, the results of the simulations are compared with experimental data. Norwood and Chen [57] looked into bubble jets in water in a similar case. They looked into a number of different nozzles and different water-air ratios. Since the results mainly focus on noise generated by the nozzle, the results from the simulations are compared on a visual basis with the few images given. Only the case with a circular nozzle, with a diameter of 0.016 m, and with an inflow of pure air is used. The airflow used corresponds to a velocity of $V_{gas} = 2.64$ m/s. Norwood and Chen [57] used a tank with a height of 60 cm, however in the images it is vis-
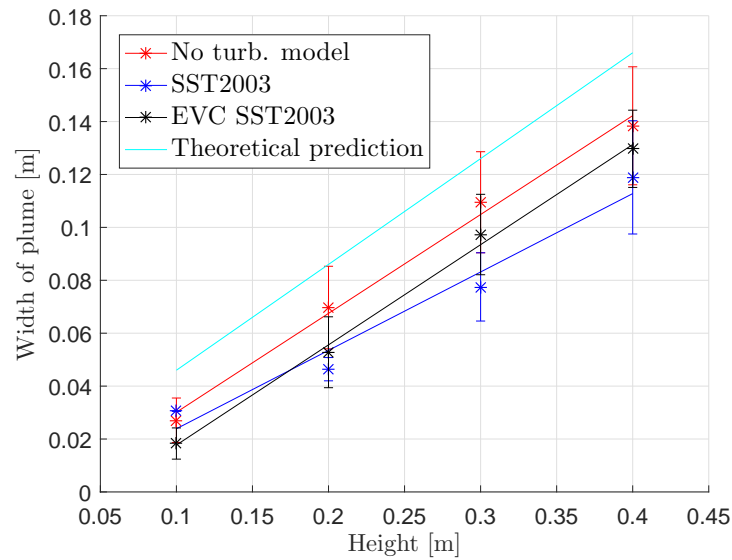
Figure 7.39: Width based on vorticity for two turbulence models with eddy-viscosity correction. The errorbars indicate the standard deviation.

ible that the nozzle is not located at the bottom. It is estimated that the nozzle is located around 50 cm below the water surface, so this height is maintained in the simulations. Unfortunately no images of the disturbances at the surface are given.

It is observed that the general shape of the plume differs. Norwood and Chen [57] describe that in the experiment a large gas pocket forms on the nozzle, which separates and rises. This is probably caused by pressure fluctuations in the pipe through which the air flows. In the numerical solution this process does not occur in the same way since a constant exit velocity is prescribed. Consequently, in the numerical solution the air is more evenly distributed. This pressure effect can also be evaluated using simulations, however it lies outside of the scope of this research. From the photo and information given by Norwood and Chen [57] it can be concluded that the width of the jet on the top lies between 15-20 cm, which is in the same order of magnitude as in the numerical solution.

7.10   Conclusions

To conclude this chapter a short overview of the main findings is given.

For a gas jet in water it is concluded that the system is buoyancy driven. To be able to accurately model the plume a complete 3D domain is needed. The grid must be fine enough to capture shedded pockets of air and to allow the plume to spread. The system is unsteady, consequently to obtain a statistically converged result it is observed that it is necessary to simulate at least two to three times the time needed for the plume to reach the surface.

Based on a grid sensitivity study it is estimated that the discretization uncertainty for the surface elevation has an order of magnitude of around 12%. This uncertainty will be also be used in chapter 8 as uncertainty for the submarine simulations. Ideally for the submarine simulations a second grid sensitivity study is performed, due to time considerations this was not yet done.

It is observed that the solution is sensitive to the choice of turbulence model. A number of one and two equation models are used. Conventional models have little effect on the spread and surface elevation, but they strongly affect the distribution of air in the plume. Rather than spread out the air is concentrated in the core of the plume. This effect can be remedied to some extend by the use of an eddy-viscosity correction, however it is unknown to what degree the solutions then resemble the physics. Consequently two more advanced turbulence models, the $k - \sqrt{k}L$ model and EARSM, are used. The results for the spread an elevation are still in the same order of magnitude, and the distribution of air is more as would be expected based on experiments. The convergence behavior of the $k - \sqrt{k}L$ model is better than that of the EARSM, therefore the $k - \sqrt{k}L$ model is deemed to be the most suitable turbulence model for this case. The convergence behavior can be improved by using a velocity profile for the inflow rather than a uniform inflow, this does lead to additional computational cost. Also there is little effect on the plume shape and surface elevation, a change velocity profile only has a local effect.

Chapter 8

Submarine modeling

The third modeled case is the modeling of a submerged exhaust on a submarine sail. For the Walrus class, model scale experiments were performed at MARIN in the nineties on request of the RDM [79, 80]. In this chapter the results of these tests are described and analyzed, followed by the numerical modeling of the case and the associated results. In all images the flow direction is from right to left, unless indicated otherwise. Due to confidentiality in some figures no axes are shown.

8.1 MARIN model tests for the Walrus class

Three series of model tests were performed into the performance of the submerged exhaust of the Walrus class submarines. These test were performed in Wageningen by the MARIN, on behalf of the RDM (the yard which build the Walrus class submarines). The first series is described by Van Hees [79], in this series two different configurations were evaluated.

The second series is described by Van Wijngaarden [80]. The movie of the experiments of the second series is lost during the last twenty-five years. The third series is not disclosed due to confidentiality and safety reasons, and the final configuration of the Walrus class submarines is not described, nor are the results of the final version shown.

Since the results of the second and third series are not available these series of tests can not be used as validation material. In the current work due to time limitations a restriction is made to the original configuration as described by Van Hees [79].

Original configuration

The original configuration (as built by the RDM) of the exhaust of the Walrus class consisted out of two openings with a grill (one on port side, one on starboard side) on the sail. Each grill was 770 by 206 mm with around 1000 circular shaped openings with a diameter of 10 mm. The schematics of the original configuration are shown

in figure 8.1a, an image of the model of the original configuration is shown in figure 8.1b. In these images the top back end of the sail is shown. This configuration is simulated on model scale using a rectangular opening with a fine netting in the opening.

(a) Schematics   (b) Photograph of the model
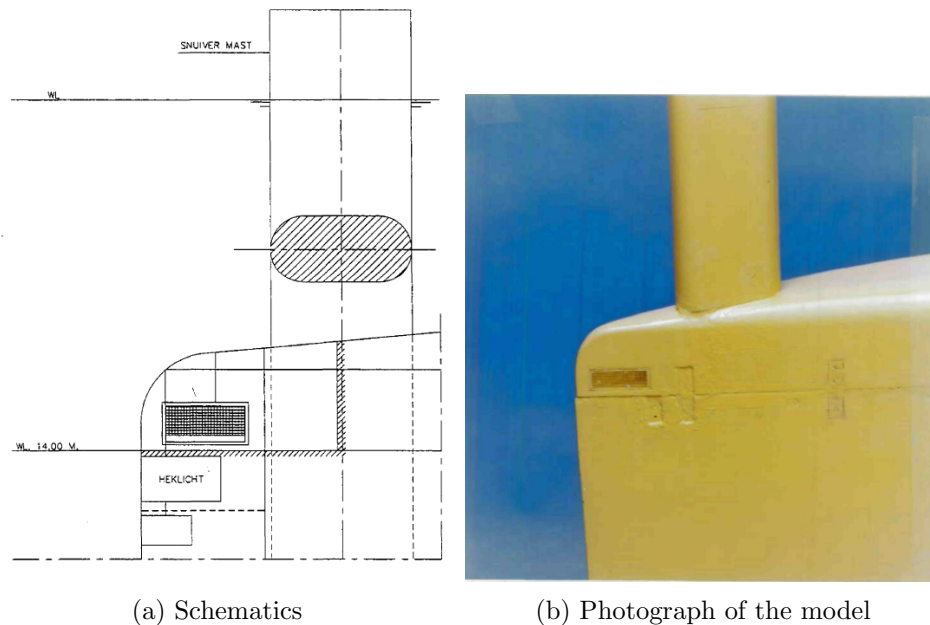
Figure 8.1: The schematics and the model of the original configuration (configuration I) of the submerged exhaust of the Walrus class [79].

Van Hees [79] states that all gas jets contribute to a single large gas jet with a theoretical jet diameter of 1.4 m. Due to the limited space in which the jet is present and the non-uniform flow due to the presence of the snorkel the surface tension is not the dominant factor in the size of the bubbles. Consequently the jet will break up into bubbles with an average theoretical diameter of 0.4 m.

Using the flow rate an estimated 25 m^2 on the water surface is disturbed, which is in agreement with the observations from the sea trials. Here it was concluded that 20 m^2 of the surface was disturbed.

Change in configuration

To reduce the surface elevation caused by the exhaust gases it was attempted to decrease the diameter of the bubbles to 0.1 m. This leads to an increased rising time and distance between the exhaust and the location behind the exhaust where the bubbles surface. The number of formed bubbles and the disturbed area are increased, which must lead to a decrease in surface elevation.

Based on the proposition for changes a design for a fixture on the sail was made by the Drawing Office Marine (*Tekenkamer Marine*) of the RDM. This second con-

figuration was also tested on model scale and is described by Van Hees [79]. These results were still not acceptable, which lead to a second series of model tests described by Van Wijngaarden [80]. It was concluded that this configuration reduces the disturbance on the surface with approximately 50%. This was not deemed satisfactory which lead to the third and final series of tests.

In the current work a restriction is made to the original configuration as described by Van Hees [79].

Model tests

At MARIN model tests with a model of the sail with snorkel at scale 1:13 were performed. A photograph of the model as used in the tests can be found in figure 8.2.

Figure 8.2: Photograph of the model used in the model tests by MARIN. In this photograph the adapted exhaust is fitted on the sail [79].

The exhaust is tested in different conditions. On model scale only the starboard side of the exhaust system is modeled, so half the amount of exhaust gases are used. For the tests a exhaust flow ϕ_V of 6.3 m^3/s on full scale is used, so 3.15 m^3/s for the starboard exhaust. The tests are done in atmospheric conditions, so the scaling factor for the amount of gas is

$$\lambda^{2.5} = 609. \tag{8.1}$$

On model scale this leads to a gas flow of $\phi_V = 5 \cdot 10^{-3}$ or $\phi_V = 1 \cdot 10^{-2}$ m^3/s respectively. On the sail a simplified snorkel is placed to simulate the flow conditions around the exhaust. During the tests video recordings were made of the exhaust plume, both above and below the water surface. On the snorkel a length scale is placed to estimate the height of surface elevation. The tests were performed with a ship speed of $V_S = 4$ kt on full scale, so on model scale the free stream velocity is $U_\infty = 0.571$ m/s.

Photographs of the exhaust plume, on the surface and submerged, are shown in figure 8.3 and figure 8.4 respectively. The effect on the disturbance on the surface is described in section 8.7.
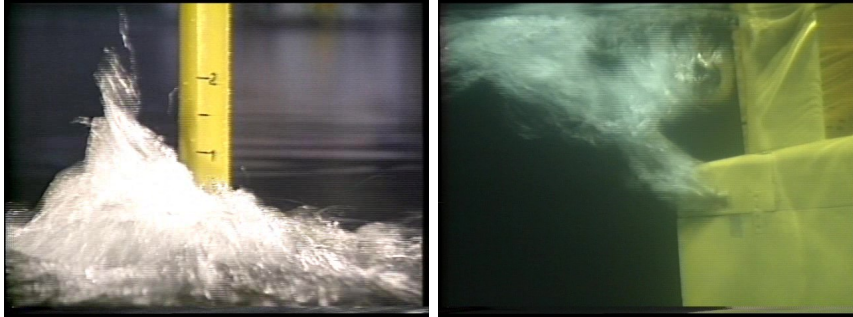
Figure 8.3: Surface and submerged photo, $\phi_V = 5 \cdot 10^{-3}$ m^3/s [79].

Figure 8.4: Surface and submerged photo, $\phi_V = 1 \cdot 10^{-2}$ m^3/s [79].

In the tests it can be seen that, periodically, large bubbles rise almost vertically behind the snorkel. The observed frequency of this phenomenon is around 2 Hz, which in agreement with the theoretic vortex frequency of the snorkel in these conditions using the equation

$$St = \frac{f_s D}{U_\infty}. \tag{8.2}$$

Van Hees [79] concludes that the large bubbles are caused by Von Kármán vortices behind the snorkel, in which multiple bubbles merge and form a large bubble. Due the large bubble size these bubbles rise rapidly and directly behind the snorkel. The large bubbles cause peaks in height of the gas-water pile. It is stated that on real scale the observed frequency will be around 1 Hz, since on model scale only one side of the exhaust is simulated. Van Hees [79] notes that the gas-water pile in real life may appear larger, due to water droplets which form a mist.

8.2   Image processing

Van Hees [79] gives an estimate of the mean height of the disturbance on the surface. Based on the movie a more accurate estimate of the height of the elevation on the water surface is obtained here by means of video processing. In this section the method, results and associated uncertainties of the processing are addressed.

From the movie the mean height is determined, this process is described in this section and shown in figure 8.5. Each frame of the movie was transferred to a binary image based on color values using the Matlab Color Separator app. Each pixel is compared with threshold values for the RGB (red, blue and green) values, this selection is shown in figure 8.6. Using the selection only the plume remains visible. In figure 8.5a an original image can be seen, figure 8.5b shows the binary image based on the color of each pixel. Next the loose pixels are filtered out, this is done by removing white dots which consist out of less than 30 pixels together, this yields figure 8.5c. From this the height of the pile is determined by detecting the edge. The edge is determined by taking the highest white pixel after filtering, this result is shown in figure 8.5d in which the edge is laid over the original image. Lastly the values in pixels are transferred to values in [m], this is done based on the scale visible on the snorkel.

From the detected edge both the maximum, the mean height and the standard deviation of the mean are determined. The height which is used for the validation process is mean of the height of 500 highest pixels. This way sudden peaks are filtered out. Also the width on one third of the height of the maximum is calculated to estimate the width of the water pile.

8.3   Image processing uncertainty

In the analysis as shown here a number of sources of error and uncertainty can be identified:

- The color separator used in Matlab. This separator determines the edge of the pile based on the Red Green Blue (RGB) values of each pixel. The margins are set relatively tight to filter out reflection of light on the snorkel. As a consequence the height is underpredicted since the spray is often not detected, as can be seen in figure 8.5d.

- The filtering. To remove loose spots, such as reflections on the snorkel, a filter is applied which removes dots consisting of less than 30 pixels. Again part of the spray is removed, as can be seen by comparing figure 8.5b and figure 8.5c.

- The camera quality. In the image obtained horizontal lines can be observed, this is especially visible in the spray region. If the image is converted to a binary image these stripes remain visible but they interfere with the filtering. Small horizontal stripes on the top can be accidentally removed by the filtering process.

(a) The original image.

(b) Binary image based on color thresholds.

(c) Binary image after filtering.

(d) Obtained edge of plume overlaid on the original image.
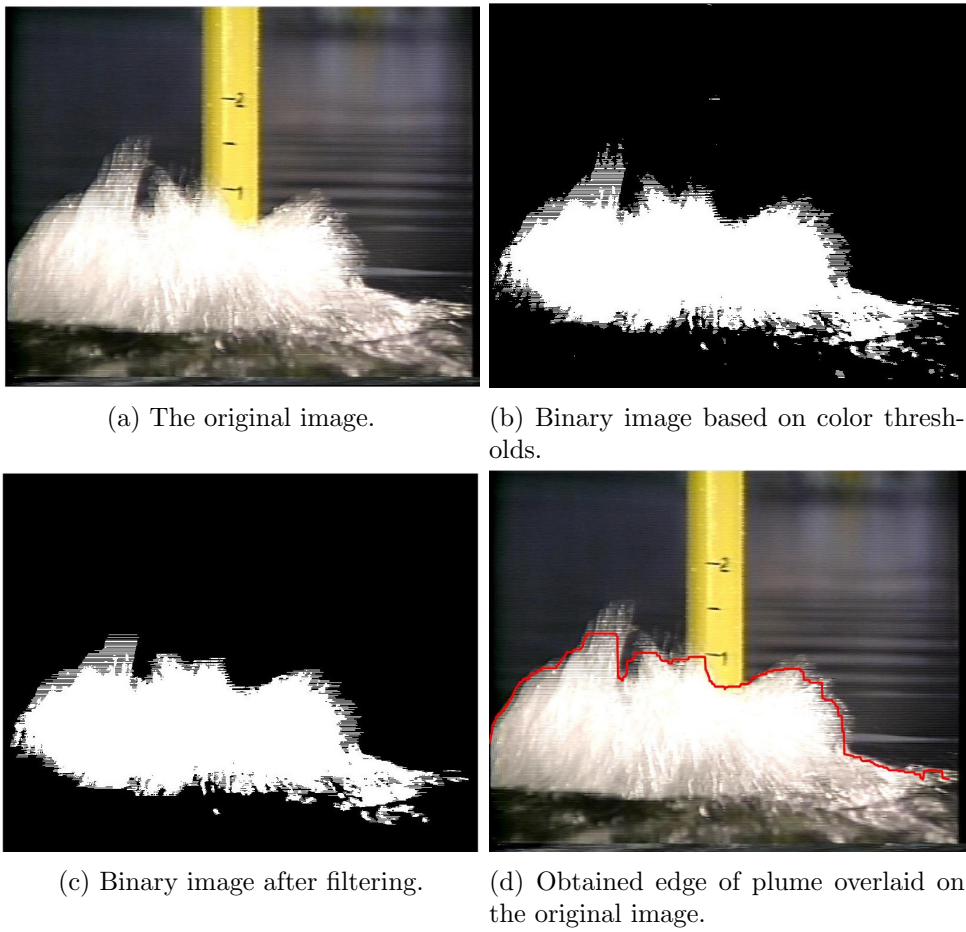
Figure 8.5: The processing of an image to obtain the height of the disturbance on the surface.
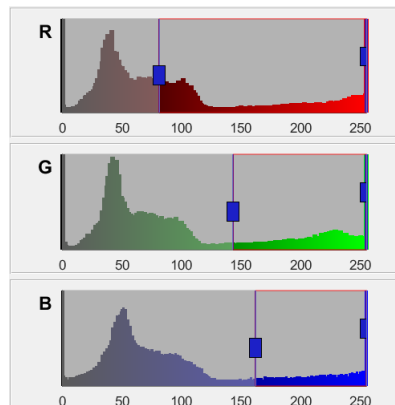
Figure 8.6: Selection of the RGB (red, green and blue) values per pixel to determine the plume in the picture.

- The experimental setup. Due to the placement of the camera the height is underestimated, this effect can be seen in figure 8.7. This effect depends on the longitudinal distance between the top of the water pile and the snorkel, which is in full scale several meters, and on the distance of the camera to the snorkel. This distance is unknown.

- The height reference as indicated on the snorkel. From the indicated numbers on the snorkel the height is estimated, however the scale is not accurate.

- The location of zero height. This is also estimated based on the indicated numbers on the snorkel, and it is compared with the value as can be seen in the fourth experiment. However due to camera vibrations this value is not constant. Also the water surface is lowered due to the disturbance caused by the snorkel, this is not taken into account.
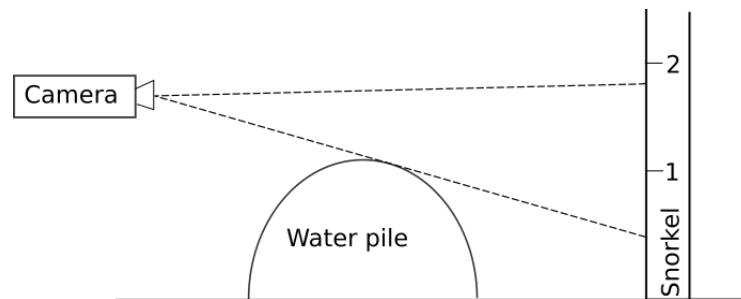
Figure 8.7: The experimental setup. In this image the under prediction due to the viewing angle can be seen. The image is not to scale.

The combination of these factors leads to an uncertainty in the results, based on figure 8.5d it can be concluded that the height is under predicted, at some point up till 60 pixels. This corresponds to an under prediction of 0.4 m. It must be noted that this under prediction only occurs for a peak which consists out of a fine spray. Based on an average peak height of approximately 2 m, the maximum height as shown in the figures can have an error as high as 20%.

It is estimated that the error for the mean height of the water pile is in the order of 10%. Van Hees [79] does not estimate the uncertainty since in this research the focus lies more on a comparison between different configurations, and since the experimental setup is the same it is assumed that the uncertainty remains the same. The uncertainty based on the current experiments can be improved by improving the color separation algorithm and improving the filtering, however due to the unknown distance between the camera and the snorkel it is presumed this uncertainty can not be reduced below 10%.

8.4   Modeling assumptions

A number of assumptions and simplifications are used in the numerical modeling. These assumptions and their influence are described in this section.

For the modeling of the plume near the submarine, ideally the flow around the complete submarine would be modeled. However, to the decrease the computational effort, a restriction is made to the sail of the submarine. As a consequence of the absence of the hull the flow speed along the sail is lower, since a moving body in a fluid displaces the fluid surrounding the body. Based on continuity therefore the flow speed must increase. This effect is limited since the flow is not constricted in any way. Furthermore the horseshoe vortex generated by the connection of the sail to the hull is absent. Kuin [33] looked into the flow around a submarine hull with different sail configurations, in these results it is shown that the horseshoe vortex remains near the hull. This vortex does not influence the flow in the region of interest in this work. The vortex which mainly influences the flow in the region of interest is the vortex generated by the top of the sail, a wing tip vortex. This vortex is taken into account.

Also the control planes on the sail are not modeled. This is questionable since they can influence the flow near the exhaust and divert this flow either upwards or downwards. However in the model tests done at MARIN these control planes are also absent, and the decision was made to keep the modeled case similar to the validation material. It is recommended to look into the influence of the control planes on the flow.

Finally only the expelling of exhaust gases in still water will be investigated, so no waves on the free surface will be taken into account. This is both a restriction in computational effort as well as in cases which must be calculated. As a result the height over which the bubbles must rise to the surface remains constant. This is a sea condition which will rarely occur, however the argumentation for this restriction is twofold. First, the formation of the exhaust plume in calm seas can be extrapolated to the behavior in waves. The spread will increase with increased water depth (in a wave crest) so the height of the surface elevation will decrease, and vice versa. Secondly the demands for the size and height of the gas-water pile at the location where the plume surfaces is most stringent for calm seas. In case of a calm sea it is possible to identify a submarine based on the dimensions of the gas-water pile using radar. This is more difficult in a more severe sea state, since the gas-water pile is no longer the only elevation of the water surface.

8.5   Computational domain

The computational domain with dimensions is shown in figure 8.8. Here also the boundary conditions and the mesh are shown.

The incoming flow is modeled using an inflow boundary condition. The far field and top of the domain are modeled as pressure, this is also used for the outflow condition.. As bottom of the domain a slip wall is used, this is to partly model the influence of the top of the hull of the submarine. The boundary layer at the bottom is not generated, but no flow can move through the plane. Details of the mesh surrounding the sail are shown in figure 8.9.
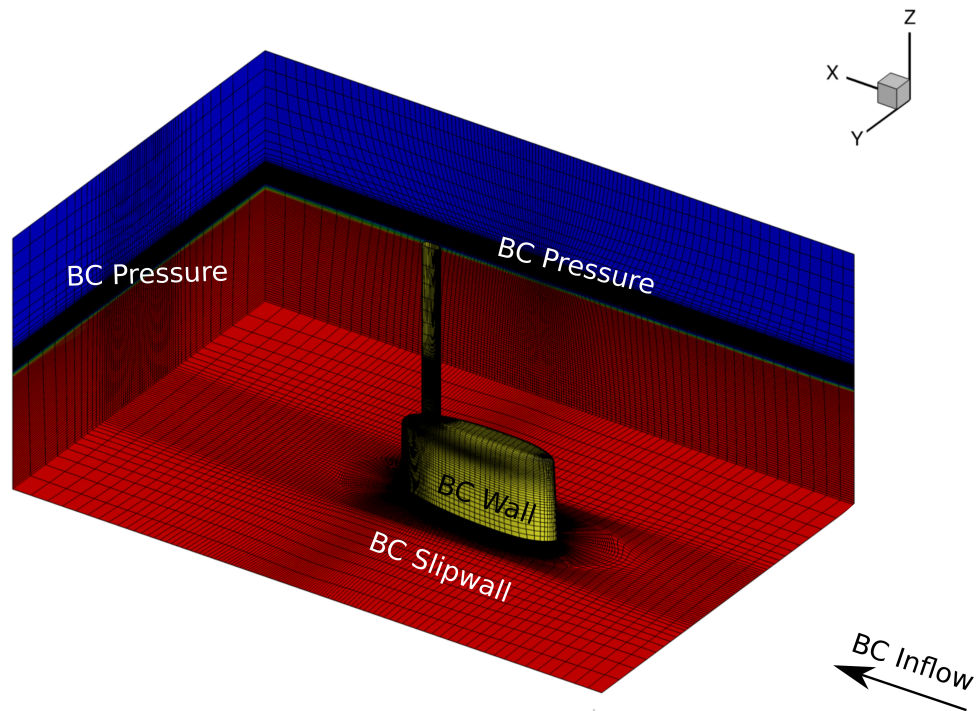
Figure 8.8: The computational domain of the submarine simulations with used boundary conditions. The red section indicates water, the blue section water. The submarine sail is shown in yellow. On the domain the coarse mesh is shown, the dimensions are in meters on model scale.

The grid consists out of an O grid surrounding the sail, with a H topology surrounding the exhaust. Surrounding the sail a refinement for the boundary layer is present. Three are available, their properties can be found in table 8.1. The maximum y^+ values around the sail have a magnitude of around 2 for the coarse grid and smaller than 1 for the finest grid.

In the mesh a refinement band should be located around the interface. Due to an error the interface is located beneath the refinement band in the grid. Consequently the cells containing the interface are larger than ideally and therefore the interface is more diffuse. This is visible in figure 8.10 where the grid on the midplane of the submarine is shown, together with the density. Due to time limitations in this work the grid is not improved, instead the effect of this error is investigated in section 8.6.

(a) Side view of the sail

(b) Detail of the exhaust, the exhaust is shown in red
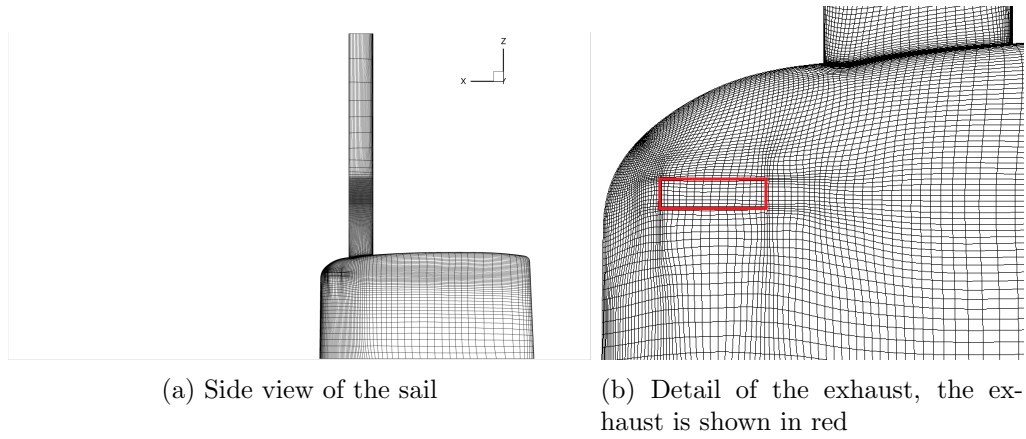
Figure 8.9: Details of the coarse grid.

Table 8.1: Submarine grids with their corresponding number of cells.

Grid	Number of cells
Coarse	$1.35 \cdot 10^6$
Medium	$4.52 \cdot 10^6$
Fine	$10.72 \cdot 10^6$
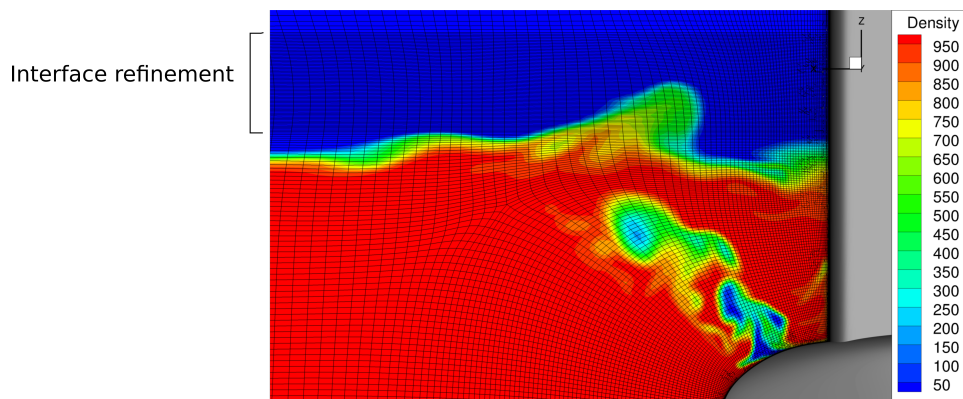
Figure 8.10: The mesh at the midplane of the submarine, with the interface refinement indicated.

8.6 Interface refinement effect

The influence of the refinement band around the interface on the result for the surface elevation is investigated for the turbulent jet. Two grids, one with an one without interface refinement are compared. For the cell size around the interface similar values as for the medium submarine grid are used. The surface elevation over time is shown in figure 8.11.

(a) With interface refinement   (b) Without interface refinement
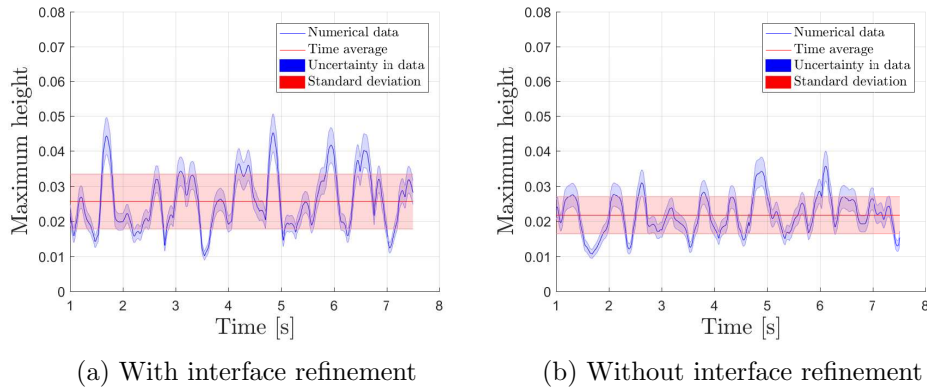
Figure 8.11: Surface elevation on a grid with interface refinement and without interface refinement.

The mean surface elevation on the grid without interface refinement is 15% lower than on the grid with interface refinement. Next to that the standard deviation is around 32% lower without interface refinement. The frequency of the peaks is in the order of 11% lower. These effects can be explained due to large cells around the interface. The elevation is spread out over a larger area and therefore more diffusive. Consequently disturbances are lower the peak heights are dampened. It is expected that a similar effect occurs for the submarine simulations.

8.7 Numerical results

Four situations were simulated for the first submarine configuration and are compared with the experiments by Van Hees [79]. First, the flow pattern surrounding the sail is investigated. Secondly, an exhaust flow on one side of the sail (the starboard side) is added, both a flow of $\phi_V = 5 \cdot 10^{-3}$ m^3/s and $\phi_V = 1 \cdot 10^{-2}$ m^3/s are modeled. Finally a exhaust flow $\phi_V = 5 \cdot 10^{-3}$ m/s on both exhausts, starboard and port side, is modeled.

8.7.1 No exhaust gas

In the first case the flow pattern surrounding the sail is investigated when no exhaust gases are dispelled. The flow is shown in figure 8.12. The convergence for this

simulation is shown in table 8.2. The y^+ values and the pressure coefficient C_p on the sail on the medium grid are shown in figure 8.13.
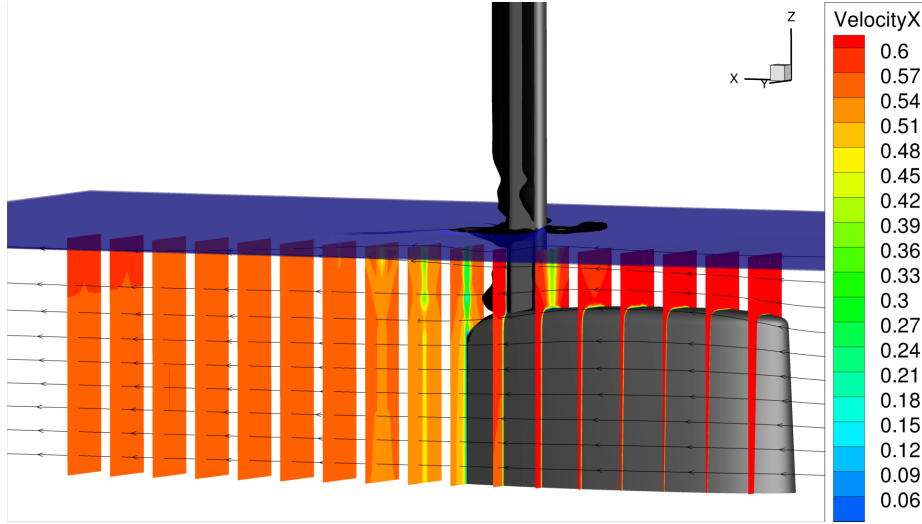
Figure 8.12: Flow around the sail. The slices show the velocity in x-direction together with streamtraces around the sail. The blue horizontal plane indicates the free surface. The black isosurface indicates the flow separation behind the snorkel mast.

Table 8.2: Order of magnitude of the achieved convergence for the flow around the sail without exhaust gases.

	L_2	L_∞
VelocityX	10^{-6}	10^{-3}
VelocityX	10^{-9}	10^{-6}
VelocityZ	10^{-7}	10^{-4}
Pressure	10^{-8}	10^{-6}
Air volume fraction	10^{-5}	10^{-3}
Turbulent kinetic energy	10^{-9}	10^{-6}
Turbulent variable 2	10^{-12}	10^{-9}

Van Hees [79] states that Von Kármán vortices behind the snorkel mast influence the result. The Reynolds number calculated for the mast is in the order 10^4 on model scale, or 10^6 on full scale. Lienhard [39] states that a Reynolds number in this range leads to a fully turbulent, narrow and disorganized wake without a vortex street. In the simulation no Von Kármán vortices are observed.

(a) y^+ (b) C_p
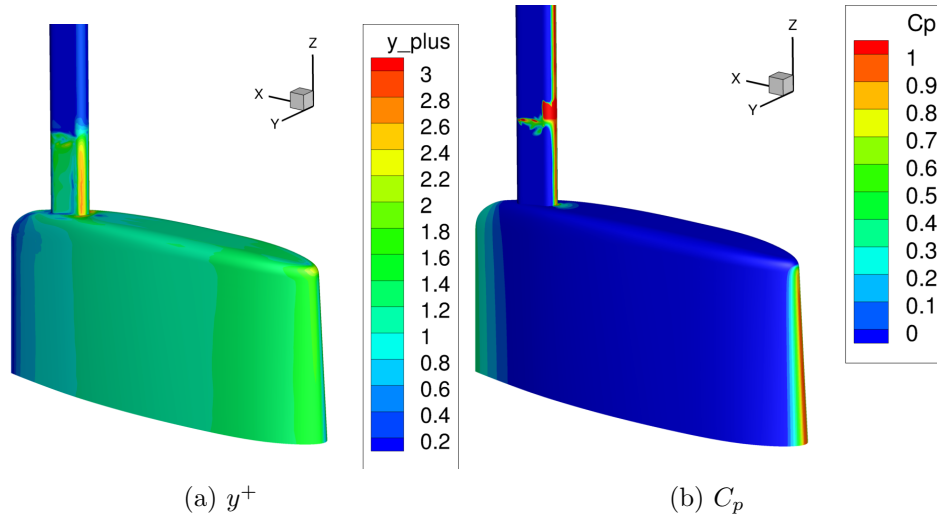
Figure 8.13: The dimensionless wall distance y^+ and the pressure coefficient C_p on the sail on the medium mesh.

8.7.2 Starboard exhaust with $\phi_V = 5 \cdot 10^{-3}$ m^3

Secondly, exhaust gases are dispelled through the starboard exhaust with $\phi_V = 5 \cdot 10^{-3}$ m^3. For these calculations both the coarse and the medium grid are used.

To obtain proper convergence smaller time steps are needed than for the turbulent jet. The mesh at the sail is refined to be able to capture the boundary layer. This is also the region through which the exhaust gases are dispelled, this leads to a high Courant number due to the high velocity of the gases. The convergence behavior for a number of representative time steps is shown in figure 8.14. Since the L_2 number is two orders of magnitude lower than the L_∞ norm it can be concluded that the convergence problems are local. The solution lacks convergence near the exhaust. For this grid and these settings a time step of $5 \cdot 10^{-4}$ is used, larger time steps lead to a diverging solution. Smaller time steps increase the convergence, however these lead to calculation times which are not feasible in this work.

The shape of the exhaust plume is shown in figure 8.15 and figure 8.16. It can be seen that even though the plume is expelled asymmetrically it is pulled into the wake of the sail and rises behind the sail. In the rear view it is visible that the spread in the direction perpendicular to the flow is almost equal for both directions.

It can be seen that some air is trapped directly behind the snorkel mast, whereas the bulk is transported upwards in with an angle of around 45°. The maximum surface elevation occurs between 20 to 30 cm behind the snorkel mast, which is in agreement with the observations on full scale stated by Van Hees [79]. After around 1.2 m the largest part of the gas has reached the surface.

In figure 8.17 a detailed view of the plume near the exhaust is shown. It can be observed that in the simulations also a pulsating behavior in the plume is present.

(a) L_2 norm

(b) L_∞ norm
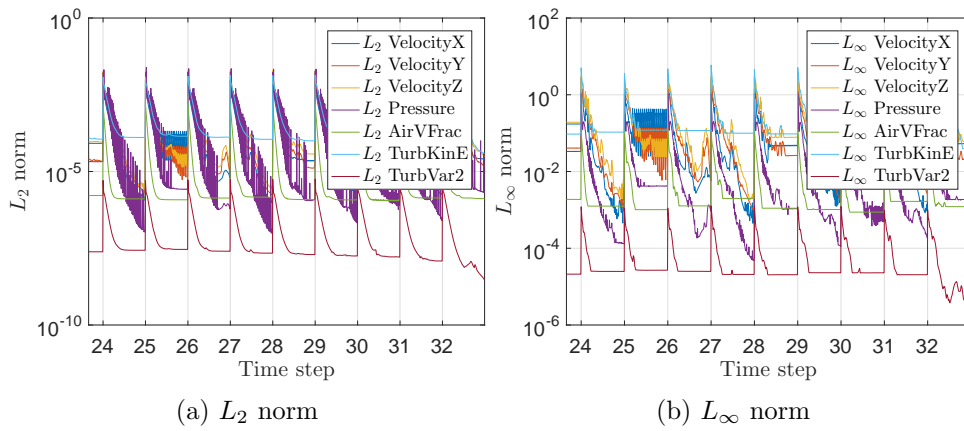
Figure 8.14: Convergence behavior for the starboard exhaust with $\phi_V = 5 \cdot 10^{-3}$ m^3. A number of representative time steps is shown.
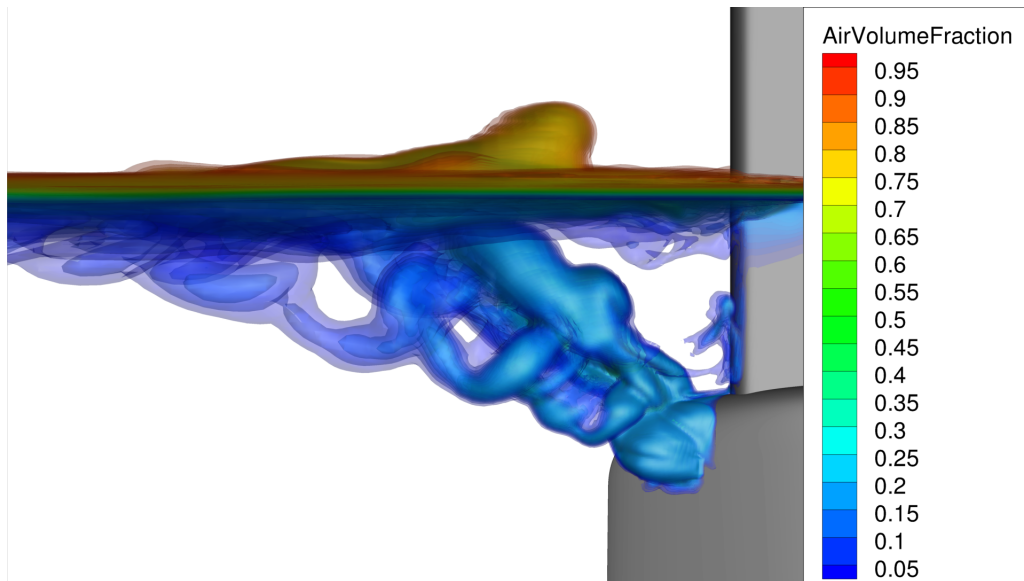
Figure 8.15: Side view of exhaust plume on starboard side with $\phi_V = 5 \cdot 10^{-3}$ m^3. The instantaneous isosurface of the density is shown.
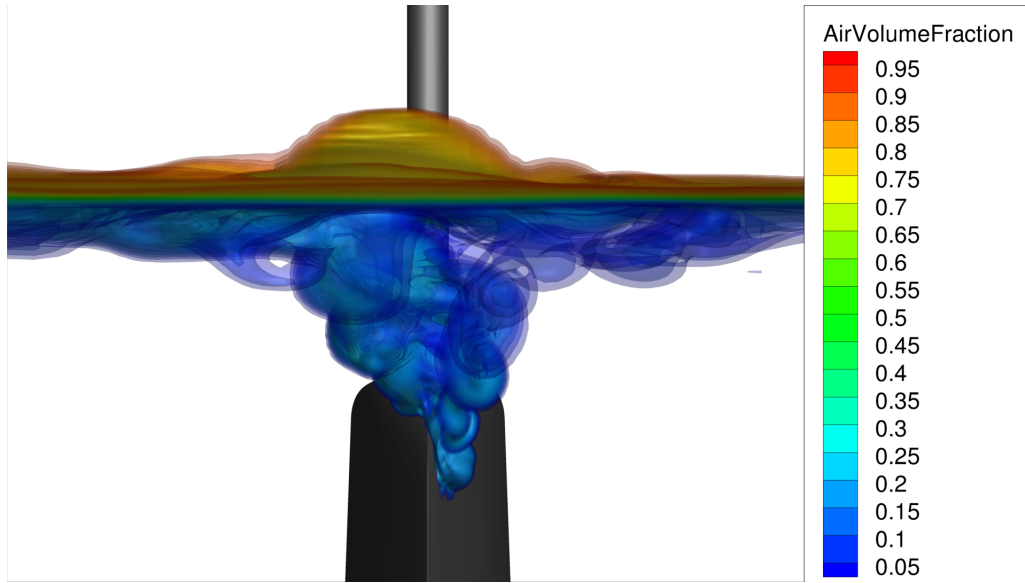
Figure 8.16: Rear view of exhaust plume on starboard side with $\phi_V = 5 \cdot 10^{-3}$ m^3. The instantaneous isosurface of the density is shown.

In the density plot, figure 8.17b, it is clearly visible that the plume consists out a number of regions with a high air volume fraction, separated by regions with a low air volume fraction. These kind of bubbles lead to a pulsating behavior in the disturbance on the surface. These pulsations are similar to the behavior described for the turbulent jet, as described in section 7.8.5. Van Hees [79] also describes these fluctuations and attributes this to Von Kármán vortices behind the snorkel, however as described in section 8.7.1 these are not observed in the simulations.

On the snorkel mast just beneath the water level a sheet of air can be observed which remains attached throughout the simulation. This air is present only in the first two cells in the boundary layer and remains attached due to the no-slip boundary condition. The layer leads to a decreased convergence, however the lack of convergence in the entire domain is dominated by the cells near the exhaust. A suggested remedy, known as a contact line correction, is tested but yields unsatisfactory results. In this correction a velocity is prescribed applied at cells at the wall, in contrast to the no-slip boundary condition.

The results for the mean surface elevation on the coarse and on the medium grid are shown in figures 8.18a and 8.18c respectively. In figure 8.18b and 8.18d the experimental results are shown. The experimental values are obtained using the method described in section 8.2, shown here is the average height of the water pile over time. The numerical results shown are the maximum of the surface elevation of behind the sail. It can be seen that the numerical result are in the same order as the experimental values. The result on the coarse grid is lower than the result on the medium grid, this is as expected since due to the larger cell size the interface is

(a) Isosurface of the density   (b) Density plot at the mid plane of the
                                        submarine.
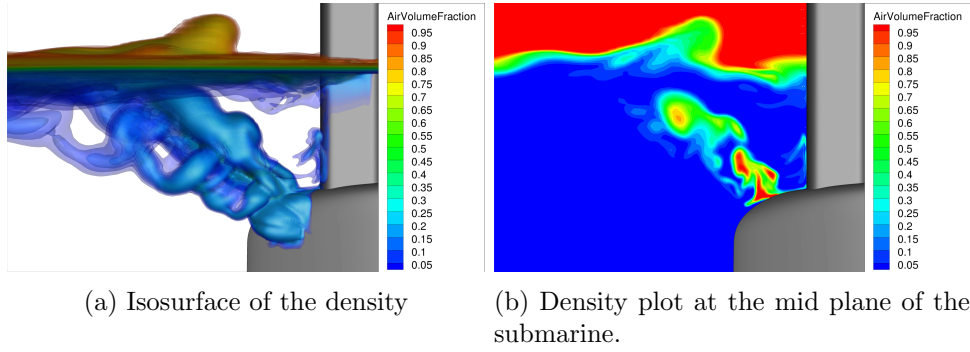
Figure 8.17: Detailed view of the plume seen from starboard side. The same time step is shown in both images

more diffusive, as observed in section 8.6. Also the standard deviation on the coarse grid is lower than on the medium grid.

For both the simulations the standard deviation of the results is lower than for the experiments. The validation of the result is described in section 8.7.3.

To obtain a result which is statistically converged in time a number of cycles must be obtained. To determine whether the mean and standard deviation of the maximum elevation have reached a steady state their development over time is shown in figure 8.19. Here two graphs are shown of the mean and standard deviation with an increasing sample size, the development is calculated with in- and decreasing time. It can be seen that the mean and standard deviation reach a constant value after around 1 s. Since here around 3 s are simulated it is concluded that the results are statically converged, and the simulation is not further extended.

8.7.3   Validation

Numerical results must be verified and validated. To verify the results for the submarine simulations again a grid sensitivity study should be performed, where both the influence of grid size and time step size is varied.

Due to computational expenses this is not done for the submarine simulations, here only two grids are used. The difference between the coarse and medium grid is an under prediction of the mean of 13% and of the standard deviation of 22%. This is in the same order of magnitude as the findings for the grid with and without interface refinement, were the under prediction was 15% and 30% respectively. With the current results it can not be stated that a grid independent solution was obtained, to this end also simulations on the finest grid must be performed. Here it is assumed that a grid independent solution was obtained with the medium grid. For the numerical uncertainty a pragmatic method is used, the uncertainty as determined for the turbulent jet in section 7.7 is used. Consequently it is assumed that the discretization uncertainty for the surface elevation has an order of magnitude of around 12%.

Figure 8.18: The mean height over time, and the mean of the mean height with associated standard deviation. The results on the coarse and medium grid, and the experimental results are shown. The results given are model scale values.
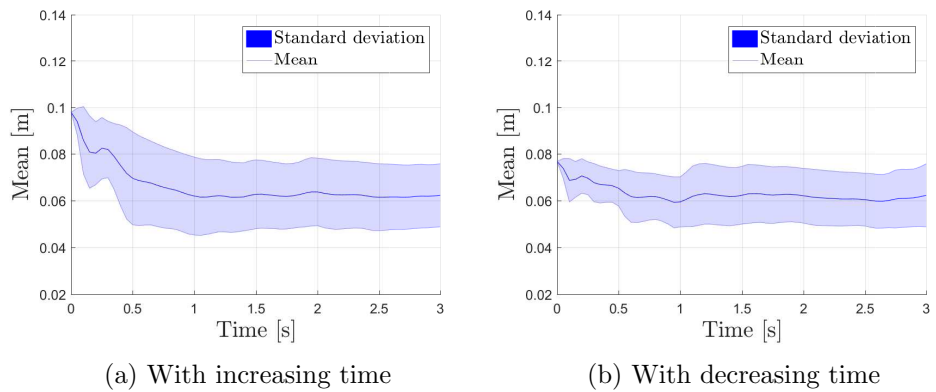
Figure 8.19: The development of the mean and standard deviation over time. The results given are model scale values.

The numerical results for the medium grid are validated against the experiments described by Van Hees [79] using the method as described in section 5.10. For this validation the results with the free surface outside of the grid refinement 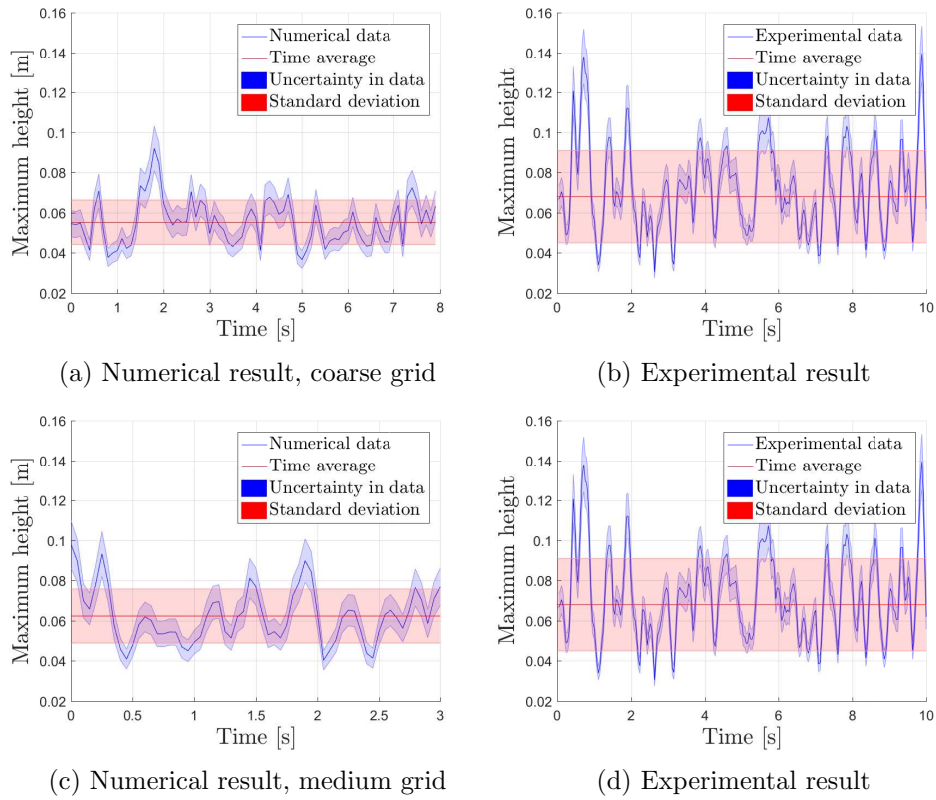band are used. It is noted that this effects the results. For the validation process three sets of results are used, the mean, the standard deviation and the frequency of the surface elevation, The values for the experiments and the simulations are shown in table 8.3.

Table 8.3: Mean, standard deviation (σ) and frequency (f) as calculated and as obtained from the movie of the experiments for the first exhaust configuration performed by Van Hees [79]. The results given are model scale values.

ϕ_V [m^3/s]	Numerical results			Experimental results		
	Mean [m]	σ [m]	f [Hz]	Mean [m]	σ [m]	f [Hz]
$5 \cdot 10^{-3}$	0.062	0.014	3.33	0.068	0.022	3.61

To validate the results the validation comparison error E and the validation uncertainty U_{val} are calculated. The validation comparison error is the difference between the numerical and the experimental result, whereas the validation uncertainty is the quadratic sum of the input uncertainty, the experimental uncertainty and the numerical uncertainty. The input uncertainty is assumed to be 0%, the experimental uncertainty is estimated to be 10% and the numerical uncertainty is assumed to be 12%. The values can be found in table 8.4. Based on these results it is concluded that the mean surface elevation and the frequency are validated against the experiments, however the standard deviation is not.

Table 8.4: Validation of the numerical results with the experiments for the first exhaust configuration with $\phi_V = 5 \cdot 10^{-3}$ [m^3/s].

	E	U_{val}	Conclusion
Mean	-8.2%	15.6%	$|E| < U_{val}$
Standard deviation	-41.3%	15.6%	$|E| > U_{val}$
Frequency	-7.6%	15.6%	$|E| < U_{val}$

In section 8.6 it is estimated that the lack of refinement around the free surface leads to an increase of the mean, standard deviation and frequency with a value of 15%, 32% and 11% respectively. If this increase is taken into account the results of the validation process change, as is shown in table 8.5. With this correction the mean, standard deviation and frequency are validated against the experimental values.

Care must be taken in using this approach, it is recommended to change the grid in such a way that the interface lies in the refinement zone. Nevertheless it can be concluded that the results are validated.

Table 8.5: Validation of the numerical results, corrected for the lack of grid refinement around the interface, with the experiments for the first exhaust configuration with $\phi_V = 5 \cdot 10^{-3}$ [m^3/s].

	E	U_{val}	Conclusion
Mean	5.5%	15.6%	$|E| < U_{val}$
Standard deviation	-13.2%	15.6%	$|E| < U_{val}$
Frequency	2.6%	15.6%	$|E| < U_{val}$

Chapter 9

Conclusions and recommendations

This chapter summarizes the main conclusions and gives two sets of recommendations, namely for further research and for the design of a submerged exhaust.

9.1 Conclusions

The results of the turbulent jet lead to the conclusion that for these applications a $k - \sqrt{k}L$ turbulence model yields the most physical results together with a decent convergence behavior. The influence of the temperature of the exhaust gases on the surface elevation is negligible, due to the marginal density differences. The main parameter which influences the surface elevation is the gas flow per area. The precise velocity profile and shape of the exhaust influence the result locally but do little to the general flow field. A velocity profile can be used to improve the convergence.

The surface elevation due to a submerged exhaust is modeled for a submarine. Only the submarine sail is taken into account. The mean surface elevation is predicted with an uncertainty in the order of 15% based on the sensitivity study done for the turbulent jet. When the result is compared with experimental data it can be concluded that the current modeling can be used for this problem. The modeling error of the numerical result is in the range imposed by the validation uncertainty. Also the standard deviation and frequency of the surface elevation are validated against the experiments.

Both in the experiments and in the simulations a pulsating behavior can be observed in the rising air. The air is trapped in the wake of the sail, out of this trapped air pockets of air rise which form the plume. These pockets generate the peaks in the surface elevation.

An important issue is the lack of proper convergence, due to the large velocity gradients at the exhaust. This is especially the case for the cells in the boundary layer. L_∞ norms are generally in the order 10^{-3}, but occasionally less. This lack

of convergence leads to an additional uncertainty in the estimate of the surface elevation. The use of a velocity profile for the exhaust gases does improve this but leads to a demand for smaller time steps. These smaller time steps lead to unfeasible calculation times.

Based on these results it is concluded that the use of the RANS code ReFRESCO is possible for the modeling of a submerged exhaust of a submarine. It is estimated that this uncertainty is in the order of $15 - 20\%$.

9.2   Recommendations for further research

For further research there are two main areas which should be investigated more in depth.

The first concerns turbulence models. The solution is sensitive to the choice of turbulence model. Only limited validation material was available for the turbulent jet, therefore the models are mainly compared to each other. To obtain a better understanding of the physical realism of the solution a more extensive validation of the turbulent jet is necessary. To this end additional experiments are necessary. For the turbulence models themselves it is concluded that the more advanced models, the $k-\sqrt{k}L$ model and the EARSM, yield the most physical result. For both of these models questions remain to be answered. For the $k - \sqrt{k}L$ model it is interesting to see to what extend the model makes use of its scale adaptive properties, how this depends on the grid size and how to what extend this influences the solution. For the EARSM it is recommended to see whether the use of a velocity profile and a decreased time step size lead to better convergence. The additional physics in this model include anisotropic turbulence, it is interesting to determine the degree of anisotropy in the solution and whether that is needed to accurately predict a turbulent jet. Next to that other turbulence models could be used, such as LES, DES and PANS. Due to time limitations these are not yet evaluated for the turbulent jet.

Secondly it is recommended to do additional experimental research to obtain a better dataset for validation for the submarine simulations. Due to the fact that the experiments were performed more than 25 years ago, and were done in a more quantitative manner, essential dimensions of the setup are not available. Also the camera quality is not optimal. Due to this the validation uncertainty is large which reduces the quality of the validation.

In this work a number of assumptions were made. For further research it is recommended to look into four aspects.

First the two assumptions for the computational domain must be evaluated, namely the absence of the control planes on the sail and the presence of the submarine hull. The flow around the sail is influenced by the appendages and the hull which might effect the disturbance on the surface.

Secondly the effect of different exhaust shapes must be looked into. It is expected

that the detailed shape (for instance the size of the openings through which the air flows) has little influence but an increase in area of the exhaust does matter. It is interesting to see how this effects the surface elevation and to what extend these differences can be captured with the current modeling. Next to that the it can be investigated in what way the design can be modified to reduce the surface elevation.

Thirdly scaling effects must be looked into. To this end it is recommended to perform simulations on full scale and compare them with the full scale results from the Walrus class. For this comparison data from either the sea trials or from the submarine in its current configuration can be used.

Finally incoming waves by wind or swell can to be taken into account. These waves lead to changing height over which the plume rises and therefore a change both in spread and in disturbance on the surface. It is observed that an increased rising distance of 10 cm on model scale leads to a surface elevation which is almost half the current surface elevation.

9.3 Recommendations for the exhaust design

In this work no study into the design of the exhaust was performed. Nevertheless based on the results some recommendations for the design of a submerged exhaust can be given.

It is concluded that the main parameter on the surface elevation is the amount of exhaust gas per area of the exhaust. Therefore to decrease the surface elevation the exhaust area should be as large as possible. Since the exhaust gases are trapped in the wake of the sail and rise from there a wide exhaust has little effect, the largest effect can be obtained by increasing the length of the exhaust.

Secondly as stated the gases are trapped in the wake behind the sail and the snorkel mast. Together with the navigation periscope the snorkel mast is always up when snorkeling. The snorkel mast is the largest mast on the sail, therefore to decrease the wake and the trapping of air it is recommended to locate the snorkel mast further forward relative to the exhaust. This way the spread of the exhaust gases is increased, and the peaks in the surface elevation are reduced.

Finally it is observed that an exhaust located further beneath the surface leads to a lower surface elevation. A trade-off must be made between the signature demands and the requirement for the backpressure in the exhaust system.

Bibliography

[1] W. Addy Majewski. What are diesel emissions, September 2012. URL `https://www.dieselnet.com/tech/emi_intro.php`.

[2] S.S. Aleyasin, M.F. Tachie, M. Koupriyanov, and T. Epp. Low Reynolds number effects on jets issuing from round and elliptic orifices. In *ICHMT DIGITAL LIBRARY ONLINE*. Begel House Inc., 2015.

[3] J. Boussinesq. Essai sur la théorie des eaux courantes. mémoire des savants étrangers. *Ac. Sc. Paris, XXVIII*, 1877.

[4] C.E. Brennen. *Fundamentals of Multiphase Flow*. Cambridge University Press, 2005. ISBN 9780521848046. URL `https://books.google.nl/books?id=F7hEfx2GUPYC`.

[5] J. Brouwer, J. Tukker, and M. Van Rijsbergen. Uncertainty analysis of finite length measurement signals. In *The 3rd International Conference on Advanced Model Measurement Technology for the EU Maritime Industry (AMT13), Gdansk, Poland*, pages 260–274, 2013.

[6] J. Brouwer, J. Tukker, and M. Van Rijsbergen. Uncertainty analysis and stationarity test of finite length time series signals. In *The 4th International Conference on Advanced Model Measurement Technology for the Maritime Industry (AMT15), Istanbul, Turkey*, 2015.

[7] C.M. Coats and H. Zhao. Transition and stability of turbulent jet diffusion flames. In *Symposium (International) on Combustion*, volume 22, pages 685–692. Elsevier, 1989.

[8] O. Coutier-Delgosha, R. Fortes-Patella, and J.L. Reboud. Evaluation of the turbulence model influence on the numerical simulations of unsteady cavitation. *Journal of Fluids Engineering*, 125(1):38–45, 2003.

[9] B. Cushman-Roisin. *Environmental Fluid Mechanics*. John Wiley & Sons, Inc., 2014. URL `https://engineering.dartmouth.edu/~d30345d/books/EFM/`.

[10] L. d'Agostino and M.V. Salvetti. *Fluid Dynamics of Cavitation and Cavitating Turbopumps*. CISM International Centre for Mechanical Sciences. Springer Vienna, 2008. ISBN 9783211766699. URL `https://books.google.nl/books?id=B5rXBLCzI8QC`.

[11] S. Delvoye. Simulation and analysis of the flow around an underwater exhaust with FreSCo. Master's thesis, Institut des Science de l'Ingénieur de Toulon et du Var - ISITV, 2009.

[12] H. Dol, J. Kok, and B. Oskam. Turbulence modelling for leading-edge vortex flows. In *40th AIAA Aerospace Sciences Meeting & Exhibit*, page 843, 2002.

[13] D.A. Drew and R.T. Lahey. Application of general constitutive principles to the derivation of multidimensional two-phase flow equations. *International Journal of Multiphase Flow*, 5(4):243–264, 1979.

[14] L Eça and M Hoekstra. On the influence of the iterative error in the numerical uncertainty of ship viscous flow calculations. In *26th Symposium on Naval Hydrodynamics*, pages 17–22, 2006.

[15] L. Eça and M. Hoekstra. Verification and validation for marine applications of CFD. *International Shipbuilding Progress*, 60(1-4):107–141, 2013.

[16] L. Eça and M. Hoekstra. A procedure for the estimation of the numerical uncertainty of cfd calculations based on grid refinement studies. *Journal of Computational Physics*, 262:104–130, 2014.

[17] Y. Egorov, F.R. Menter, R. Lechner, and D. Cokljat. The scale-adaptive simulation method for unsteady turbulent flow predictions. part 2: Application to complex flows. *Flow, Turbulence and Combustion*, 85(1):139–165, 2010.

[18] R. Fortes-Patella, O. Coutier-Delgosha, and J. Reboud. Evaluation of the turbulence model influence on the numerical simulations of unsteady cavitation. *J. Fluids Eng*, 125(1):38–45, 2003.

[19] B. Gharraee, C. Eskilsson, R. Bensow, G. Vaz, et al. Numerical Simulation of Cavitation on a Horizontal Axis Tidal Turbine. In *The 26th International Ocean and Polar Engineering Conference*. International Society of Offshore and Polar Engineers, 2016.

[20] J. Hawkes, G. Vaz, S. Turnock, S. Cox, and A. Philips. Software performance analysis of massively-parallel hydrodynamics simulations. In *11th International Conference on Hydrodynamics (ICHD)*, 2014.

[21] R. Hogan. Expanded uncertainty and coverage factors for calculating uncertainty, December 2015. URL `http://www.isobudgets.com/expanded-uncertainty-and-coverage-factors-for-calculating-uncertainty/`.

[22] J. Hua and J. Lou. Numerical simulation of bubble rising in viscous liquid. *Journal of Computational Physics*, 222(2):769–795, 2007.

[23] J. Hua, P. Lin, and J.F. Stene. Numerical simulation of gas bubbles rising in viscous liquids at high Reynolds number. *Moving Interface Problems and Applications in Fluid Dynamics, Contemporary Mathematics*, 466:17–34, 2008.

[24] IAPWS. Revised release on surface tension of ordinary water substance. Technical report, The International Association for the Properties of Water and Steam, 2014.

[25] M. Ishii. Thermo-fluid dynamic theory of two-phase flow. *NASA STI/Recon Technical Report A*, 75:29657, 1975.

[26] C.O. Iyogun and M. Birouk. Effect of sudden expansion on entrainment and spreading rates of a jet issuing from asymmetric nozzles. *Flow, turbulence and combustion*, 82(3):287–315, 2009.

[27] S.T. Johansen, N.M. Anderson, and S.R. De Silva. A two-phase model for particle local equilibrium applied to air classification of powders. *Powder technology*, 63(2):121–132, 1990.

[28] S.H. Jongsma, E.T.A. Van der Weide, and J. Windt. Implementation and Verification of a Partitioned Strong Coupling Fluid-Structure Interaction Approach in a Finite Volume Method. In *12th International Conference on Hydrodynamics (ICHD)*, 2016.

[29] I. Kataoka and A. Serizawa. Bubble flow, September 2016. URL `http://www.thermopedia.com/es/content/8/`.

[30] M. Kerkvliet, G. Vaz, N. Carette, and M. Gunsing. Analysis of U-type anti-roll tank using URANS: sensitivity and validation. In *ASME 2014 33rd International Conference on Ocean, Offshore and Arctic Engineering*, pages V002T08A031–V002T08A031. American Society of Mechanical Engineers, 2014.

[31] C.M. Klaij and C. Vuik. SIMPLE-type preconditioners for cell-centered, colocated finite volume discretization of incompressible Reynolds-averaged Navier–Stokes equations. *International Journal for Numerical methods in fluids*, 71(7):830–849, 2013.

[32] A.H. Koop, C.M. Klaij, and G. Vaz. Viscous-flow calculations for model and full-scale current loads on typical offshore structures. In *MARINE 2011, IV International Conference on Computational Methods in Marine Engineering*, pages 3–29. Springer, 2013.

[33] R.W.J. Kuin. Hydrodynamic improvements of a generic submarine using viscous flow calculations. Master's thesis, University of Twente, 2013.

[34] P.R. Kulkarni, S.N. Singh, and V. Seshadri. The smoke nuisance problem on ships - a review. *International Journal of Maritime Engineering*, 2005.

[35] P.K. Kundu, I.M. Cohen, and D.R. Dowling. *Fluid Mechanics*. Elsevier Science, 2015. ISBN 9780124071513. URL `https://books.google.nl/books?id=EehDBAAAQBAJ`.

[36] A.S. Langman, G.J. Nathan, J. Mi, and P.J. Ashman. The influence of geometric nozzle profile on the global properties of a turbulent diffusion flame. *Proceedings of the combustion institute*, 31(1):1599–1607, 2007.

[37] L. Larsson, H.C. Raven, and J.R. Paulling. *Ship Resistance and Flow*. Principles of naval architecture. Society of Naval Architects and Marine Engineers, 2010. ISBN 9780939773763. URL `https://books.google.nl/books?id=5zi8bwAACAAJ`.

[38] B.E. Launder and D.B. Spalding. The numerical computation of turbulent flows. *Computer methods in applied mechanics and engineering*, 3(2):269–289, 1974.

[39] J.H. Lienhard. *Synopsis of lift, drag, and vortex frequency data for rigid circular cylinders*, volume 300. Technical Extension Service, Washington State University, 1966.

[40] E.J. List. Turbulent jets and plumes. *Annual review of fluid mechanics*, 14 (1):189–212, 1982.

[41] J. Magnaudet and I. Eames. The motion of high-Reynolds-number bubbles in inhomogeneous flows. *Annual Review of Fluid Mechanics*, 32(1):659–708, 2000.

[42] M. Manninen, V. Taivassalo, and S. Kallio. On the mixture model for multiphase flow, 1996.

[43] *Estimation of Numerical Uncertainty for Steady and Unsteady Flows*. MARIN, April 2016.

[44] *Numerical uncertainty analysis - user manual*. MARIN, April 2016.

[45] MARIN. ReFRESCO description, November 2016. URL `http://www.refresco.org/`.

[46] S. McElman, A. Koop, E.J. de Ridder, and A. Goupee. Simulation and Development of a Wind-Wave Facility for Scale Testing of Offshore Floating Wind Turbines. In *ASME 2016 35th International Conference on Ocean, Offshore and Arctic Engineering*, pages V006T09A035–V006T09A035. American Society of Mechanical Engineers, 2016.

[47] F.R. Menter. Two-equation eddy-viscosity turbulence models for engineering applications. *AIAA journal*, 32(8):1598–1605, 1994.

[48] F.R. Menter and Y. Egorov. Revisiting the turbulent scale equation. In *IU-TAM Symposium on One Hundred Years of Boundary Layer Research*, pages 279–290. Springer, 2006.

[49] F.R. Menter and Y. Egorov. The scale-adaptive simulation method for unsteady turbulent flow predictions. part 1: theory and model description. *Flow, Turbulence and Combustion*, 85(1):113–138, 2010.

[50] F.R. Menter, Y. Egorov, and D. Rusch. Steady and unsteady flow modelling using the $k - \sqrt{k}L$ model. In *Ichmt Digital Library Online*. Begel House Inc., 2006.

[51] A. Meslem, R. Greffet, I. Nastase, and A. Ammar. Experimental investigation of jets from rectangular six-lobed and round orifices at very low Reynolds number. *Meccanica*, 49(10):2419–2437, 2014.

[52] Ministerie van Defensie. Movie of the sea trial of Hr. Ms. Zeeleeuw, 1990.

[53] Ministerie van Defensie. Onderzeeboten, September 2016. URL https://www.defensie.nl/onderwerpen/materieel/inhoud/schepen/onderzeeboten.

[54] B.R. Morton. Forced plumes. *Journal of Fluid mechanics*, 5(01):151–163, 1959.

[55] R.F. Mudde and O. Simonin. Two-and three-dimensional simulations of a bubble plume using a two-fluid model. *Chemical Engineering Science*, 54(21): 5061–5069, 1999.

[56] K.G. Nayar, D. Panchanathan, G.H. McKinley, and J.H. Lienhard V. Surface tension of seawater. *Journal of Physical and Chemical Reference Data*, 43(4): 043103, 2014.

[57] C. Norwood and L. Chen. Water injection for bubble noise reduction. In *Proceedings of ACOUSTICS*, 2004.

[58] F.S. Pereira, L. Eça, and G. Vaz. On the order of grid convergence of the hybrid convection scheme for RANS codes. *CMNI2013*, pages 1–21, 2013.

[59] F.S. Pereira, G. Vaz, and L. Eça. On the use of Hybrid Turbulence Models. In *Proceedings of the 17th Numerical Towing Tank Symposium, NuTTS*, volume 14, pages 28–30, 2014.

[60] S.B. Pope. *Turbulent Flows*. Cambridge University Press, 2000. ISBN 9781139643351. URL https://books.google.nl/books?id=4rghAwAAQBAJ.

[61] M. Rafique, P. Chen, and M.P. Duduković. Computational modeling of gas-liquid flow in bubble columns. *Reviews in Chemical Engineering*, 20(3-4): 225–375, 2004.

[62] J.A. Ramírez-Macías, P. Brongers, S. Rúa, and R.E. Vásquez. Hydrodynamic modelling for the remotely operated vehicle Visor3 using CFD. *IFAC-PapersOnLine*, 49(23):187–192, 2016.

[63] J.L. Reboud, B. Stutz, and O. Coutier. Two phase flow structure of cavitation: experiment and modeling of unsteady effects. In *Third International Symposium on Cavitation, Grenoble, France*, 1998.

[64] M. Renilson. *Submarine Hydrodynamics*. SpringerBriefs in Applied Sciences and Technology. Springer International Publishing, 2015. ISBN 9783319161846. URL `https://books.google.nl/books?id=GgkyBwAAQBAJ`.

[65] B.W. Righolt, S. Kenjereš, R. Kalter, M.J. Tummers, and C.R. Kleijn. Dynamics of an oscillating turbulent jet in a confined cavity. *Physics of Fluids*, 27(9):095107, 2015.

[66] D Rijpkema and G Vaz. Viscous flow computations on propulsors: verification, validation and scale effects. *Proceedings of the Developments in Marine CFD*, 2011.

[67] D.R. Rijpkema. Numerical simulation of single-phase and multi-phase flow over a naca 0015 hydrofoil. Master's thesis, M. Sc. Thesis, Delft University of Technology, Faculty of 3ME, 2008.

[68] P.J. Roache. *Verification and Validation in Computational Science and Engineering*. Hermosa, 1998. ISBN 9780913478080. URL `https://books.google.nl/books?id=ENRlQgAACAAJ`.

[69] W. Rodi. A new algebraic relation for calculating the Reynolds stresses. In *Gesellschaft Angewandte Mathematik und Mechanik Workshop Paris France*, volume 56, 1976.

[70] G.F. Rosetti, G. Vaz, and A.L.C. Fujarra. URANS calculations for smooth circular cylinder flow in a wide range of Reynolds numbers: Solution verification and validation. *Journal of Fluids Engineering*, 134(12):121103, 2012.

[71] J.C. Rotta. Statistische theorie nichthomogener turbulenz. *Zeitschrift für Physik*, 129(6):547–572, 1951.

[72] B. Schuiling. The design and numerical demonstration of a new energy saving device. In *16th Numerical Towing Tank Symposium*, pages 141–146, 2013.

[73] S. Socolofsky. Turbulence and the Reynolds Averaged Navier-Stokes equations. Technical report, Texas A&M Ocean Engineering MTS/SNAME, 2008.

[74] P.R. Spalart. Strategies for turbulence modelling and simulations. *International Journal of Heat and Fluid Flow*, 21(3):252–263, 2000.

[75] S.L. Toxopeus, C.D. Simonsen, E. Guilmineau, M. Visonneau, T. Xing, and F. Stern. Investigation of water depth and basin wall effects on KVLCC2 in manoeuvring motion using viscous-flow calculations. *Journal of Marine Science and Technology*, 18(4):471–496, 2013.

[76] M. Ungarish. Hydrodynamics of suspensions. *Journal of Fluid Mechanics*, 290:406–406, 1995.

[77] D.T. Valentine. Reynolds-averaged navier-stokes codes and marine propulsor analysis. Technical report, DTIC Document, 1993.

[78] F. Van den Bosch. Marine Hydrodynamics Lecture 9, 2016. URL `http://www.astro.yale.edu/vdbosch/astro320_summary10.pdf`.

[79] M.Th. Van Hees. Observatieproeven van de onder water uitlaat voor de Walrus-klasse onderzeeboten. Technical report, MARIN, June 1990.

[80] H.C.J. Van Wijngaarden. Tweede serie observatieproeven van de onderwateruitlaat voor de Walrus-klasse onderzeeboten. Technical report, MARIN, March 1992.

[81] G. Vaz, F. Jaouen, and M. Hoekstra. Free-surface viscous flow computations: Validation of urans code fresco. In *ASME 2009 28th International Conference on Ocean, Offshore and Arctic Engineering*, pages 425–437. American Society of Mechanical Engineers, 2009.

[82] W.C. Verloop. The inertial coupling force. *International journal of multiphase flow*, 21(5):929–933, 1995.

[83] S. Wallin and A.V. Johansson. An explicit algebraic Reynolds stress model for incompressible and compressible turbulent flows. *Journal of Fluid Mechanics*, 403:89–132, 2000.

[84] J. Webber. Webbers warships, September 2016. URL `http://www.webberswarships.ca/styled-9/index.html`.

[85] F.M. White. *Viscous Fluid Flow*. McGraw-Hill series in mechanical engineering. McGraw-Hill, 2006. ISBN 9780071244930. URL `https://books.google.nl/books?id=G6IeAQAAIAAJ`.

[86] D.C. Wilcox. Reassessment of the scale-determining equation for advanced turbulence models. *AIAA journal*, 26(11):1299–1310, 1988.

[87] J. Windt. Adaptive Mesh Refinement in Viscous Flow Solvers: Refinement in the Near-wall Region, Implementation and Verification. In *Numerical Towing Tank Symposium*, 2013.

[88] G. Xu and R. Antonia. Effect of different initial conditions on a turbulent round free jet. *Experiments in Fluids*, 33(5):677–683, 2002.

[89] N. Zuber and J.A. Findlay. Average volumetric concentration in two-phase flow systems. *Journal of heat transfer*, 87(4):453–468, 1965.

Appendix A

Conservation of mass equation

The derivation shown here is based on the derivation given by Kundu et al. [35]. Mass is calculated using a volume integral of the density ρ

$$m = \iiint_V \rho \, \mathrm{d}V \tag{A.1}$$

in a fixed control volume V which is independent of time. Conservation of mass states that the time derivative of the mass in a control volume must equal to the mass flux $\rho\mathbf{u}$ across the boundaries

$$\frac{\partial m}{\partial t} = - \oiint_S \rho\mathbf{u} \cdot \mathrm{d}\mathbf{S} \tag{A.2}$$

with a minus to ensure that an outward flow results in a decreasing mass (a surface area vector points outwards). If the equation for mass is substituted this results in

$$\iiint_V \frac{\partial \rho}{\partial t} \mathrm{d}V = - \oiint_S \rho\mathbf{u} \cdot \mathrm{d}\mathbf{S}. \tag{A.3}$$

This equation can be rewritten using the divergence theorem

$$\iiint_V \frac{\partial \rho}{\partial t} \mathrm{d}V = - \iiint_V (\nabla \cdot \rho\mathbf{u}) \, \mathrm{d}V \tag{A.4}$$

so

$$\frac{\partial \rho}{\partial t} = -\nabla \cdot \rho\mathbf{u}. \tag{A.5}$$

Conservation of mass then reads

$$\frac{\partial \rho}{\partial t} + \nabla \cdot \rho\mathbf{u} = 0. \tag{A.6}$$

This equation is also known as the continuity equation.

The continuity equation can be rewritten to

$$\frac{\partial \rho}{\partial t} + \rho \nabla \cdot \mathbf{u} + \rho \left(\nabla \cdot \mathbf{u} \right) = 0 \tag{A.7}$$

in which the material derivative of the density can be recognized

$$\frac{D\rho}{Dt} = \frac{\partial \rho}{\partial t} + \nabla \rho \cdot \mathbf{u}. \tag{A.8}$$

The continuity equation is therefore

$$\frac{D\rho}{Dt} + \rho \left(\nabla \cdot \mathbf{u} \right) = 0. \tag{A.9}$$

If an incompressible flow is considered $\frac{D\rho}{Dt} = 0$, so the expression simplifies to

$$\nabla \cdot \mathbf{u} = 0. \tag{A.10}$$

Appendix B

Conservation of momentum equation

The derivation shown here is based on the derivation given by White [85] and Larsson et al. [37].

The conservation of momentum can be derived from Newton's second law

$$\mathbf{F} = m\mathbf{a}. \tag{B.1}$$

For a fluid particle it is customary to divide by the volume of the particle and use the density, so

$$\rho \frac{D\mathbf{u}}{Dt} = \mathbf{f}. \tag{B.2}$$

The force $\mathbf{f}$ is the applied force per unit volume, and can be split into pressure forces $\mathbf{f}_p$, body forces $\mathbf{f}_b$ and viscous forces $\mathbf{f}_v$,

$$\mathbf{f} = \mathbf{f}_p + \mathbf{f}_b + \mathbf{f}_v. \tag{B.3}$$

The pressure force can be written as

$$\mathbf{f}_p = -\frac{1}{\rho}\nabla p. \tag{B.4}$$

Body forces are for instance gravity. Lastly the viscous forces must be determined. These forces are caused by the stresses acting on the sides of the fluid particle. The net force on the particle in each direction is

$$
\begin{aligned}
dF_{x,net} &= \left(\frac{\partial \tau_{xx}}{\partial x}dx\right)dydz + \left(\frac{\partial \tau_{yx}}{\partial y}dy\right)dxdz + \left(\frac{\partial \tau_{zx}}{\partial z}dz\right)dxdy \\
dF_{y,net} &= \left(\frac{\partial \tau_{xy}}{\partial x}dx\right)dydz + \left(\frac{\partial \tau_{yy}}{\partial y}dy\right)dxdz + \left(\frac{\partial \tau_{zy}}{\partial z}dz\right)dxdy \\
dF_{z,net} &= \left(\frac{\partial \tau_{xz}}{\partial x}dx\right)dydz + \left(\frac{\partial \tau_{yz}}{\partial y}dy\right)dxdz + \left(\frac{\partial \tau_{zz}}{\partial z}dz\right)dxdy
\end{aligned}
\tag{B.5}
$$

or on a unit volume basis (divided by the volume $dxdydz$)

$$f_x = \frac{\partial \tau_{xx}}{\partial x} + \frac{\partial \tau_{yx}}{\partial y} + \frac{\partial \tau_{zx}}{\partial z}$$
$$f_y = \frac{\partial \tau_{xy}}{\partial x} + \frac{\partial \tau_{yy}}{\partial y} + \frac{\partial \tau_{zy}}{\partial z} \tag{B.6}$$
$$f_z = \frac{\partial \tau_{xz}}{\partial x} + \frac{\partial \tau_{yz}}{\partial y} + \frac{\partial \tau_{zz}}{\partial z}$$

Stokes theorem states that the viscous stress tensor τ_{ij} is proportional to the rate of symmetric strain tensor S_{ij}, according to

$$\tau_{ij} = \mu S_{ij} \tag{B.7}$$

in which μ is the dynamic viscosity, and S_{ij} is defined as

$$S_{ij} = \frac{\partial u_i}{\partial x_j} + \frac{\partial u_j}{\partial x_i}, \tag{B.8}$$

with the dynamic viscosity. The six components of the strain tensor can be written as

$$\tau_{xx} = 2\mu \frac{\partial u}{\partial x}$$
$$\tau_{xy} = \tau_{yx} = \mu \left(\frac{\partial u}{\partial y} + \frac{\partial v}{\partial x} \right)$$
$$\tau_{zx} = \tau_{xz} = \mu \left(\frac{\partial w}{\partial x} + \frac{\partial u}{\partial z} \right)$$
$$\tau_{yy} = 2\mu \frac{\partial v}{\partial y} \tag{B.9}$$
$$\tau_{yz} = \tau_{zy} = \mu \left(\frac{\partial v}{\partial z} + \frac{\partial w}{\partial y} \right)$$
$$\tau_{zz} = 2\mu \frac{\partial w}{\partial z}.$$

By substituting these expressions in the equations for the net force in each direction it follows after some rewriting that

$$\mathbf{f}_v = \mu \nabla^2 \mathbf{u}. \tag{B.10}$$

Therefore the conservation of momentum in conservative form is

$$\frac{D\mathbf{u}}{Dt} = \mathbf{f} - \frac{1}{\rho} \nabla p + \nu \nabla^2 \mathbf{u} \tag{B.11}$$

or

$$\rho \frac{\partial \mathbf{u}}{\partial t} + \rho \mathbf{u} \cdot \nabla \mathbf{u} = \rho \mathbf{f} - \nabla p + \mu \nabla^2 \mathbf{u} \tag{B.12}$$

This equation together with the continuity equation is known as the Navier-Stokes equations.

Appendix C

RANS equations derivation

The derivation given here is based on the derivation given by Valentine [77] and Socolofsky [73], The Navier-Stokes equations consist out of two equations:

- the conservation of mass,

- the conservation of momentum

The conservation of mass is given by

$$\frac{\partial u_i}{\partial x_i} = 0. \tag{C.1}$$

The conservation of momentum is

$$\rho \frac{\partial \mathbf{u}}{\partial t} + \rho \mathbf{u} \cdot \nabla \mathbf{u} = \rho \mathbf{f} - \nabla p + \mu \nabla^2 \mathbf{u} \tag{C.2}$$

or

$$\frac{D\mathbf{u}}{Dt} = \mathbf{f} - \frac{1}{\rho} \nabla p + \nu \nabla^2 \mathbf{u} \tag{C.3}$$

under the assumption that the viscosity and density is constant. An alternative formulation, in index notation, is

$$\frac{\partial u_i}{\partial t} + \frac{\partial}{\partial x_j} \left(u_j u_i \right) = -\frac{1}{\rho} \frac{\partial p}{\partial x_i} + \nu \frac{\partial^2 u_i}{\partial x_j^2} + f_i. \tag{C.4}$$

Reynolds decomposition decomposes the velocity field $\mathbf{u}$ in a mean, $\bar{\mathbf{u}}$, and a random fluctuation, $\mathbf{u}'$, such that

$$u_i = \bar{u}_i + u_i'. \tag{C.5}$$

The same principle is applied to the pressure p

$$p = \bar{p} + p' \tag{C.6}$$

and the body forces f_i

$$f_i = \bar{f}_i + f'_i. \tag{C.7}$$

The decomposed velocity and pressure are substituted in the Navier-Stokes equations. Firstly in the conservation of mass, which yields

$$\frac{\partial}{\partial x_i} \left(\bar{u}_i + u'_i \right) = 0. \tag{C.8}$$

This equation is time-averaged

$$\lim_{T \to \infty} \frac{1}{T} \int_{t_0}^{t_0+T} \frac{\partial}{\partial x_i} \left(\bar{u}_i + u'_i \right) \mathrm{d}t = 0 \tag{C.9}$$

$$\frac{\partial}{\partial x_i} \left(\overline{\bar{u}_i + u'_i} \right) = 0 \tag{C.10}$$

$$\frac{\partial}{\partial x_i} \left(\bar{u}_i + \bar{u}_i{}' \right) = 0. \tag{C.11}$$

Since the average of the fluctuations, $\bar{u}'_i$, is zero the the averaged flow field is

$$\frac{\partial \bar{u}_i}{\partial x_i} = 0 \tag{C.12}$$

From equation C.8 and the continuity of the average flow field it can be concluded that the flow fluctuations also obey continuity

$$\frac{\partial u'_i}{\partial x_i} = 0. \tag{C.13}$$

If Reynolds decomposition is applied to the conservation of momentum equation the following equation is obtained

$$\frac{\partial \left(\bar{u}_i + u'_i \right)}{\partial t} + \frac{\partial}{\partial x_j} \left(\left(\bar{u}_j + u'_j \right) \left(\bar{u}_i + u'_i \right) \right) =$$
$$- \frac{1}{\rho} \frac{\partial \left(\bar{p} + p' \right)}{\partial x_i} + \nu \frac{\partial^2 \left(\bar{u}_i + u'_i \right)}{\partial x_j^2} + \left(\bar{f}_i + f'_i \right). \tag{C.14}$$

This equation is again time-averaged

$$\frac{\partial \left(\overline{\bar{u}_i + u'_i} \right)}{\partial t} + \frac{\partial}{\partial x_j} \left(\overline{\left(\bar{u}_j + u'_j \right) \left(\bar{u}_i + u'_i \right)} \right) = -\frac{1}{\rho} \frac{\partial \left(\overline{\bar{p} + p'} \right)}{\partial x_i}$$
$$+ \nu \frac{\partial^2 \left(\overline{\bar{u}_i + u'_i} \right)}{\partial x_j^2} + \left(\overline{\bar{f}_i + f'_i} \right) \tag{C.15}$$

$$\frac{\partial \bar{u}_i}{\partial t} + \frac{\partial}{\partial x_j} \left(\overline{\bar{u}_j \bar{u}_i} + \overline{\bar{u}_j u'_i} + \overline{u'_j \bar{u}_i} + \overline{u'_i u'_j} \right) = -\frac{1}{\rho}\frac{\partial \bar{p}}{\partial x_i} + \nu \frac{\partial^2 \bar{u}_i}{\partial x_j^2} + \bar{f}_i. \tag{C.16}$$

Since $\bar{u}$ is constant and $\bar{u}'$ is zero this becomes

$$\frac{\partial \bar{u}_i}{\partial t} + \frac{\partial}{\partial x_j} \left(\overline{\bar{u}_j \bar{u}_i} + \overline{u'_i u'_j} \right) = -\frac{1}{\rho}\frac{\partial \bar{p}}{\partial x_i} + \nu \frac{\partial^2 \bar{u}_i}{\partial x_j^2} + \bar{f}_i \tag{C.17}$$

$$\frac{\partial \bar{u}_i}{\partial t} + \bar{u}_j \frac{\partial \bar{u}_i}{\partial x_j} = -\frac{1}{\rho}\frac{\partial \bar{p}}{\partial x_i} + \nu \frac{\partial^2 \bar{u}_i}{\partial x_j^2} - \frac{\partial}{\partial x_j} \left(\overline{u'_i u'_j} \right) + \bar{f}_i \tag{C.18}$$

or

$$\frac{\partial \bar{u}_i}{\partial t} + \bar{u}_j \frac{\partial \bar{u}_i}{\partial x_j} = \frac{1}{\rho}\frac{\partial}{\partial x_i} \left(-\bar{p}\delta_{ij} + \mu\frac{\partial \bar{u}_i}{\partial x_j} - \rho\overline{u'_i u'_j} \right) + \bar{f}_i. \tag{C.19}$$

In scalar form this equation is

$$\rho\frac{D\bar{\mathbf{u}}}{Dt} + \rho\frac{\partial}{\partial x_j} \left(\overline{u'_i u'_j} \right) = \rho\mathbf{f} - \nabla\bar{p} + \mu\nabla^2\bar{\mathbf{u}} \tag{C.20}$$

Together with the conservation of mass these two equations form the so-called unsteady Reynolds Average Navier-Stokes equations or RANS. The second term in the conservation of momentum represents the mean transport of fluctuating momentum by turbulent velocity fluctuations. Since this term is not negligible and an analytic form is unknown this term leads to the closure problem of turbulence.

Appendix D

Numerical settings

Timeloop	Solution scheme	Implicit three time level
Outerloop	Max iteration	150
	Convergence tolerance	$1 \cdot 10^{-4}$
Boundaries	Walls	Slipwall
	Top	Pressure
	Inflow turbulence	$\frac{\nu_t}{\nu}$ $1 \cdot 10^{-2}$
Solver	Mass momentum solver	Segregated
Momentum	Solver	CG
	Preconditioner	Jacobi
	Convergence tolerance	$1 \cdot 10^{-2}$
	Max iteration	200
	Explicit relaxation	0.7
	Convective flux discretization	QUICK with flux limiter
	Residual normalization	Parnassos like
Turbulence	Solver	CG
	Preconditioner	BJacobi
	Convergence tolerance	$1 \cdot 10^{-1}$
	Max iteration	200
	Explicit relaxation	0.25
	Convective flux discretization	QUICK with flux limiter
Pressure	Solver	GMRES
	Convergence tolerance	$1 \cdot 10^{-2}$
	Max iteration	500
	Explicit relaxation	0.15

Free surface	Solver	CG
	Convergence tolerance	$1 \cdot 10^{-2}$
	Max iteration	200
	Explicit relaxation	0.5
	Convective flux discretisation	Fromm scheme with SUPERBEE limiter
Materials	Water dynamic viscosity	$1.002 \cdot 10^{-3}$
	Water density	998
	Air dynamic viscosity	$1.8 \cdot 10^{-5}$
	Air density	1.2

Appendix E

Statistical uncertainty

The uncertainty analysis of finite length measurement signals is described. This derivation is based on the work by Brouwer et al. [5].

A measured time series $x_i(t)$ with finite length T is considered a sample record of an ergodic stationary random process $\{x(t)\}$. The sample time-average m_i is an estimator of the mean of the process μ_x with

$$m_i = \frac{1}{T} \int_0^T x_i(t)\mathrm{d}t. \tag{E.1}$$

The sample record variance s_i^2 is an estimator of the variance of the process σ_x^2 with

$$s_i^2 = \frac{1}{T} \int_0^T \left(x_i(t) - m_i\right)\mathrm{d}t. \tag{E.2}$$

Due to the finite length of of the time series there is a deviation between m_i and μ_x. The expected value of the variance of the mean s_m can be written as

$$s_m^2 = E\left[(m_i - \mu_x)^2\right]. \tag{E.3}$$

Substituting the equation for the sample time-average m_i in this equation yields

$$s_m^2 = E\left[\left(\frac{1}{T} \int_0^T x_i(t)\mathrm{d}t - \mu_x\right)^2\right] \tag{E.4}$$

$$s_m^2 = E\left[\frac{1}{T^2}\left(\int_0^T x_i(t)\mathrm{d}t\right)^2 - 2\frac{\mu_x}{T}\int_0^T x_i(t)\mathrm{d}t + \mu_x^2\right] \tag{E.5}$$

$$s_m^2 = E\left[\frac{1}{T^2}\left(\int_0^T x_i(t)\mathrm{d}t\right)^2\right] - 2E\left[\frac{\mu_x}{T}\int_0^T x_i(t)\mathrm{d}t\right] + E\left[\mu_x^2\right] \tag{E.6}$$

$$s_m^2 = E\left[\frac{1}{T^2}\left(\int_0^T x_i(t)\mathrm{d}t\right)^2\right] - 2\mu_x^2 + \mu_x^2 \tag{E.7}$$

$$s_m^2 = \frac{1}{T^2}\int_0^T\int_0^T E\left[x_i(\xi)x_i(\eta)\right]\mathrm{d}\eta\mathrm{d}\xi - \mu_x^2. \tag{E.8}$$

When this is combined with the autocovariance function

$$C_{xx}(t,s) = E[(X_t - \mu_t)(X_s - \mu_s)] = E[X_t X_s] - \mu_t\mu_s, \tag{E.9}$$

for a stationary process, in which

$$\mu_t = \mu_s = \mu \tag{E.10}$$

and

$$C_{xx}(t,s) = C_{xx}(s-t) = C_{xx}(\tau) \tag{E.11}$$

where $\tau = |s - t|$ (the lag time), the variance of the mean s_m^2 can be written as

$$s_m^2 = \frac{2}{T}\int_0^T\left(1 - \frac{\tau}{T}\right)C_{xx}(\tau)\mathrm{d}\tau. \tag{E.12}$$

$C_{xx}(\tau)$ can be directly calculated using

$$C_{xx}(\tau) = \frac{1}{T}\cdot\int_0^T x_i(t)\cdot x_i(t+\tau)\mathrm{d}t - \mu_x^2 \tag{E.13}$$

or using the Fourier transform of the one-sided autospectral density function $S_{xx}(f)$

$$C_{xx}(\tau) = \int_0^\infty S_{xx}(f)\cos(2\pi f\tau)\mathrm{d}f \tag{E.14}$$

which is a quicker process. This relation is known as the Wiener-Khinchine relation. $S_{xx}(f)$ can be calculated using

$$S_{xx}(f) = \frac{2}{T}|X(f)|^2 \tag{E.15}$$

and

$$X(f) = \int_0^T (x_i(t) - m_i)\,e^{-i2\pi ft}\mathrm{d}t. \tag{E.16}$$

The random uncertainty of the mean of a single sample record can be calculated using the autocovariance method, which makes use of equation E.12. However due to the numerical evaluation of the integrals negative values for s_m^2 can occur. As method to circumvent this problem a biased estimator for the autocovariance $C_{xx,biased}(\tau)$ can be used. This estimator is defined as

$$C_{xx,biased}(\tau) = \left(1 - \frac{|\tau|}{T}\right)\cdot C_{xx}(\tau). \tag{E.17}$$

The used of a biased estimator yields positive values for s_m^2, however these values are biased. Equation E.12 for biased definitions gives

$$s_{m,biased}^2 = \frac{2}{T} \int_0^T \left(1 - \frac{\tau}{T}\right) C_{xx,biased}(\tau) \mathrm{d}\tau = \frac{2}{T} \int_0^T \left(1 - \frac{\tau}{T}\right)^2 C_{xx}(\tau) \mathrm{d}\tau. \quad \text{(E.18)}$$

For oscillatory signals and the condition for the sample length T

$$T > \frac{1}{f_L} \quad \text{(E.19)}$$

in which f_L is the lowest (dominant) frequency component, the ratio of biased to unbiased variance of the mean becomes

$$\frac{s_{m,biased}^2}{s_m^2} = 2. \quad \text{(E.20)}$$

Using this and the fact that the random uncertainty of the mean value at the first-order replication level is equal to the standard deviation of the mean, the uncertainty u can be calculated using

$$u = \sqrt{\frac{1}{T} \int_0^T \left(1 - \frac{\tau}{T}\right) C_{xx,biased}(\tau) \mathrm{d}\tau}. \quad \text{(E.21)}$$

The expanded uncertainty is calculated using

$$U = k_\% \cdot u \quad \text{(E.22)}$$

in which $k_\%$ is a coverage factor. For a 95% confidence interval $k_\% = 1.96$, and for a 99% confidence interval $k_\% = 2.58$ [21].

Appendix F

Discretization uncertainty

The discretization uncertainty is determined using the procedure of Eça and Hoekstra [16]. For this method at least four, geometrically similar, grids are required. First an overview of the procedure is given, at the end the extension needed for unsteady calculations as given by Rosetti et al. [70] is described.

Determination of ϵ_ϕ

Firstly the error estimate ϵ_ϕ is determined. This error estimate is calculated by determining the minimum of the function

$$S_{RE}(\phi_0, \alpha, p) = \sqrt{\sum_{i=1}^{n_g} w_i \left(\phi_i - (\phi_0 + \alpha h_i^p) \right)^2}$$ (F.1)

with and without weights. The weights can be determined using

$$w_i = \frac{\frac{1}{h_i}}{\sum_{i=1}^{n_g} \frac{1}{h_i}}$$ (F.2)

and

$$nw_i = n_g w_i$$ (F.3)

ϵ_ϕ can be determined based on the obtained value of p:

- If any of the fits yields $0.5 \leq p \leq 2$, $\epsilon_\phi = \delta_{RE}$, if both fits satisfy this condition the fit with the smallest standard deviation is used. δ_{RE} can be calculated with
$$\delta_{RE} = \alpha h_i^p.$$ (F.4)

- If $p > 2$ solve
$$\delta_1 = \alpha h_i$$ (F.5)

and

$$\delta_2 = \alpha h_i^2 \tag{F.6}$$

with and without weights. This can be done by solving for the minimum of the functions

$$S_1(\phi_0, \alpha) = \sqrt{\sum_{i=1}^{n_g} w_i \left(\phi_i - (\phi_0 + \alpha h_i)\right)^2} \tag{F.7}$$

and

$$S_2(\phi_0, \alpha) = \sqrt{\sum_{i=1}^{n_g} w_i \left(\phi_i - \left(\phi_0 + \alpha h_i^2\right)\right)^2}. \tag{F.8}$$

The fit with the smallest standard deviation yields ϵ_ϕ.

- If $p < 0.5$ or impossible to establish solve

$$\delta_1 = \alpha h_i \tag{F.9}$$

$$\delta_2 = \alpha h_i^2 \tag{F.10}$$

and

$$\delta_1 2 = \alpha_1 h_i \alpha_2 h_i^2 \tag{F.11}$$

with and without weights. This can be done by determining the minimum of functions F.7, F.8 and

$$S_{12}(\phi_0, \alpha_1, \alpha_2) = \sqrt{\sum_{i=1}^{n_g} w_i \left(\phi_i - \left(\phi_0 + \alpha_1 h_i + \alpha_2 h_i^2\right)\right)^2}. \tag{F.12}$$

The fit with the smallest standard deviation yields ϵ_ϕ.

Data range parameter

Next a data range parameter is calculated to asses the quality of the fit, this parameter is calculated using

$$\Delta_\phi = \frac{(\phi_i)_{max} - (\phi_i)_{min}}{n_g - 1} \tag{F.13}$$

in which n_g is the number of used grids.

Determination of the safety factor

A safety factor is determined from p, σ and Δ_ϕ:

- if $0.5 \leq p < 2.1$ and $\sigma < \Delta_\phi$, $F_S = 1.25$,

- otherwise, $F_S = 3$

Determination of the numerical uncertainty

Finally the uncertainty is calculated using:

- if $\sigma < \Delta_\phi$

$$U_\phi(\phi_i) = F_S \epsilon_\phi(\phi_i) + \sigma + |\phi_i - \phi_{fit}| \tag{F.14}$$

- if $\sigma \geq \Delta_\phi$

$$U_\phi(\phi_i) = 3\frac{\sigma}{\Delta_\phi} \left(\epsilon_\phi(\phi_i) + \sigma + |\phi_i - \phi_{fit}| \right). \tag{F.15}$$

Here ϕ_{fit} is defined as

$$\phi_{fit} = \phi_0 + \epsilon_{phi}. \tag{F.16}$$

Adaptation for unsteady simulations

The error estimate for unsteady simulations makes use of an extended equation to estimate the error [70],

$$\delta_{RE} = \alpha_x h_i^{p_x} + \alpha_t \tau_i^{p_t} \tag{F.17}$$

which leads to the following function for S_{RE}

$$S_{RE}(\phi_0, \alpha, p) = \sqrt{\sum_{i=1}^{n_g} w_i \left(\phi_i - (\phi_0 + \alpha_x h_i^{p_x} + \alpha_t \tau_i^{p_t}) \right)^2}. \tag{F.18}$$

To determine the minimum of this function a Newton-Raphson shooting method is needed to solve the set of nonlinear equations which arise [70].